The Development of a Localized Disturbance in a Boundary Layer

by

Kenneth Samuel Breuer

Sc.B. Mechanical Engineering, Brown University, 1982
S.M. Aeronautics and Astronautics, Massachusetts Institute of Technology, 1984

SUBMITTED IN PARTIAL FULFILLMENT OF THE
REQUIREMENTS FOR THE DEGREE OF

Doctor of Philosophy
in
Fluid Mechanics
Department of Aeronautics and Astronautics
at the
Massachusetts Institute of Technology

May 1988

Signature of Author _____
Department of Aeronautics and Astronautics
April 29, 1988

Certified by _____
Marten T. Landahl
Professor, Department of Aeronautics and Astronautics

Certified by _____
Joseph H. Haritonidis
Associate Professor, Department of Aeronautics and Astronautics

Certified by _____
Sheila E. Widnall
Professor, Department of Aeronautics and Astronautics

Accepted by _____
Professor Harold Y. Wachman
Chairman, Department Graduate Committee

The Development of a Localized Disturbance in a Boundary Layer

by
Kenneth Samuel Breuer

Submitted to the Department of Aeronautics and Astronautics, April 29, 1988, in partial fulfillment of the requirements for the degree of Doctor of Philosophy in Fluid Mechanics

The development of a localized disturbance in a laminar boundary layer is considered. It is found that the disturbance can be conceived of as being comprised of two parts: a wave portion, and an advective portion which travels at the local mean velocity. Measurements and theoretical results reveal that the transient portion of the disturbance develops into an inclined shear layer which attains a maximum perturbation amplitude, but elongates linearly with time, exhibiting an algebraic instability in accordance with Landahl[46]. For weak disturbances, the effects of viscosity cause the transient portion to decay exponentially, leaving only the dispersive wave modes which form a linearly unstable wave packet, in good agreement with the theory of Gaster[18]. The effects of a weak non-linearity are also observed. For higher amplitude disturbances, numerical simulation and experiments reveal that the shear layer created by the transient distorts the local mean profile sufficiently to allow a secondary shear-layer-type instability to grow. A strong non-linear mechanism is also observed which causes the formation of long streamwise 'strips' of alternating high- and low-speed fluid. Disturbances of opposite sign are also considered. By comparing the results for identical but opposite disturbances the effects of non-linearity are assessed. It is found that the strong 'negative' disturbance, which does not exhibit any secondary instability, grows at a slower rate than the positive disturbance.

The structure of the disturbance in the laminar boundary layer is compared with structures found by conditional sampling of turbulent velocity fields. It is found that the transitional and turbulent structures have many common features and it is proposed that they are both governed by the same dynamical processes: three-dimensionality and the interaction with a strongly sheared mean velocity profile.

Thesis Co-Supervisors: Marten T. Landahl, Professor of Aeronautics and Astronautics
Joseph H. Haritonidis, Associate Professor of Aeronautics and Astronautics.

To my father, and the memory of my mother

Acknowledgments

The support for this work derives from several agencies and I would like to acknowledge here their generous support. The Office of Naval Research Graduate Fellowship Program supported me for my first two years of graduate school and during my final year of study. I am particularly grateful to Mike Reischman and to Debbie Hughes for their help in securing funding for my last year at MIT. The Office of Naval Research also provided support under Contract #N00014-78-C-0696. The Air Force Office for Scientific Research provided generous support for the two intervening years at MIT under Contract #F49620-83-C-0019. The Royal Insitutute of Technology in Stockholm and the NASA/Stanford Center for Turbulence Research provided financing during my visits to Sweden and Ames. I would also like to acknowledge the support of several individuals who have provided help and support during the past few years at MIT.

Marten Landahl, for his advice and encouragement during the course of my work. Marten's broad knowledge and his physical insight were always helpful, and always available.

Joe Haritonidis, who defined the standard for experimental excellence and then patiently passed on his expertise. Joe's enthusiasm and his rigorous attention to detail have been invaluable during the course of my work.

Jacob Cohen, who first introduced me to the darker (and more interesting) side of stability theory and whose friendship and help are gratefully appreciated.

Skip Gresko, who not only became an invaluable ally, from system programming to hot-wire construction, but also tidied up the lab.

Henrik Alfredsson, Arne Johansson, Dan Henningson and everyone at KTH and FFA in Stockholm for their friendship and help during my stay in Stockholm.

John Kim and Parvis Moin at the NASA/Stanford Center for Turbulence Research who made the 1987 summer program so fruitful and enjoyable. I am especially indebted to Phillipe Spalart for allowing me to use his boundary layer code and for explaining its inner secrets.

Finally, to my family, friends and fellow graduate students, who have managed to endure my travails during these past few years and still somehow managed to remain my friends. Special thanks to Gil Troy who was always ready to catch that late movie or to commiserate on our meager existance. Last but not least, thanks to Rochelle Hahn for her patience and support during this time.

Contents

List of Tables

List of Figures

List of Symbols

Roman

D	Diameter of hot wire sensing element
E_1, E_2	Raw voltages from hot wire annemometers
f	Frequency (in Hertz)
$\mathbf{I}$	Identity matrix
J	Number of points in normal direction
k	Two-dimensional wave number: $k^2 = \alpha^2 + \beta^2$
L	Length of hot wire sensing element
l_x, l_y, l_z	Length scales for initial conditions
p	Pressure perturbation
$\mathbf{R}, \mathbf{S}, \mathbf{T}, \mathbf{D}$	Matrices for finite difference calculations
Re_{δ_*}	Reynolds number based on displacement thickness
Re_x	Reynolds number based on x
t	Time
U_∞	Free stream velocity
$U, U(y)$	Local mean velocity
U', U''	Derivatives of local mean velocity
u, v, w	Perturbation velocity components
u_τ	Friction velocity
$\tilde{u}, \tilde{v}, \tilde{w}$	Fourier transformed perturbation velocities
$\tilde{u}_1, \tilde{w}_1$	Horizontal velocities in rotated coordinate system
x, y, z	Coordinate directions
x_0	Position of membrane disturbance

x_v	Virtual origin for Blasius boundary layer

Greek

α	Streamwise wave number
β	(a) Non-dimensional frequency: $\beta = 2\pi f \delta_* / U_\infty$
	(b) Spanwise wave number
δ_*	Displacement thickness
$\delta, \delta_{.99}$	Boundary layer thickness
δ_θ	Momentum thickness
Δx	x location relative to membrane location
Δy	Discretization distance in normal direction
Δt	Time step
η	(a) Non-dimensional Blasius coordinate: $\eta = y\sqrt{U/\nu(x - x_v)}$
	(b) Lagrangian coordinate in normal direction
ξ, ς	Largrangian coordinates
ν	Kinematic viscosity
ρ	Fluid density

Superscripts

n	Index denoting time step
$+$	Normalized by viscous wall parameters

Subscripts

j	Index denoting vertical position

Chapter 1

Introduction

The problem of transition to turbulence has been investigated extensively during the past 100 years. Hundreds of papers and books have been written on the subject, and several excellent review articles are available. In this introduction we shall provide a brief overview of the current literature as it pertains to this thesis. For a more detailed coverage of the subject, the reader is referred to one of the more comprehensive articles. For example, see Drazin & Reid[17], Drazin & Howard[16], Maslowe[53], Lin[50], Betchov & Criminale[7] or Tani[72].

1.1 Previous Results

Research into transition to turbulence was initiated by Reynolds[62] in his classic pipe flow experiment. Reynolds described the transition of laminar flow into a "sinuous motion", and he speculated that an instability mechanism might be responsible for the breakdown of the flow. Rayleigh[61] was the first to investigate this idea theoretically, and he derived the equations for the evolution of a small amplitude wave in an inviscid parallel shear flow. Rayleigh also realized that in order for an instability to grow in such a flow, it was necessary for the mean velocity profile to have an inflection point. The viscous theory was later developed independently by Orr[58] & Sommerfeld[67] after

whom the now classic linear stability equation is named.

The solution to the Orr-Sommerfeld equation was investigated by several researchers in the ensuing years. Heisenberg[26] was the first to show that a flow which does not have an inflection point, and is thus inviscidly stable according to Rayleigh's inflectional criterion, nevertheless exhibits instability at high Reynolds numbers. He used asymptotic theory for large Re and for long waves, and estimated that the critical Reynolds number - the value at which the flow became unstable to infinitesimal disturbances - was of the order of 1000 for plane Poiseuille flow. Tollmien[73] and Schlichting[65] advanced the theory for boundary layer flows, and estimated the critical Reynolds number for that flow to be between 420 and 575. Schlichting also determined the eigenfunctions for the wave motion - the amplitude distribution of the wave through the boundary layer.

Experimental confirmation of the theoretical results was slow in coming primarily because of the extreme difficulty in building a facility with sufficiently low noise levels to be able to measure such small amplitude waves. Confirmation of the theory was made possible in the 1940's when Dryden constructed a low-noise wind tunnel at the National Bureau of Standards, in Washington D.C.. In the series of experiments by Schubauer & Skramstad[66] an oscillating ribbon was used to generate two-dimensional low-amplitude waves of a fixed frequency, and hot wire anemometers were employed to measure the growth of these waves in the boundary layer. The shape of the neutral curve, the growth rates, and the eigenfunctions predicted by the theory of Tollmien & Schlichting were all confirmed.

1.1.1 Three Dimensional Secondary Instabilities

All of the research thus far had concentrated on the growth of two-dimensional waves, and considerable success had been achieved in matching theory and experiments for the early stages of transition. However, it became clear from the experiments of Klebanoff, Tidstrom & Sargent[41,42] that the latter stages of transition were governed by three-dimensional processes. In their experiments, the scale of the three-dimensionality was artificially fixed by placing pieces of tape at regular intervals across the span of the flat plate. This enabled the detailed measurement of the secondary structure, which they found to consist of 'peaks' and 'valleys' imbedded in the two-dimensional wave structure. The fluid at the peaks moved downstream faster than the fluid at the valleys, forming 'lambda' vortex structures which subsequently broke down to turbulence very rapidly. Kovasznay, Komoda & Vasudeva[43] investigated the vortices more closely and discovered that associated with the lambda structures were intense internal shear layers. Benney & Lin[6] modeled the three-dimensional instability problem theoretically by superimposing oblique waves onto the two-dimensional Tollmien-Schlichting waves and then considering the non-linear interaction between the two and the mean shear flow. They found good agreement with the results of Klebanoff et al. Herbert[30] applied a Floquet analysis to the same problem and found that the secondary instability contained a coupling between the two-dimensional Tollmien-Schlichting waves and the normal vorticity modes (from the oblique waves). This interaction is very similar to the resonant interaction discussed by Benney & Gustavsson[5] in which a resonance between the normal velocity and the the normal vorticity can result in additional instability modes. These resonant modes were calculated for Couette flow by Gustavsson and Hultgren[23] and for Plane Poiseuille flow by Gustavsson[24].

A different nonlinear route to breakdown was discussed by Herbert[29] and also Craik[14] in which a subharmonic resonance occurs between the primary wave and oblique waves with half the frequency. This breakdown scenario was observed experimentally by Kachanov & Levchenko[37].

Recent advances in computational ability have allowed researchers to study the transition problem numerically, and simulations of boundary layer transition have been made by Wray & Hussaini[74], Spalart & Yang[70] and others. Transition in plane Poiseuille flow, which is somewhat easier to handle numerically because of the finite geometry, has also been studied by Orszag & Kells[59], Gilbert & Kleiser[21], and others. The numerical results agree well with the experimental data through the onset of the secondary instability, but the limited resolution of the calculations, imposed by the limited computer memory available, has made simulation beyond this stage difficult. Recent calculations with larger machines should overcome this problem.

1.1.2 The Initial Value Problem

The discussion thus far has concentrated solely on a normal mode analysis in which the disturbance is assumed to be an infinite and uniform wave train. The problem with this approach is that while it is a natural starting place in the investigation of the stability of a particular flow, it is not a very accurate approximation to what one might expect in a physical situation. A real flow is unlikely to experience two-dimensional uniform disturbaces, but rather will be subjected to isolated, impulsive and three-dimensional disturbances. On an aircraft wing, for example, such disturbances might originate from an imperfection on the wing surface, or from localized upstream irregularities, acoustic sources etc. For this reason, it would seem more appropriate to extend the present

analysis to three-dimensional, impulsive disturbances.

There are several features that become apparent, when one looks at a single disturbance, localized in time and space. Orr[58] discussed the initial value problem and pointed out that in addition to the discrete spectrum whose modes are governed by the Rayleigh equation, a continuous spectrum of modes must also be considered in order to account for a general initial disturbance. In an inviscid flow, the existence of the continuous spectrum is a result of the exclusion of viscosity which introduces a singularity into the equations at the point were the wave speed equals the local mean velocity (see Lin[50] for more details). For viscous flows, however, this singularity is no longer present, but for infinite or semi-infinite domains, such as the shear layer or the boundary layer, Gustavsson[24] found that a viscous continuous spectrum exists associated with the absence of the solid boundary. Since flows in finite domains, such as channel flow, do not have a viscous continuous spectrum, an arbitrary initial disturbance may therefore be fully represented by a summation of normal (discrete) modes.

Case[10] outlined the solution for a general two-dimensional parallel flow and distinguished between dispersive modes, which derive from the normal mode analysis, and advective modes which are associated with the (inviscid) continuous spectrum. He carried out an asymptotic analysis for these advective modes and predicted that they decay at least as fast as $1/t$. However, Gustavsson[24] found that the advective modes decay as $1/t^2$, and Gustavsson noted that there may be an error in Case's analysis. The dispersive part of the disturbance is neutrally stable (in the inviscid case) and thus the total wave energy remains constant. However, since the waves spread out spatially as the waves disperse, their amplitude decays as $1/t^2$[24].

For three-dimensional disturbances, an additional mechanism must also be consid-

ered. For any general inviscid three-dimensional disturbance, a 'lift-up' term emerges[44] from the analysis in which fluid particles retain their horizontal momentum when lifted up by the integrated effect of the vertical velocity. If there is a mean shear, this lift-up of fluid creates a horizontal disturbance velocity which will not in general disappear as time goes to infinity. This *permanent scar*[44] in the streamwise velocity is only present for a three-dimensional disturbance. Landahl[46] also showed that any general three-dimensional disturbance is subject to an algebraic instability. This instability mechanism predicts that as $t \rightarrow \infty$, the energy of the disturbance will grow at least as fast as linearly in time - in sharp contrast to the two-dimensional theory, in which the advective modes decay in time, and the dispersive modes are neutrally stable.

Gustavsson[24] considered the three-dimensional linear initial value problem for the boundary layer in some detail, approximating the mean profile by a piecewise linear profile. He also found that the disturbance was represented by two components: the dispersive part, governed by the Rayleigh equation and traveling with typical dispersive wave velocities, and the advective part resulting from the inviscid continuous spectrum and traveling at the local mean velocity. In agreement with Landahl[44], Gustavsson also found that in addition to the decaying continuous modes that were derived in the two-dimensional analysis, the streamwise component of the disturbance contains a non-vanishing term, due entirely to the spanwise structure of the initial disturbance and the lift-up effect. The spanwise velocities also behave in a similar manner, and so for large times the horizontal velocities will dominate over the vertical velocity due to the liftup effect.

Recently, Henningson[27], in a detailed analysis of the inviscid initial value problem in plane Poiseuille flow, associated the liftup effect with normal vorticity modes - the

modes that Craik[15] and Herbert[30] found to be excited in secondary instabilities. Russell & Landahl[63] examined an initial value problem in which the dispersive effects were completely ignored and thus the entire evolution of the disturbance is governed by the liftup effect. Their Flat-Eddy model, which will be used later, included nonlinear effects and showed the development of internal shear layers, which intensified as the disturbance traveled downstream.

The purely dispersive aspects of a three-dimensional linear disturbance were investigated theoretically by Gaster[18] and experimentally by Gaster & Grant[20]. Gaster represented the disturbance by a summation of the least-stable Orr-Sommerfeld modes and modeled the disturbance's evolution by calculating the growth and decay of individual modes according to the solutions of the Orr-Sommerfeld equation. The calculated disturbance was a swept back wave packet which agreed well with the measurements which were taken just outside the boundary layer. At this position, the liftup of fluid does not produce any horizontal perturbations since there is no mean shear, and so Gaster's model is appropriate at this location outside the boundary layer. Gaster did report seeing shear layers when the same measurements were made inside the boundary layer[19], but he erroneously attributed this to non-linear effects. Recently, Cohen[12] has conducted measurements inside the boundary layer, but for a weak initial disturbance, and at a large enough downstream distance such that the advective modes have decayed. His results indicate that Gaster's model is still valid, although non-linear effects do become important as the wave packet grows in amplitude at which point signs of a subharmonic resonance become apparent.

It should be made clear that the distinction between the advective and dispersive parts of a general disturbance is primarily a descriptive one. In the linear inviscid anal-

ysis, a clear theoretical distinction does arise and, as was discussed above, is associated with the singularity present in the Rayleigh equation at the critical layer. However, in the linear viscous analysis, the disturbance may represented by Orr-Sommerfeld modes. The wave portion is represented by the least stable modes, and the transient part, by higher, damped, modes. Thus one should not think that the advective portion cannot be described by wave modes, but rather that it is not usefully described in such terms. We should note that the viscous continuous spectrum may have a part in the boundary layer, but its role is not yet clear. For finite Reynolds number, there are only a finite number of Orr-Sommerfeld modes (see Mack[51]). Hence, an arbitrary disturbance cannot be represented completely by Orr-Sommerfeld modes and the continuous spectrum must be employed. However, one would expect that the boundary layer and the channel flow to be qualitatively similar, and so we would conjecture that the portion of the disturbance represented by the continuous spectrum will be relatively minor.

Morkovin[56] pointed out several years ago that finite amplitude disturbances might perturb the base flow sufficiently such that the traditional Tollmien-Schlichting route to transition might be bypassed directly by non-linear effects. This was the case in the results of Amini[3] who initiated an 'incipient spot' by means of a strong jet of air through a pin hole in the wall. However, Amini's study was limited mainly to mapping out the structure of that particular disturbance and did not consider localized disturbances in general, or the more basic mechanisms that contributed to the non-linear bypass mechanism.

1.2 Present Work

The present work is an investigation into the evolution of isolated disturbances in a laminar boundary layer. As has been made clear in the previous discussion, such disturbances can be thought of as being comprised of two parts: a dispersive part and a advective part. (Throughout the thesis, both 'advective' and 'transient' are used interchangeably to refer to the advective portion of a disturbance and similarly, both 'wave' and 'dispersive' refer to the wave part of a disturbance) The dispersive part, governed by normal mode solutions to the Orr-Sommerfeld equation, will be unstable at sufficiently high Reynolds numbers, and should behave much as the wave packet of Gaster[18] and Gaster & Grant[20]. The advective part, due entirely to the three-dimensional nature of the disturbance, is a little more of an unknown. According to the linear theory of Landahl[46], and Gustavsson[24], the advective part of the disturbance should grow algebraically initially. However, the theory is for inviscid flow, and clearly this will not be valid for all amplitudes and Reynolds numbers. At low amplitudes, the advective modes will be damped by viscosity, and similarly viscous effects will place a limit on the scale of regions of intense shear. (Landahl[45] estimated this to be $(\nu l/U')^{1/3}$ where l is a typical streamwise length scale, and U' is the mean shear). Another aspect of the advective part of the disturbance which remains to be determined more precisely is its structure, both through the boundary layer, and in the spanwise direction. The evolution of this structure as the disturbance propagates will also be of interest in this thesis. The effect of amplitude on the disturbance evolution is also discussed. For low amplitudes, we would expect that the linear theory will be a good approximation to the disturbance evolution. However, stronger amplitude disturbances will include nonlinear effects, and we shall show that the nonlinear bypass mechanism discussed by

Morkovin[56] is observed.

1.2.1 Organization of the Results

The investigation is comprised of several different approaches to the initial value problem in a laminar boundary layer. Experimental, analytical and numerical work has been completed, and both low and high amplitude disturbances have been investigated. The results presented in the thesis have been divided into two main parts. The first of these parts, discussed in Chapter 3, concerns the evolution of 'weak' disturbances. These disturbances are characterized by the fact that the transient portion does not grow and break down to turbulence, but decays as the disturbance propagates, leaving the wave packet which grows slowly according to linear theory. In contrast to this, the strong disturbances, which are discussed in Chapter 4, are characterized by the fact that the transient portion does not decay, but grows and leads directly to turbulent breakdown, bypassing the wave growth route to transition. Both Chapters 3 and 4 contain several approaches to the problem of the disturbance growth. The discussions begin with experimental results, but some theoretical calculations are presented in addition. For the weak disturbances two theoretical approaches are used: the linear initial value problem is solved numerically for an inviscid flow, and also the flat-eddy equations are used for weakly non-linear disturbances. The flat eddy analysis is continued for the strong disturbances in Chapter 4 and in addition to this, some results from a full Navier-Stokes numerical simulation are also presented.

In addition to the application of these results to the study of transition, there are also several issues that are raised which apply to the structure of fully turbulent flows. Many of the features that have been observed in the evolution of a disturbance in the

laminar boundary layer have also been observed by other researchers in conditional sampling of fully turbulent shear flows. The similarities and differences between the flows and the implications of these common features are discussed in Chapter 5.

The following chapter discusses many of the technical details concerning the experimental equipment and the methods used during the measurements. In addition, the documentation concerning the mean flow and the quality of the boundary layer in the wind tunnel are discussed here. Specific details concerning individual measurements will be addressed in the main discussion as they arise.

One note concerning the placement of figures and tables in the thesis. The figures referred to in the text are placed following the chapter in which they are first discussed. Tables are placed in the text on the page where they are referenced. A list of figures and a list of tables may be found at the begining of the thesis.

Chapter 2

Experimental Considerations

This chapter discusses the general details of the experimental set-up and the procedure used in taking measurements for this research. The wind tunnel facilities are described and the flow parameters used during the measurements are outlined. The quality of the basic mean flow is also discussed in some depth.

2.1 Wind Tunnel

The experiments described in this thesis were conducted in the Turbulence Research Laboratory in the department of Aeronautics and Astronautics at MIT. The details of the wind tunnel and the flat plate may be found in Mangus[52], but we shall outline the pertinent features here. The wind tunnel is a closed loop type with a test section 6.1 meters long, 1.22 meters high and 0.6 meters wide. The flat plate, made from aluminum, is 12.7mm thick and is mounted vertically, 10 cm from the tunnel side wall. The plate extends the entire length of the test section and to within 10 cm of both the tunnel floor and ceiling. A tapered leading edge with an elliptical tip is attached to the front of the plate which is joined to the floor and ceiling by a porous metal plate behind which are ducts for suction of the boundary layers which grow in the corners of the test section. This corner flow grows substantially further downstream, and it

contaminates the boundary layer on the flat plate at large downstream distances. For the present experiments this suction control was not used, although it has been used successfully for maintaining a high quality laminar boundary layer over the entire length of the test section (Cohen[12]). A right-handed coordinate system was defined with x as the streamwise direction, z, the spanwise direction and y the direction normal to the plate. The velocity components are defined accordingly, with the streamwise component written as a local mean plus a perturbation: $U(y) + u$, the normal component, v and the spanwise component, w.

2.2 Hot-wire anemometers

The flow measurements were made using constant temperature hot-wire anemometry. The hot-wire probes used, both for single wire measurements and two-wire measurements, were constructed in-house and typically had dimensions of less than 0.5 mm in length. Wollaston wire, 1.27 microns in diameter, was used for the sensing wire giving a typical L/D ratio of greater than 300. The probes were operated at a resistive overheat of 30%. The anemometer circuits used were built in-house and the circuit is shown in Figure 2.1. For measuring u and v components of velocity, a standard x-wire probe was built, having a box size of 0.4 mm. The probe for measuring u and w components was a swept-back 'v'-wire (see Figure 2.2).

The data was acquired using a Phoenix Data A/D system capable of digitizing upto sixteen channels simultaneously at an aggregate data rate of 350 KHz. the A/D was connected to a PDP 11-55 computer, which also controlled all the probe positioning, timing and all other aspects of the experimental procedure. Subsequent data processing

and graphics were performed on a MicroVax II. The hot wire probe was mounted on a traversing mechanism with four degrees of freedom: x, y, z and one rotational axis for x-wire calibration. The traverse was powered by stepping motors which were controlled by the PDP-11 via a Modulynx motion control system.

2.2.1 Hot-Wire Calibration

All of the hot-wire calibration was performed directly by the computer. No linearizers or signal conditioners were used. For single wire measurements, the wire was calibrated by fitting seven calibration points to a cubic polynomial. For dual wire measurements (both x-wires for measuring u and v, and v-wires for measuring u and w) a look-up table procedure was used. This method, described by Leuptow, Breuer and Haritonidis[49] fits a look-up table to the calibration data (taken at seven velocities and nine angles) and uses bi-linear interpolation to calculate the two components of velocity from a pair of raw hot-wire voltages E_1, E_2. Initial versions of the calibration procedure used the voltages directly as the variables for a cartesian look-up table, but a later procedure[22] converted E_1 and E_2 into radial coordinates which took advantage of the fan-like shape of the raw calibration data and allowed for a more accurate calibration with fewer table entries. In all cases, the error in the probe calibration $(u_{meas} - u_{actual})/u_{actual}$ was less than 0.5% in both u and v (or w). During the actual data acquisition, the hot-wire linearization was carried out by an assembly language routine on the PDP-11. This allowed for very fast conversion of the raw voltages to velocities, speeding up the data collection considerably. The calibration was checked frequently for drift to ensure that it was still valid, and provided that the tunnel and electronic equipment had been operating for some time and had achieved a thermal

equilibrium, the calibration typically remained accurate for several hours.

2.3 Disturbance Generator

The experiments presented here all concern the development of an initial disturbance introduced into a boundary layer flow. To introduce a disturbance, several methods were tried. Amini[3,4] used an air jet, introduced through a 1 mm hole in the wall and driven by the motion of an audio speaker. The disadvantage of this type of disturbance is that it is very small and very localized. The small spanwise dimension of the disturbance makes the detailed measurement of its structure somewhat difficult, and it is desirable to generate a disturbance with a larger spanwise dimension. Another, perhaps more serious, problem is that the positive disturbance - generated by an upward motion of the speaker which pushes air up through the hole - is completely different from the negative disturbance - generated by downward motion of the speaker, which sucks air down through the hole. This difference is because the upward motion of the speaker results in a jet of air injected to the boundary layer, while the downward motion of the speaker creates a uniform sink flow from the boundary layer and down through the hole. For the experiments presented here, it was necessary to have both a highly controllable disturbance, and to be able to produce disturbances identical in amplitude and structure, but with opposite sign. The disturbance generator eventually used, shown in Figure 2.3, was a small elliptical membrane, 9 mm by 17 mm, mounted flush with the wall at a distance 0.76 meters from the leading edge of the plate. The membrane was imbedded into a circular plug which could be rotated so that the long dimension of the membrane was either aligned with the flow or perpendicular to it. A pressure source was connected to the back side of the membrane via a solenoid-controlled valve. By activating the

valve, the membrane was exposed to an over-pressure and a small bump then formed on the surface of the flat plate. Closing the valve allowed the pressures to equalize and the membrane returned to its rest position, flush with the wall. The net effect was to produce a short, localized up-down motion at the wall. By connecting the membrane to a vacuum, instead of an over-pressure, a down-up wall motion could be achieved, producing the same disturbance but with opposite sign (this will be demonstrated in the next chapter).

The electric pulse to the solenoidal valve could be varied so as to vary the duration of the wall motion. The shortest cycle time (governed by the physical response-time of the valve) was found to be 4 milliseconds, and this was achieved by operating the valve, as shown in Fig. 2.3, at 40 volts (instead of the rated 12 volts) and in conjunction with a 200 ohm dropping resistor.

2.4 Mean Flow Characteristics

Extensive measurements were made to determine the quality of the mean flow in the test section. Two quantities were of special interest: the uniformity of the boundary layer across the span of the flat plate, and the extent to which the flow conformed to a Blasius boundary layer. The spanwise uniformity of the flow was characterized by measuring the displacement thickness (δ_*) at 1 cm intervals over a span of 80 cm at different x-locations. These measurements are summarized in Fig. 2.4. Initially, large and concentrated peaks in the displacement thickness δ_* were discovered and it was found that the location of these peaks corresponded to the location of seams in the screens in the settling chamber of the wind tunnel. The peaks in δ_* remained confined

to a very small spanwise extent (< 1 cm) as far as 3 meters downstream from the leading edge, and were accompanied by increased u' levels within the boundary layer. The last of four settling chamber screens was replaced, which removed the largest peaks, but as Figure 2.4 shows, some localized variations still persist and despite extensive efforts, the cause of these peaks has yet to be determined. At the worst point, the variation of δ_* is about 10% of the mean value at $x = 1$ meter. The cause of these bulges in the boundary layer are still a mystery. One possibility is that the seams of the screen created a wake with localized vorticity which then impinged on the plate at the leading edge and was stretched out in the streamwise direction. However, this does not explain the peaks present after the new screen was in place. A possible alternative explanation is that potential fluctuations from the boundary layer on the contraction wall (which was measured to be turbulent and of varying thickness across the span), were causing localized disturbances on the flat plate. A third idea was that separation in the diffuser of the tunnel, downstream of the fan, was somehow leaving a scar in the mean flow which persisted through the turning vanes, the honeycomb, four screens and the contraction. However, we were unable to positively correlate any single quantity with the location of the δ_* peaks, which remained at the same position with uncanny persistence.

Since the spanwise variations in the base flow are not symmetrical about the centerline, any effect they may have on the measurements should be detectable in strong asymmetric features in the measurements. No such deviations were observed in any of the experiments, indicating that the mean flow variations did not significantly affect the measurements. Excluding the 'bad' spot at $z = -12$cm the boundary layer on the flat plate showed very good agreement with the Blasius solution. The conformity of the boundary layer to the Blasius solution is shown in Figures 2.5 and 2.6. 78 profiles are plotted in Fig. 2.5, taken over 13 downstream stations from $x = 50$ cm to $x = 350$ cm

and at six spanwise locations: $z = \pm 5, \pm 20$ and ± 30 cm. The data is plotted in the non-dimensional Blasius coordinate: $\eta = y\sqrt{U/\nu(x - x_v)}$, using a consistent virtual origin x_v for all the profiles. The virtual origin is a result of slight flow non-uniformities in the vicinity of the plate leading edge. Figure 2.6 shows the growth of the displacement thickness (averaged over all spanwise locations) with downstream distance. The symbols show the measured growth while the curve plots the growth predicted by the Blasius solution. The good agreement between the measurements and the theoretical values in both Fig. 2.5 and Fig. 2.6 indicates that while the mean flow does have isolated spots of spanwise non-uniformity, its development is in accordance with the Blasius solution.

2.5 Flow parameters

Most of the experiments were conducted at a free stream velocity, U_∞, of 6 meters/second. As mentioned above, the disturbance generator was located at $x_0 = 0.76$ meters. Assuming that the mean flow can be described by the Blasius solution for the boundary layer, we can calculate the relevent flow parameters at $x_0 = 78$ m. These are given in Table 2.1.

The Reynolds number of 950 falls well above the critical Reynolds number for linear instabilities which is $Re_{\delta_*} = 520$[57]. According to Jordinson's[36] solutions to the Orr-Sommerfeld equation, at $Re_{\delta_*} = 950$, waves with a non-dimensional frequency, $\beta = 2\pi f \delta_* / U_\infty$, between 0.06 and 0.13 will be amplified. Figure 2.7 shows a power spectrum of the streamwise velocity taken inside the boundary layer at the a height where the local mean velocity is $0.3U_\infty$. The spectrum is plotted in normalized dB vs. frequency, shown in both non-dimensional units, β, and in Hertz. Several features of the

x_0	0.76 meters
U_∞	6.0 meters/second
Displacement thickness, δ_*	2.37 mm
Momentum thickness, δ_θ	0.92 mm
Boundary layer thickness, $\delta_{.99}$	6.9 mm
Re_x	304000
Re_{δ_*}	950

Table 2.1: Flow parameters for experimental data based on the Blasius solution for the boundary layer

flow noise can be identified. At the low frequency end, the sharp spikes in the spectrum result from the ambient noise in the system - the tunnel motor, etc. A broad hump in the spectrum, from $\beta = 0.07$ to 0.16 indicates the linearly amplified modes selected from the background noise, in good agreement with Jordinson's calculated values. The peak at 120 Hz is the contamination of the hot wire signal from the mains noise. This peak is in some ways an artifact of this specific measurement. The hot wire signals did have some 60 cycle background noise, and this is reflected in the power spectrum. However, during actual data collection, care was taken to ensure that the each member of the ensemble average was triggered at random in relation to the phase of the 60 cycle noise. This ensured that this noise was averaged out by the ensembling process and so it is not seen in the disturbance measurements.

2.6 Experimental Procedure

The structure of the disturbed flow, created by the membrane movement, was mapped out by positioning the hot wire probe at an (x, y, z) position downstream of the membrane and measuring the velocity trace as the disturbance advected past the probe. The measurement sequence was initiated by a pulse from the computer which triggered the membrane motion. After waiting a preset time, the velocity record, consisting of 512 points, was digitized at a rate sufficient to capture the disturbance signal (Typically about 300 μsecs). By measuring at several locations, a complete map of the structure could be assembled. Two kinds of flow maps were obtained by this procedure. By positioning the probe at $z = 0$ and at several y locations through the boundary layer, a vertical slice of the disturbance through the centerline of the structure was obtained. The second mapping that was performed was a horizontal slice through the disturbance at a fixed y/δ_* from the wall and at several z locations. From these two kinds of mapping, a good representation of the complete structure could be inferred. These measurements were carried out at several different x locations downstream from the membrane location (at $x = 0.76$ meters from the leading edge of the flat plate).

At each (x, y, z) position, 100 events of the disturbance's passage were measured and an ensemble average was then calculated. In all cases, the disturbance velocity was extremely coherent, and so the ensemble average is a very faithful representation of an individual event. As the disturbance grew and started to break down to turbulence, the coherence of the signals did, however, deteriorate. The averaging process was also

beneficial in reducing the random background noise. This was especially important at the edges of the disturbance, where the perturbation velocities were very weak ($u \approx$ 0.05% of U_∞), and the averaging was necessary to pick out the coherent signal from the incoherent fluctuations present in the flow.

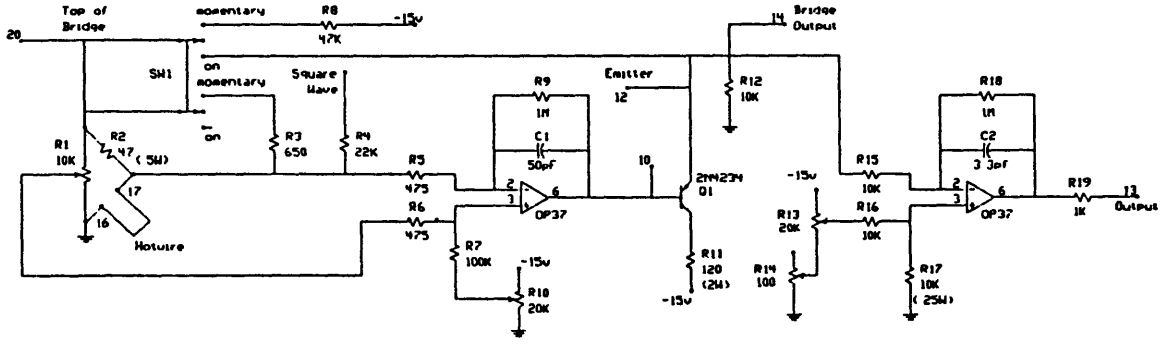

Figure 2.1: Hot-wire anemometer circuit diagram

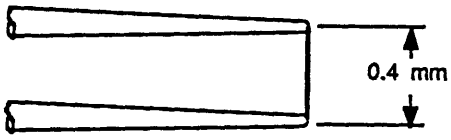

(a) Single wire probe

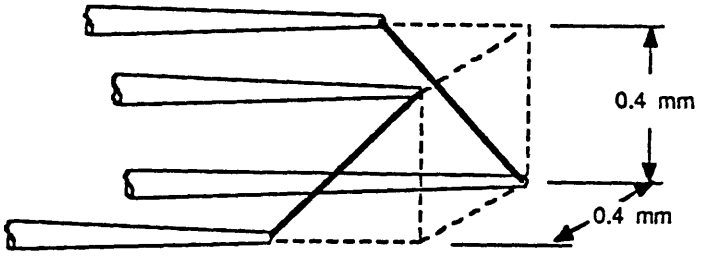

(b) X-wire probe for u and v components of velocity

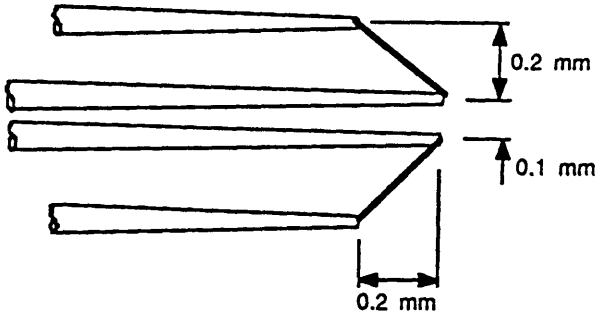

(c) V-wire probe for u and w components of velocity

Figure 2.2: Hot-wire probe geometry. Single wire for measuring u, x-wire for measuring u and v, and v-wire for measuring u and w.

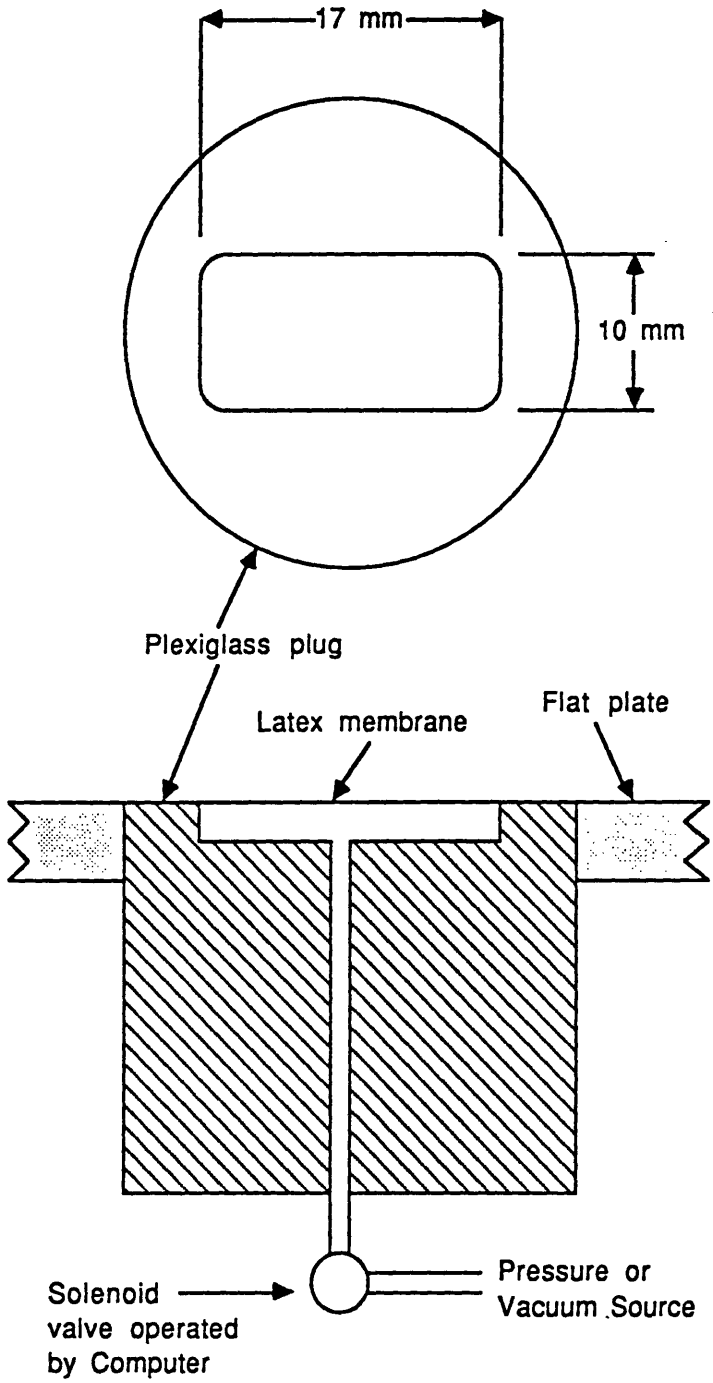

Figure 2.3: Schematic of the membrane used to generate localized disturbances in the boundary layer.

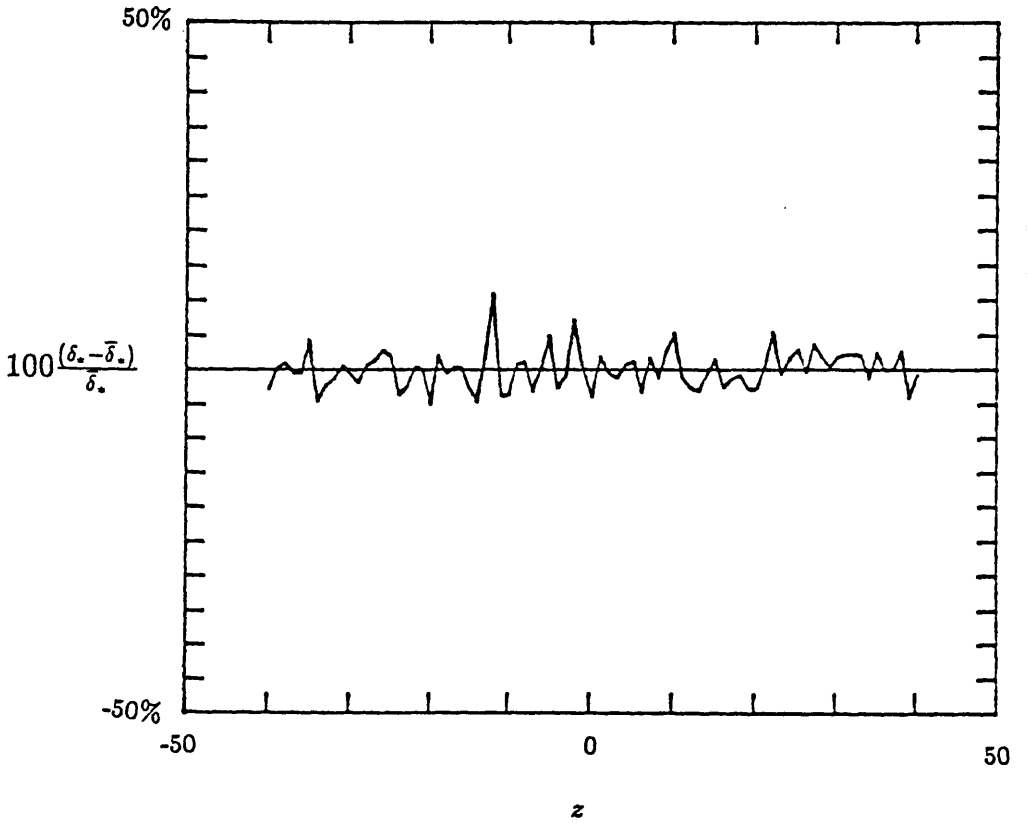

Figure 2.4: Variation of displacement thickness, δ_*, across the flat plate at $x = 1$ meter from the leading edge

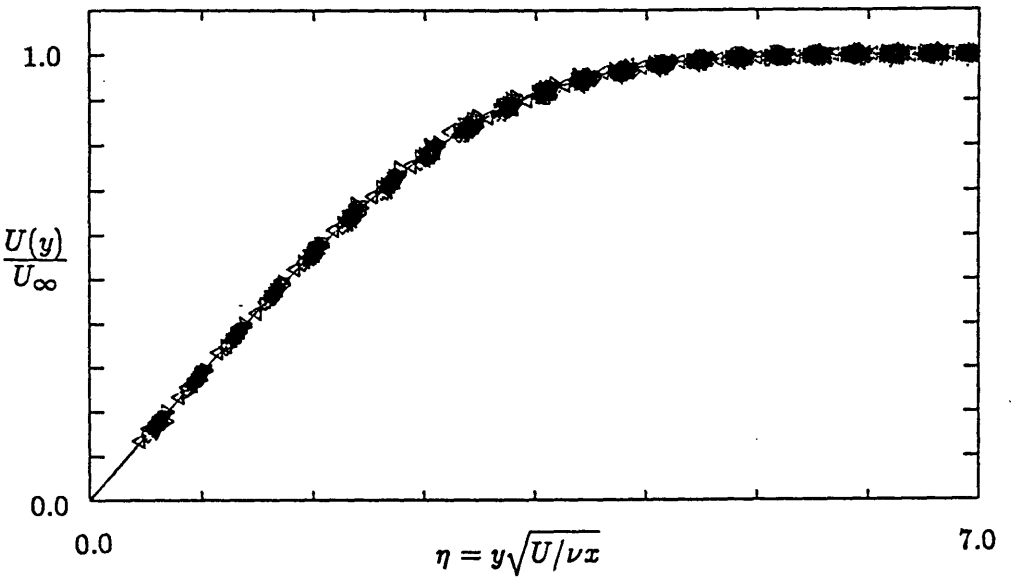

Figure 2.5: Velocity profiles taken at 78 locations at $x = \pm 5, \pm 20$ and ± 50 cm, $x = 50 - 350$cm in 25cm intervals. The data is plotted in the non-dimensional Blasius coordinate: $\eta = y\sqrt{U/\nu(x - x_0)}$

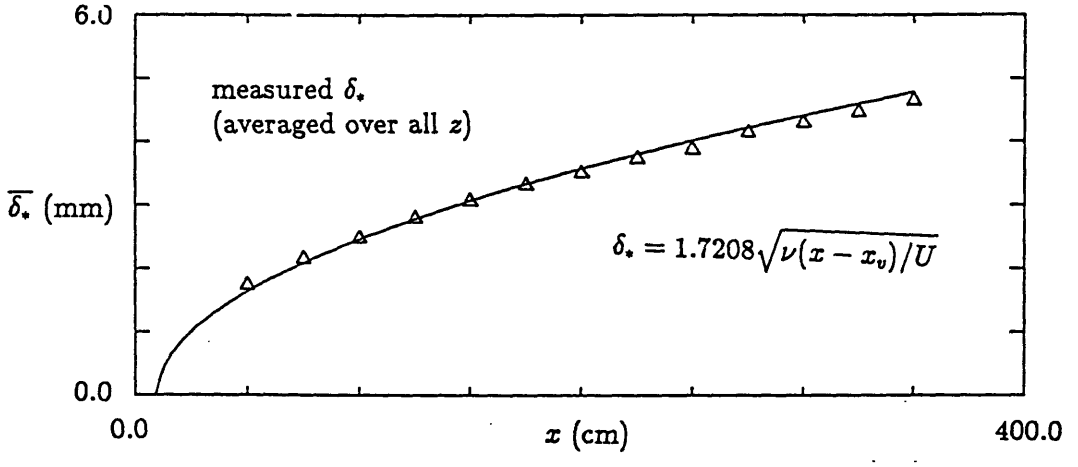

Figure 2.6: Development of δ_* with downstream distance. Symbols represent the measured δ_* (averaged over all spanwise locations). Curve represents the evolution predicted by Blasius theory.

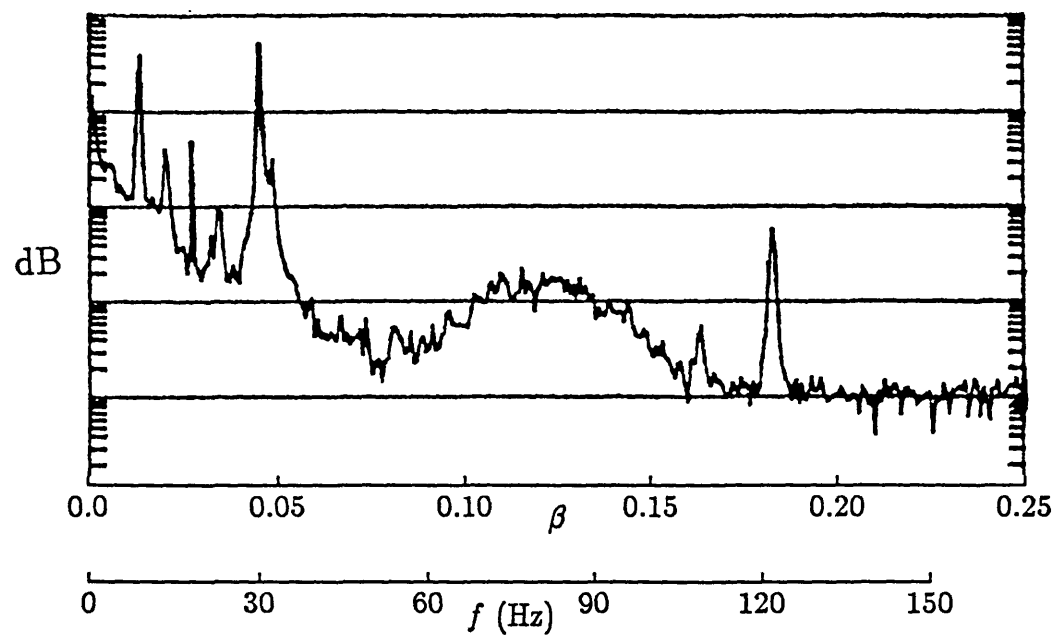

Figure 2.7: Power spectrum of the streamwise velocity inside the boundary layer where $u/U_\infty = 0.3$. Horizontal axis depicts both frequency in Hertz and non-dimensional frequency $\beta = 2\pi f \delta_* / U_\infty$.

Chapter 3

Weak Disturbances

This chapter discusses the evolution of weak disturbances in the boundary layer. The classification of a disturbance as being weak needs to be explained. A weak disturbance, in this context, is one in which the advective portion of the disturbance does not break down to form a turbulent spot. The overall development scenario, then, for this kind of disturbance is that the transient portion decays (through viscous diffusion) and the remaining disturbance is a slowly growing wave packet. Thus, the disturbance is ultimately unstable, but initially only to linear wave growth. It should be noted that a weak disturbance is not necessarily a linear one. In fact, the experimental results presented all involve weakly non-linear disturbances. However, many of the dominant processes observed in the evolution of the disturbance are linear processes, and so the linear initial value problem is solved in Section 3.2.1 so as to be able to examine these mechanisms in detail. A second theoretical approach, based on the Flat-Eddy model proposed by Russell and Landahl[63], is also used. This approach allows for the non-linear terms to be retained, but assumes that the horizontal pressure gradients may be neglected as a first approximation. This approach is examined in Section 3.2.2.

3.1 Experimental Work

A weak disturbance was generated by the membrane and mapped out in the $t - y$ plane on the centerline ($z = 0$) as described in the previous chapter. The amplitude of this disturbance, characterized by the peak-to-peak amplitude of the streamwise perturbation velocity at $\Delta x/\delta_* = 8$, was 2.2% of U_∞. A vertical 'cut' through the boundary layer was measured at several x-locations, starting at $\Delta x/\delta_* = 8$ and at regular intervals of approximately $8.5\delta_*$ thereafter. At each x-location, measurements were taken at 20 y positions through the boundary layer spanning a vertical height of $5\delta_*$. The vertical spacing was arranged according to a 1.5 power law so that there was increased resolution near the wall. All three components of velocity were measured but several problems with the measurement of the v component were encountered and these results had to be discarded. The problems in measuring v were associated with the contamination of the x-wire probe data by the spanwise velocity component of the disturbance and the strong spanwise shear layers in the streamwise velocity $\partial u/\partial z$. This issue is discussed in detail in Appendix A. The spanwise structure of the disturbance was measured with the v-probe, measuring both u and w at a fixed height in the boundary layer. The probe was positioned at a height where $u/U_\infty = 0.3$ which corresponds to $y/\delta_* = 0.5$. The disturbance was mapped out in the $t - z$ plane by taking measurements at 33 spanwise locations, evenly spaced at $1\delta_*$ intervals and spanning $z = \pm 16\delta_*$.

3.1.1 Streamwise Disturbance Velocities

The streamwise velocity perturbations at the different x-locations are shown in Figure 3.1a-d. In these figures, as in all subsequent figures, the disturbance is plotted with

the local mean velocity subtracted. The structure of the streamwise disturbance immediately behind the membrane is a direct result of the nature of the initial disturbance generation. A region of fluid with decreased velocity is produced by the membrane's upward motion which pushes up low-speed fluid from the near wall region of the boundary layer. On the subsequent downward motion of the membrane, the negative v velocity pulls down high-speed fluid from the upper part of the boundary layer, resulting in a region of accelerated fluid. This is the liftup effect that Landahl discusses[47] in which fluid elements lifted by the initial conditions retain most of their horizontal momentum (a mixing length argument) and it is this mechanism that is responsible for the transient modes of the disturbance.

Figure 3.1 indicates that the structure is tilted over in the downstream direction (Remember that Figure 3.1 is plotted against *time* and so the flow can be thought of as going from right to left). This is typical of the advective portion of a disturbance which travels at the local mean velocity[24,27]. The disturbance in the upper part of the boundary layer travels faster than the disturbance close to the wall, and so the effect is to tilt the whole structure over as it advects downstream creating an inclined shear layer in the flow. This shear layer can be seen throughout the sequence of pictures in Figure 3.1 and at successive downstream stations the disturbance tilts with an increasingly acute angle of inclination to the wall intensifying the shear layer accordingly. By $\Delta x/\delta_* = 42$, the inclination angle seems to have reached an equilibrium level at which point the forcing by the mean shear might be offset by viscous forces, which set a limit on the intensity of the shear layer. The local advection of fluid particles also results in the streamwise stretching of the disturbance as it advects downstream since the 'foot' of the disturbance closer to the wall travels slower than the 'head'.

After the initial formation of the shear layer, the amplitude of the disturbance decreases slightly, and then remains relatively constant as the structure moves downstream. From $\Delta x/\delta_* = 17$ onwards, the peak-to-peak amplitude of the u component hovers around 2 % of U_∞, and only by $\Delta x/\delta_* = 59$ does it begin to decay slowly. During this time, the structure grows by elongation, and its length increases linearly from about $25\delta_*$ at $\Delta x/\delta_* = 17$ to about $40\delta_*$ at $\Delta x/\delta_* = 68$ (Figure 3.2). Thus, although the perturbation velocity remains constant, the energy of the disturbance nevertheless grows as the structure increases in size. This is precisely situation for the algebraic instability that Landahl discussed[46], and without the effect of viscosity this growth would continue indefinitely. However, since the flow in reality is dissipative, the advective part of disturbance does decay slowly as it travels downstream, and on measuring far downstream, the shear layer was found to have completely disappeared.

The spanwise structure of the disturbance is shown in Figure 3.3a-f. This sequence is actually for a disturbance somewhat weaker than discussed above, and the peak-to-peak streamwise disturbance amplitude in this case is only 0.8% of U_∞. This decreased amplitude enables us more clearly to distinguish between the advective and wave portions of the disturbance but it also means that the disturbance becomes difficult to measure experimentally because of its very low amplitude.

The structure of the disturbed flow field immediately behind the disturbance generator again reflects the motion of the membrane. The regions of low-speed fluid, followed by high-speed fluid are consequences of the up-down motion of the membrane pushing up and pulling down fluid particles in the boundary layer. Small lobes are also seen on either side of the central perturbations. These too are natural consequences of the membrane's initial movement. The positive v caused by the membrane's upward mo-

tion is accompanied by a weaker negative v on either side necessitated by continuity. In an identical manner to the central motion, this downward motion brings with it high speed fluid from the upper flow, resulting in a small region of locally accelerated fluid. Thus, the initial structure of streamwise perturbation velocities can be explained by the vertical rearrangement of fluid elements caused by the normal velocity component of the initial disturbance field. As mentioned before, this is the lift-up effect in which the streamwise perturbation velocities result from the integrated effects of the normal velocities (the initial membrane motion).

We should take a moment at this stage and discuss the validity of inferring spatial information about the disturbance from the time series data. Clearly we are applying a Taylor hypothesis in this regard. This is justified since the disturbance does not change it's structure very significantly from one x-location to the next and is in a state of near equilibrium. The disturbance does however elongate as it passes by the probe, but even this is a fairly slow process and a general spatial picture can thus be approximated directly from the time series.

As we progress downstream, the evolution of the disturbance is observed in Figure 3.3a-f. By $\Delta x/\delta_* = 42$ the distinction between the advective and the dispersive parts of the disturbance becomes clear. The central core of the structure forms the advective part discussed thus far while the wave structure becomes more and more apparent at later x-locations. As with the previous case, the u perturbation remains at a fairly constant level, after an initial decay. The dispersive portion, seen as weak waves on the edge of the disturbance, is beginning to grow, and forms the swept-back wave-packet familiar from the results of Gaster and Grant[18,20]. These waves have a typical frequency which agrees well with the frequency of the most unstable mode

at that local Reynolds number. Further downstream, the transient portion continues to decay, while the accompanying waves grow and disperse as they propagate downstream. Since the membrane is symmetric about the x-axis, the disturbance should also show reflective symmetry. This symmetry is initially very good, but there are some differences in the amplitude of the structure on either side of the plane of symmetry. These differences are particularly noticeable in Figures 3.3c & d. However, since the measurements at subsequent x-locations seem to recover their symmetry, it is safe to assume that the actual disturbance does maintain symmetry fairly well, and that the apparent asymmetric structures in Figures 3.3c & d are experimental inaccuracies. The specific source of the inaccuracy remains unexplained but it could be due to a slight decrease in the pressure supplied to the membrane during the second half of the measurements at those x-locations. This would result in a weaker disturbance generated during the measurements on one side of the centerline which would explain the observed asymmetry.

One comment should be made concerning the long 'tail' behind the disturbance seen in Figure 3.3a. This tail is not a spurious consequence of experimental noise, but rather can be explained as being part of the transient disturbance. Since the advective portion travels with the local mean velocity, there must be a part of the disturbance, next to the wall, which does not propagate at all but rather remains at the point of generation. Thus, as the disturbance travels downstream, it is in fact 'pinned' to the wall at $x = x_0$, and stretched out from that point. The tail that Figure 3.3a shows is the evidence of this pinning. After the main disturbance has passed by, the slow-moving and weak tail still remains until it is dissipated by viscosity. At the subsequent downstream x-locations, we should still be able to see the tail, but because of its very low amplitude, it has already dissipated and is no longer visible.

3.1.2 Spanwise Disturbance Velocities

The spanwise structure of the spanwise velocity component is shown in Figures 3.4a-f. As with the streamwise perturbation, the structure of the w component at $\Delta x/\delta_* = 8$ strongly reflects the initial generation mechanism and the consequences of the lift-up effect. As discussed above, the upward motion of the membrane generates a positive v velocity and continuity dictates that accompanying this must be a downward motion on either side of the central core. This pattern implies that there must be an accompanying spanwise flow which converges towards the centerline at the bottom of the disturbance structure and diverges from the centerline higher up in the boundary layer. At $y/\delta_* = 0.5$ (where the measurements were taken), which is low in the boundary layer, a positive streamwise perturbation should therefore be accompanied by a converging flow and conversely, the downward membrane motion, resulting in a positive streamwise perturbation should be accompanied by a diverging spanwise flow. Indeed, this is what is observed in Figure 3.4a. As with the streamwise velocity perturbations, the w component changes as the disturbance progresses downstream from the compact format of the advective modes, to the swept-back and more extensive pattern of the wave-packet. The typical frequency of the w perturbation also changes from one associated with the membrane size, to the lower frequency associated with linear instability waves. The anti-symmetry of the w component of velocity is expected for a disturbance which is symmetrical in the u and v components with respect to its centerline and the experimental results show this anti-symmetry with remarkable accuracy.

3.1.3 Centerline Disturbance Velocities

The progression of the disturbance, and its transition from one dominated by advected modes to a dispersive wave packet can be examined in more detail by looking at the streamwise velocity signal along the centerline of the disturbance. This is shown in Figure 3.5 which shows the u signal from a station immediately behind the membrane to a station $\Delta x/\delta_* = 300$. As before, the signal behind the membrane reflects the motion of the membrane. The up-down motion creates a low-speed – high-speed velocity perturbation in the streamwise velocity signal. This initial amplitude is quite small, and the peak-to-peak amplitude of the first u signal is 0.8% of U_∞. As the disturbance moves downstream the transient stretches and decays, and at an x-location of about $\Delta x/\delta_* = 200$ the disturbance is comprised solely of a wave packet. The distinction between the transient and dispersive parts is also emphasized by looking at the propagation velocities of the disturbance at various stages of its development (shown in Figure 3.6). The propagation speed of the disturbance in its initial phase is $0.33U_\infty$ which agrees well with the local mean velocity at the height of measurement which was $0.3U_\infty$. This is what we would expect, as the advective modes do travel at the local mean velocity. In contrast to this, the phase speed of the wave-packet wave crests further downstream is $0.35U_\infty$ which is the typical speed for a Tollmien-Schlichting wave in a boundary layer. The velocities of the leading- and trailing-edges of the wave packet are $0.37U_\infty$ and $0.45U_\infty$ respectively, in good agreement with the envelope speeds measured by Gaster and Grant [20].

The development of the amplitude of the centerline disturbance velocity is shown in Figure 3.7. This is plotted in logarithmic coordinates and normalized by the amplitude at the first x station. Again, the distinction between the transient part of the distur-

bance and the dispersive part is evident. Initially, when the transient is dominant, the amplitude decays exponentially as the damped transient modes die out. After a region of transition, the wave packet establishes itself, and the disturbance grows exponentially with a spatial growth rate of about 0.005. This is a little lower than the rate predicted by linear theory, which is about 0.009, but falls within the limits of experimental accuracy. The exponential decay of the transient modes suggests that it is comprised of higher Orr-Sommerfeld modes which are quite heavily damped. This is a reminder that while the weak transient part of the disturbance exhibits different characteristics from the wave modes, the distinction between the two is a conceptual one and the governing mechanisms are ultimately the same.

3.1.4 Non-Linear Effects

Despite the low amplitude of this disturbance, weak non-linear effects were observed in the disturbance evolution. These effects were examined by creating the same initial disturbance as before, with the same initial amplitude, but with opposite sign. Physically, this was accomplished, as described in Chapter 2, by operating the membrane with a vacuum source in place of the usual pressure source. The spanwise structure of this 'negative' disturbance is seen in Figure 3.8. The initial velocity perturbations are almost identical in structure and amplitude but with opposite sign to those in Figure 3.3. The similarity includs the initial structure of the disturbance, the decay of the advective modes, the growth of the wave modes, and the weak tail pinned to the wall behind the disturbance. However, close examination of the later x-locations reveals that, for both signs of initial disturbance, at $\Delta x/\delta_* = 76$ the positive perturbations have split into two peaks off the centerline while the negative perturbations remain centered

at $z = 0$. These non-linear effects are only seen in the streamwise velocity component, and no measurable differences were apparent in the w disturbance velocity (Figure 3.4).

The weak non-linearity is again evident in Figure 3.10 in which the centerline streamwise velocity perturbation seen in Figure 3.5 (created by the normal up-down membrane motion) is re-plotted. Superposed on top of this, and plotted with a dotted line, is the centerline streamwise velocity perturbation of the negative disturbance (created by a down-up membrane motion), and *inverted* so as to highlight the similarities and differences between the two disturbances. Initially, in agreement with the contour plots of Figures 3.3 and 3.8, the two disturbances are identical in structure, but with opposite sign. However, by $\Delta x/\delta_* = 40$, differences between the two have appeared, and the effect of the non-linearity is apparent. As the transient decays, and the wave modes establish themselves as the remnant of the disturbance, the differences disappear and by $\Delta x/\delta_* = 260$ the wave packets are again identical and opposite. The nature of the non-linearity is clearly not strong and does not have a global effect on the disturbance since the linearly unstable wave numbers which remain after the transient has decayed are not affected by the non-linear action which was confined to the damped modes of the transient portion of the disturbance.

3.1.5 Summary

In this section the experimental investigation of weak disturbances was discussed. These disturbances can be conceived of as being comprised of two portions - a transient, or advective portion, and a wave, or dispersive, portion. The transient part derives from the details of the initial disturbance mechanism and is created by the lift-up of fluid elements by the membrane's movement. The fluid particles retain most of their streamwise

momentum resulting in significant streamwise velocity perturbations. This is in agreement with Henningson's results[27], who also found that the horizontal perturbations quickly dominated the flow field. The wave portion is comprised of a slowly growing linear wave packet surrounding the transient core. For a weak disturbance the transient modes decay exponentially, but the length of the disturbance grows linearly, presumably through the invisicd algebraic instability mechanism. A non-linear mechanism was also observed, but it was sufficiently weak such that the resultant linear wave packet was not affected.

3.2 Theoretical Work

Two approaches to the theoretical problem were attempted. The first is the standard linear initial value problem for a disturbance in a boundary layer, and the second is the application of the Flat Eddy model, developed by Russell and Landahl[63].

3.2.1 The Linear Initial Value Problem

Derivation of Equations and Numerical Method

The derivation of the equations for the linear, inviscid initial value problem is straightforward and our approach follows previous discussions of the problem (e.g. Case[10], Drazin and Reid[17], Henningson[27], etc) In this analysis, the flow is assumed to be inviscid and the mean flow is assumed to be two-dimensional and parallel. This assumption is valid for moderate times of evolution since the boundary layer thickness

increases according the square root of downstream distance:

$$\delta_* = \delta_{*0}\sqrt{\frac{x}{x_0}} \tag{3.1}$$

and for the typical cases investigated here ($x_0 = 0.76$ meters, $Re_{\delta_*} = 1000$) the boundary layer thickens only 10% over a distance of about $61x/\delta_{*0}$. The velocity is written as a mean component plus a perturbation:

$$u = U(y) + u(x,y,z,t) \tag{3.2}$$

$$v = v(x,y,z,t) \tag{3.3}$$

$$w = w(x,y,z,t) \tag{3.4}$$

We can then write the linearized Euler equations for an arbitrary three-dimensional disturbance:

$$u_t + Uu_x + U'v = -p_x \tag{3.5}$$

$$v_t + Uv_x = -p_y \tag{3.6}$$

$$w_t + Uw_x = -p_z \tag{3.7}$$

where the U' denotes dU/dy. The continuity equation for incompressible flow is given by

$$u_x + v_y + w_z = 0 \tag{3.8}$$

This system of equations is subject to the boundary conditions that the normal velocity be zero at the wall, and that all perturbations die out as $y \to \infty$, and as $x, z \to \pm\infty$.

The initial perturbation state is defined as

$$u(x,y,z;t=0) = u_0(x,y,z) \tag{3.9}$$

$$v(x,y,z;t=0) = v_0(x,y,z) \tag{3.10}$$

$$w(x,y,z;t=0) = w_0(x,y,z) \tag{3.11}$$

Taking the Fourier transform in the x and z planes, we obtain

$$(\frac{\partial}{\partial t}+i\alpha U)\tilde{u}+U'\tilde{v} = -i\alpha\tilde{p} \tag{3.12}$$

$$(\frac{\partial}{\partial t}+i\alpha U)\tilde{v} = -\tilde{p}_y \tag{3.13}$$

$$(\frac{\partial}{\partial t}+i\alpha U)\tilde{w} = -i\beta\tilde{p} \tag{3.14}$$

$$i\alpha\tilde{u}+\tilde{v}_y+i\beta\tilde{w} = 0 \tag{3.15}$$

where α and β are the wave numbers in x and z respectively and a tilde denotes a Fourier transformed quantity. By multiplying Equation 3.12 by $i\alpha$ and Equation 3.14 by $i\beta$, adding the two equations and using continuity (equation 3.15) we obtain an equation for the pressure:

$$\tilde{p}=\frac{-1}{k^2}[(\frac{\partial}{\partial t}+i\alpha U)\tilde{v}_y-i\alpha U'\tilde{v}] \tag{3.16}$$

where $k^2=\alpha^2+\beta^2$. Taking the y derivative, and substituting into Equation 3.13 we get the familiar Rayleigh Equation for the vertical velocity component

$$(\frac{\partial}{\partial t}+i\alpha U)(\frac{\partial^2}{\partial y^2}-k^2)\tilde{v}-i\alpha U''\tilde{v}=0 \tag{3.17}$$

One can also obtain equations for the horizontal velocity components by substituting Equation 3.16 into the horizontal momentum equations, 3.12 and 3.14:

$$(\frac{\partial}{\partial t}+i\alpha U)\tilde{u} = -\frac{\beta^2}{k^2}U'\tilde{v}+\frac{i\alpha}{k^2}(\frac{\partial}{\partial t}+i\alpha U)\tilde{v}_y \tag{3.18}$$

$$(\frac{\partial}{\partial t}+i\alpha U)\tilde{w} = \frac{\alpha\beta}{k^2}U'\tilde{v}+\frac{i\beta}{k^2}(\frac{\partial}{\partial t}+i\alpha U)\tilde{v}_y \tag{3.19}$$

These two equations can be simplified by rotating the horizontal coordinate system by introducing the transformation

$$\tilde{u}_1 = \frac{1}{k}(\alpha\tilde{u} + \beta\tilde{w}) \tag{3.20}$$

$$\tilde{w}_1 = \frac{1}{k}(\beta\tilde{u} - \alpha\tilde{w}) \tag{3.21}$$

in which $\tilde{u}_1$ is the velocity component perpendicular to the wave front and $\tilde{w}_1$ is the component parallel to the wave front. $\tilde{u}_1$ is also related to the derivative of the transformed vertical velocity $\tilde{v}_y$, and $\tilde{w}_1$ is related to the Fourier transform of the vertical vorticity. Applying this transformation to Equations 3.18 and 3.19, we obtain

$$(\frac{\partial}{\partial t} + i\alpha U)\tilde{u}_1 = \frac{i}{k}(\frac{\partial}{\partial t} + i\alpha U)\tilde{v}_y \tag{3.22}$$

$$(\frac{\partial}{\partial t} + i\alpha U)\tilde{w}_1 = -\frac{\beta}{k}U'\tilde{v} \tag{3.23}$$

These equations can be integrated directly using the transformed initial conditions yielding:

$$\tilde{u}_1 = \tilde{u}_{1_0}e^{-i\alpha U(y)t} + \frac{i}{k}(\tilde{v}_y - \tilde{v}_{y0}e^{-i\alpha U(y)t}) \tag{3.24}$$

$$\tilde{w}_1 = \tilde{w}_{1_0}e^{-i\alpha U(y)t} - \frac{\beta}{k}U'e^{-i\alpha U(y)t}\int_0^t \tilde{v}(y,t')e^{i\alpha U(y)t'}dt' \tag{3.25}$$

$\tilde{u}$ and $\tilde{w}$ can be retrieved by solving Equations 3.20 and 3.21 for $\tilde{u}$ and $\tilde{w}$:

$$\tilde{u} = \frac{1}{k}(\alpha\tilde{u}_1 + \beta\tilde{w}_1) \tag{3.26}$$

$$\tilde{w} = \frac{1}{k}(\beta\tilde{u}_1 - \alpha\tilde{w}_1) \tag{3.27}$$

Equations 3.24 and 3.25 illustrate well the additional term that the three-dimensionality presents in the evolution of a disturbance. The equation for $\tilde{w}_1$ is only non-zero for a disturbance both with a spanwise structure, and in a mean shear flow, and it is this

equation that contains the lift-up term described by previous investigators[44,24,27]. The second term in Equation 3.25 contributes when the integrated effect of the vertical velocity is non-zero and when there is a mean shear U'. Also note that for a sharper spanwise structure (i.e. for larger values of β) this effect will be more important.

In order to solve Equations 3.17, 3.22 and 3.23 either some simplifying assumptions must be made about the mean profile or the initial conditions, or one must resort to numerical methods of solution. Both Gustavsson[24] and Henningson [27] assumed piecewise linear profiles for the mean velocity profiles in a boundary layer and a plane Poiseuille flow respectively, and they were able to integrate the equations in closed form. The strength of this approach is that the different effects present in the solution are readily seen in the analytical solution, but the treatment of the mean profile by a series of linear segments does introduce some spurious behaviour in the solution, especially in the dispersive portion which is quite sensitive to the mean profile curvature. For the present work, the complete Blasius profile was used, and the equations were integrated directly using a finite-difference technique described in the following section.

Solution of the Linear Initial Value problem

The solution to this system of equations derives from the method used by Kim, Moin and Moser[40] at NASA Ames in their numerical studies of fully developed turbulent channel flow. Equation 3.17 was solved by breaking it into two equations:

$$\frac{\partial \nabla^2 \tilde{v}}{\partial t} = i\alpha(U''\tilde{v} - U\nabla^2\tilde{v}) \tag{3.28}$$

$$\nabla^2\tilde{v} = (\frac{\partial^2}{\partial^2 y} - k^2)\tilde{v} \tag{3.29}$$

This equation was discretized into J evenly spaced points in the normal direction, and centered differences were used to approximate vertical derivatives. A Crank-Nicolson scheme was used to march forward in time, ensuring stability. The resulting finite difference equations obtained are:

$$\nabla^2\tilde{v}_j^{n+1} - \nabla^2\tilde{v}_j^n = i\alpha\Delta t(U_j''\frac{\tilde{v}_j^{n+1}+\tilde{v}_j^n}{2} - U_j\frac{\nabla^2\tilde{v}_j^{n+1}+\nabla^2\tilde{v}_j^n}{2}) \tag{3.30}$$

$$\nabla^2\tilde{v}^n = \frac{\tilde{v}_{j+1}^n - 2\tilde{v}_j^n + \tilde{v}_{j-1}^n}{\Delta y^2} - k^2\tilde{v}_j^n \tag{3.31}$$

where the superscript refers to the current time level and the subscript refers to the vertical level. This system of equations may be written in matrix form for a vector $\tilde{\mathbf{v}}^n$ which represents the complete vertical disturbance velocity at time level n: $\tilde{v}_j^n, j = 1 \ldots J$. Writing the equations in this form and after some simple matrix operations we obtain:

$$(\mathbf{I}+i\mathbf{R})\mathbf{D}\tilde{\mathbf{v}}^{n+1} = (\mathbf{I}-i\mathbf{R})\mathbf{D}\tilde{\mathbf{v}}^n + i\mathbf{S}(\tilde{\mathbf{v}}^{n+1}+\tilde{\mathbf{v}}^n) \tag{3.32}$$

where $\mathbf{R}$ and $\mathbf{S}$ are diagonal matrices associated with the mean profile:

$$\mathbf{R}_j = \frac{\alpha\Delta t U_j}{2} \tag{3.33}$$

$$\mathbf{S}_j = \frac{\alpha\Delta t U_j''}{2} \tag{3.34}$$

$\mathbf{D}$ is the (tri-diagonal) matrix associated with the Laplacian derivative in the normal direction (Equation 3.31) and $\mathbf{I}$ is the identity matrix. After some further simple manipulations, we arrive at an equation for advancing the vertical disturbance velocity:

$$\tilde{\mathbf{v}}^{n+1} = (\mathbf{D}+i(\mathbf{RD}-\mathbf{S}))^{-1}(\mathbf{D}-i(\mathbf{RD}-\mathbf{S}))\tilde{\mathbf{v}}^n \tag{3.35}$$

It should be noted that for fixed $\alpha, \beta, \Delta y$ and Δt, all of these matrices are constant and need to be evaluated and combined only once, at $t = 0$. In order to calculate the disturbance velocity at any subsequent time we need only apply the resultant matrix

iteratively to the $\tilde{\mathbf{v}}^n$ array. The matrices are also all tri-diagonal which allows for very fast manipulation and inversion during the computational cycle.

Equation 3.23 can also be written in matrix form:

$$(\mathbf{I}+i\mathbf{R})\tilde{\mathbf{w}}_1^{n+1} = (\mathbf{I}-i\mathbf{R})\tilde{\mathbf{w}}_1^{n} - \mathbf{T}(\tilde{\mathbf{v}}^{n+1}+\tilde{\mathbf{v}}^{n}) \tag{3.36}$$

where the matrix $\mathbf{R}$ is the same as above and $\mathbf{T}$ is another constant diagonal matrix:

$$\mathbf{T} = \frac{\Delta t \beta U'}{2k}\mathbf{I} \tag{3.37}$$

This equation may be integrated at the same time as the Rayleigh equation (Eqn 3.30) utilizing the current values for $\tilde{\mathbf{v}}^n$ and $\tilde{\mathbf{v}}^{n+1}$.

The computation is made even more simple by making use of the symmetries inherent in this system of equations. It can be shown readily that equation 3.17 has the following symmetry properties:

$$\tilde{v}(-\alpha,\beta) = \tilde{v}^*(\alpha,\beta) \tag{3.38}$$

$$\tilde{v}(\alpha,-\beta) = \tilde{v}(\alpha,\beta) \tag{3.39}$$

similarly, for Equations 3.22 and 3.23:

$$\tilde{u}_1(-\alpha,\beta) = -\tilde{u}_1^*(\alpha,\beta) \tag{3.40}$$

$$\tilde{u}_1(\alpha,-\beta) = \tilde{u}_1(\alpha,\beta) \tag{3.41}$$

$$\tilde{w}_1(-\alpha,\beta) = \tilde{w}_1^*(\alpha,\beta) \tag{3.42}$$

$$\tilde{w}_1(\alpha,-\beta) = -\tilde{w}_1(\alpha,\beta) \tag{3.43}$$

where a * denotes the complex conjugate of a quantity. This implies that if the initial conditions meet these symmetry requirements, then we only need to carry out the

calculations for $\alpha, \beta > 0$. The symmetry in β will be naturally satisfied if the initial condition is symmetric with respect to the $z = 0$ axis.

Initial Conditions

The initial disturbance was chosen so as to be localized, to satisfy continuity, and to be a good approximation to the initial disturbance produced in the previously described experiments. The initial conditions, shown in Figure 3.11 had the form of a pair of counter rotating streamwise vortices. This disturbance, similar to the one used by Russell and Landahl[63] and also by Henningson [27], is derived from a two-dimensional stream function:

$$u = 0; \qquad v = -\frac{\partial \Psi}{\partial z}; \qquad w = \frac{\partial \Psi}{\partial y} \tag{3.44}$$

where

$$\Psi = A\bar{x}\bar{z}\bar{y}^3 e^{-\bar{x}^2-\bar{y}^2-\bar{z}^2} \tag{3.45}$$

and $\bar{x}, \bar{y}, \bar{z}$ are coordinates scaled by some characteristic lengths: l_x, l_y and l_z:

$$\bar{x} = x/l_x; \qquad \bar{y} = y/l_y; \qquad \bar{z} = z/l_z \tag{3.46}$$

For the present results the scaling lengths used were: $l_x = 5\delta_*, l_y = 1.2\delta_*$, and $l_z = 6\delta_*$; chosen so as to best approximate the experimental conditions. The amplitude factor A was chosen to approximate the experimental conditions. One should be careful not to confuse the value of A with the amplitude described in the previous section which referred to the peak-to-peak amplitude of the resultant disturbance. The two are not the same (at all), and should not be confused. At time $t = 0$ the center of the disturbance is located at $x = 0, z = 0$.

Results of Initial Value Problem

Equations 3.35 and 3.36 were solved numerically using standard routines for tri-diagonal matrices. The calculation used 64 modes in α and 32 modes in β. The computational domain was a box, $200\delta_*$ in the streamwise direction and $50\delta_*$ in the spanwise direction. The vertical direction was discretized into 41 equally spaced points from $y/\delta_* = 0$ to 6. The boundary conditions were that the vertical velocity be zero at the wall: $v(0) = 0$, and decay exponentially in the free stream: $v \propto e^{-ky}$. Fast Fourier Transforms were used to convert the final results from wavenumber space back to physical space, and the above-mentioned symmetry properties of the equations and initial conditions were used to make the computations more efficient.

Figure 3.12 shows the streamwise disturbance velocity, plotted in the $x - y$ plane at three times: $t = 25, 50$ and 75. In this figure, and in subsequent theoretical results, the horizontal axis is x (not t as in the experimental data), and the flow is from left to right. The sequence of snap-shots show the development of the disturbance and bear a strong resemblance to the experimental data. Initially, there is no u component, but as a result of the initial conditions lifting up fluid elements vertically, the familiar low-speed – high-speed patches of fluid are seen, and the tilting by the action of the mean shear is also observed. As with the experimental data, the action of the mean shear is to tilt the structure over and to stretch it out in the streamwise direction. This creates an internal shear layer which is continually intensified by the streamwise elongation of the structure. Since there is no viscosity to limit the shear layer thickness by diffusion of the local vorticity in the shear layer, it continues to intensify with increasing time. Another result to note is the increasing amplitude of the disturbance. One should remember that this is an inviscid calculation, and hence there is no growth or decay of waves. All

modes are neutrally stable. This means that the growth of the disturbance is not due to an instability, but rather it is due to the liftup of fluid elements by the v component of the initial disturbance. As v decays (see Figure 3.13), this liftup will end, and at that point the disturbance amplitudes will not increase any further. The algebraic instability mechanism discussed by Landahl[46] predicts that the energy of the disturbance will grow linear with time provided

$$\int_{-\infty}^{\infty} v_0 dx \neq 0 \tag{3.47}$$

For this particular choice of initial conditions, this integral *is* equal to zero, and so we would not expect to see the algebraic growth for long times for this specific calculation.

The spanwise structure predicted by the linear theory is shown in Figure 3.14. The strong similarity with the experimental results confirms that the choice of initial conditions in order to match the experimental results was an appropriate one. In this view, the distinction between the transient and dispersive modes is again apparent. As before, the streamwise structure at first reflects the initial conditions, including the side lobes representing the return flow of the initial eddy structure. As time progresses, the transient core increases in strength, but in addition, the wave structure on the side of the disturbance also develops. As already noted, the lack of growing modes in the inviscid case requires that all growth shown in the streamwise velocity component be a result of the liftup effect and the subsequent action of the mean shear. The dominant nature of the liftup effect is illustrated in Figure 3.15 in which the contribution to u velocity component from the vertical vorticity component, w_1 is plotted at $t = 75$. The flow pattern from the w_1 component alone, which is only present in a three-dimensional disturbance, is almost indistinguishable from the full solution (Figure 3.14c), indicating that for a localized disturbance, the three-dimensionality is the dominant feature of the flow. One should be careful not to confuse the u_1 and w_1 parts of the flow with the tran-

sient and dispersive parts of the disturbance discussed earlier. Figure 3.15 shows that the w_1 portion of the disturbance contains both the advective part of the disturbance as well as the dispersive part.

The vertical component of velocity is shown in Figures 3.16 and 3.17. The picture here is quite different from that of the streamwise and spanwise components, and it serves to highlight the qualitatively different behaviours of the normal and the horizontal components of velocity. The normal velocity essentially maintains it's initial vertical structure, and does not show the formation of the shear layer, or any other aspects of the transient modes. This behaviour is expected since the v component is governed solely by the Rayleigh equation (Equation 3.17), and thus is only related to pressure. The horizontal velocities are governed by the two auxiliary equations (Equations 3.18,3.19) which, in addition to being driven by the vertical velocity, are also coupled to the initial conditions and the three-dimensionality of the disturbance field. This difference between the two velocities is essential. Figure 3.17 illustrates this further. Whereas the horizontal velocities showed the growth of the transient at the core of the disturbance, the normal velocity does not exhibit this at all, but only shows the development of the wave field (which is, of course, the pressure wave dictated by the Rayleigh Equation). It does appear that the amplitude of the waves are decaying as time increases, and this would seem to contradict the neutrally stable solutions of the inviscid equations. However, the wave *energy* remains constant, but since the waves disperse as they propagate, the wave amplitudes must decay accordingly. Since the dispersion is in two directions, x and z, we would expect v to decay as $1/t^2$.

The amplitude evolution of the disturbance is summarized in Figure 3.13 which plots the peak-to-peak disturbance amplitude as a function of time. From $tU/\delta_* = 0$ to

about 40 the growth is linear and this growth is the initial lift-up of fluid elements by the vertical velocity. For larger times, v decays as we would expect, and consequently, the growth in the horizontal velocities slows. We do not see a leveling off of the u amplitude as was observed in the experimental results. This is because the v component does not decay very fast and so a relatively long time is required for the lift-up process to finish. As discussed earlier, the v component should decay as $1/t^2$. However, the calculations indicate that it is a slower decay, more like $1/t$. This might be due to the limited spanwise size of the computational domain which could force the disturbance to behave in a two-dimensional manner and would dictate a $1/t$ decay rate. The streamwise extent of the domain also becomes a limiting factor for large times. By $t = 150$, the disturbance has stretched so much that it exceeds the computational box and the influence of adjacent disturbances (via the periodic boundary conditions) probably affects the solution. This might account for the strange behaviour in the w component at large times.

3.2.2 Flat-Eddy Model

The Flat-Eddy model, introduced by Russell and Landahl[63] represents a different approximation to the flow than the linear problem discussed above. Whereas in the linear problem the approximation is that the disturbance velocities only interact with the mean flow, this assumption is not needed in the flat-eddy approximation. Instead, as the name might suggest, the assumption is made that the vertical scale of the disturbance l_y is much smaller than the horizontal scales l_x, l_z and that the eddy appears much like a pancake, or a strip of bacon. As will be discussed later on, this approximation allows us to examine the transient portion of the disturbance without the low-amplitude restriction of the linear theory

As with the linear problem discussed in the previous section, we shall assume that the flow is incompressible, parallel and inviscid. The flat-eddy equations are derived by looking at the initial value problem in a Lagrangian reference frame. In this approximation, we assume that momentum is conserved in the horizontal plane and we solve the system by integrating the continuity equation in Lagrangian coordinates. (For a detailed derivation and discussion of the model, see Russell and Landahl[63], and Landahl[47])

Derivation of the Flat-Eddy equations

The equations of motion in a Lagrangian frame of reference represents the flow field in terms of the position of individual fluid elements. Each fluid particle is marked at time $t = 0$ by the cartesian coordinate $(\xi(0), \eta(0), \varsigma(0))$ and that particle's location at subsequent times is denoted by $(\xi(t), \eta(t), \varsigma(t))$. In Lagrangian coordinates, the continuity equation is simply represented by the Jacobian which dictates that volumes in Eulerian space (x, y, z) are conserved in Lagrangian space (ξ, η, ς):

$$\frac{\partial(x, y, z)}{\partial(\xi, \eta, \varsigma)} = 1$$

writing explicitly the second component of this system of equations, we get three equations relating (x, y, z) to (ξ, η, ς):

$$\frac{\partial \xi}{\partial y} = x_\varsigma z_\eta - x_\eta z_\varsigma \tag{3.48}$$

$$\frac{\partial \eta}{\partial y} = x_\xi z_\varsigma - x_\varsigma z_\xi \tag{3.49}$$

$$\frac{\partial \varsigma}{\partial y} = x_\eta z_\xi - x_\xi z_\eta \tag{3.50}$$

The Euler equations, in Lagrangian coordinates are almost trivial:

$$\frac{Du_i}{Dt} = -\frac{\partial p}{\partial x_i} \tag{3.51}$$

The x and z momentum equations can be integrated once:

$$u = U(y) + u_0 - \int_0^t \frac{\partial p}{\partial x} dt \tag{3.52}$$

$$w = w_0 - \int_0^t \frac{\partial p}{\partial z} dt \tag{3.53}$$

and integrated again:

$$x = \xi + (U(y) + u_0)t - \int_0^t (t - t') \frac{\partial p}{\partial x} dt' \tag{3.54}$$

$$z = \varsigma + w_0 t - \int_0^t (t - t') \frac{\partial p}{\partial z} dt' \tag{3.55}$$

Thus far, the equations are exact (although inviscid). Landahl[47] showed that for an eddy whose typical vertical scale l_y is small compared to its horizontal scales, the pressure terms are of order ϵ and may be neglected for moderate times. By neglecting the pressure terms, we can substitute Equations 3.54 and 3.55 into Equation 3.50, which yields a system of ordinary differential equations for the Lagrangian coordinates:

$$\frac{d\xi}{dy} = -U(y)_\eta t - u_{0\eta} t - U(y)_\eta w_{0\varsigma} t^2 + (u_{0\varsigma} w_{0\eta} - u_{0\eta} w_{0\varsigma}) t^2 \tag{3.56}$$

$$\frac{d\eta}{dy} = 1 - v_{0\eta} t + (u_{0\xi} w_{0\varsigma} - u_{0\varsigma} w_{0\xi}) t^2 \tag{3.57}$$

$$\frac{d\varsigma}{dy} = -t w_{0\eta} + U(y)_\eta w_{0\varsigma} t^2 + (u_{0\eta} w_{0\xi} - u_{0\xi} w_{0\eta}) t^2 \tag{3.58}$$

These equations can be easily integrated using standard ODE techniques to give $\xi(y), \eta(y)$ and $\varsigma(y)$ for any given fixed (x, z)-location and time t. By sweeping through several (x, z) pairs, one can calculate the Lagrangian coordinates associated with the entire Eulerian field at any given time. The Lagrangian coordinate at a point (x, y, z) informs

us of where the fluid particle at that point originated, and since we have neglected the pressure forces in this approximation, the velocity of that particle will not have changed in the intermediate time. Thus, one can construct the Eulerian velocity field from this information.

The motivation behind this derivation is clear. From the results thus far we have seen that for a general disturbance, the transient part plays an extremely important role in the disturbance's evolution. In the linear initial value problem discussed above, the transient portion was represented by two equations for the horizontal velocity field which depended on the initial conditions and specifically on the spanwise structure of the initial disturbance. This is the equation for the vertical vorticity that Benney & Gustavsson[5] and Henningson [27] discussed. The flat-eddy equations derived here directly model the vertical vorticity which represents the transient portion, while ignoring the pressure effects which model the wave modes of the disturbance. In formulating the equations in this manner, we have been able to retain all of the non-linear terms in the equations. This should allow a more detailed examination of finite amplitude effects. However, caution must be used since the neglect of the pressure terms will limit the validity of results for strongly non-linear flows with sharp gradients. Similarly, for large times, the integrated effects of pressure will introduce significant errors into the calculations.

Another aspect of the flat-eddy approximation that should be noted is that since wave modes are excluded from the solution, not only will the wave portion of the disturbance not be modeled, but also any secondary instabilities that might arise from the mean flow distortion will not be realized in the calculations.

Results and Discussion

The flat-eddy equations, (Eqns 3.56 - 3.58) were solved using a standard fourth-order Runge-Kutta integration technique. The initial conditions used were as described in the previous section. Figure 3.18 shows the evolution of the disturbance at three times, $tU/\delta_* = 25, 50$ and 75. Several features that have been seen in both the experiments and the linear theory are present here. One first notices the establishment of the streamwise perturbation velocities by the vertical motion of the initial disturbance, and how the mean velocity tilts the structure over forming an internal shear layer in the boundary layer. As time increases, the tilting continues until a sharp, intense shear layer is formed. In the real flow, this was abated by the diffusive action of viscosity, but since the calculations are inviscid, the shear layer in the theoretical studies is considerably sharper than when compared with the experimental results. We also see the intensification of the downstream low-speed side of the disturbance at the expense of the high-speed region further upstream. This is in agreement with the experimental data which also shows a preference for the low-speed side of the disturbance. The other feature which is reminiscent of the experimental results is the long tail that trails behind the disturbance, leading back to the initial location of the counter-rotating eddies. This tail, as with the experimental data, is due to the fact that the structure is 'pinned' to the wall close to $y = 0$. Since the local velocity there is almost zero, the disturbance hardly moves and so drags its tail behind as the rest of the structure moves at the faster local velocities present in the upper part of the boundary layer.

Figure 3.19 shows the spanwise structure of the streamwise disturbance velocity calculated by the flat-eddy equations. For short times, the structure of the disturbance is very similar to both the linear theory and the experimental results, and since this

initial structure is determined by the liftup of fluid elements, this agreement is not surprising. For longer times, the essential features of the linear theory are reproduced. The front part of the disturbance propagates more-or-less unchanged except that the central low-speed region intensifies as it travels downstream. The upstream side of the disturbance has quite a different behaviour. It is stretched out and decreases in amplitude as it travels. This is in qualitative agreement with the linear theory, although here the decrease in the amplitude and the elongation of the contours is more marked than in the linear theory. Figure 3.20 shows the same view as Figure 3.19 except that the initial condition was of opposite sign, i.e. $A = -0.05$. Here, the weakly non-linear effects seen in the experiments are also observed, although a direct association is not perfect. The negative disturbance has a similar structure to the positive disturbance but it is not quite equal and opposite. The negative perturbations in Fig. 3.20 are all slightly larger than their equivalent positive perturbation in Fig. 3.19 indicating that the non-linear effects amplify the low-speed regions preferentially. This seems to be born out by the experimental data in which the low-speed perturbations are consistently larger in amplitude than the positive perturbations. Although the main features of the structure are reproduced by the flat-eddy calculations, the agreement is somewhat tentative. This, perhaps, is not surprising since the flat-eddy model is only modelling the advective terms, and for the weak disturbances, those terms are ultimately not the important features of the disturbance structure. One would expect that for the stronger disturbance, in which the transient plays a more dominant role, the flat-eddy calculations might be more appropriate.

3.2.3 Summary

This section has described two approaches to modeling the evolution of weak disturbances. The first, the linear initial value problem, illustrates well the distinctions between the transient and the wave portions of the disturbance as well as emphasizing the relative importance of the vertical vorticity modes in defining the evolution of a three-dimensional disturbance. The linear solutions exhibits the formation of an internal shear layer through the liftup of fluid and its algebraic growth, both associated with the three dimensional nature of the disturbance. The second theoretical approach, the flat-eddy model, looks only at the transient portion of the disturbance, and captures well the formation of the shear layer and several features of the disturbance evolution. The weak non-linearity seen in the experimental results is also modeled by the flat-eddy theory although the correspondence is less convincing. Both of the theoretical models are inviscid approximations and so the disturbance evolves undamped by viscosity. This means that while the transient part from a low-amplitude real disturbance will eventually decay, it grows unchecked in the numerical simulations.

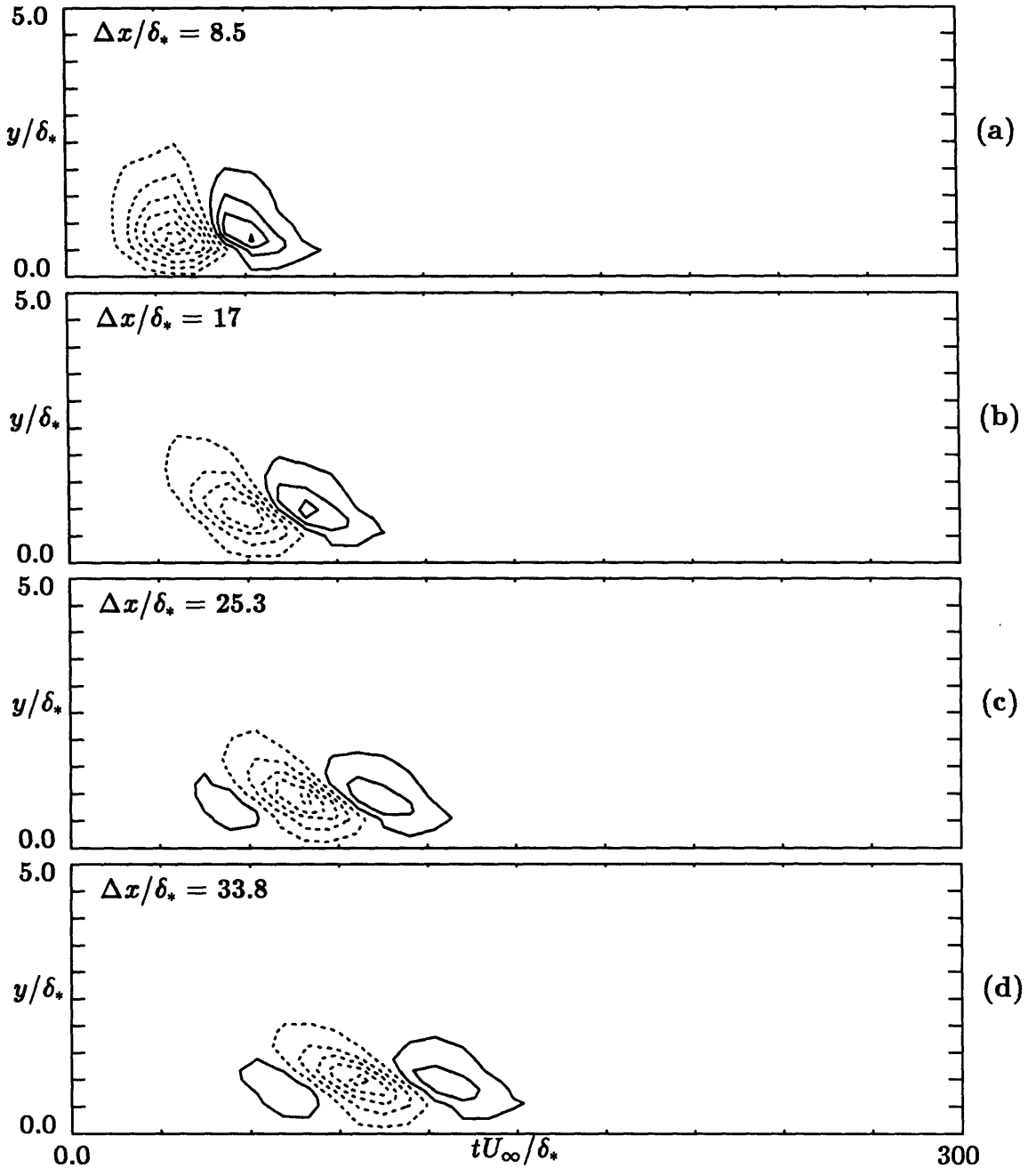

Figure 3.1: Experimental data. Contours of streamwise perturbation velocity at $z = 0.0$. Contour levels: $0.003U_\infty$. Solid lines represent positive contours, dotted lines represent negative contours.

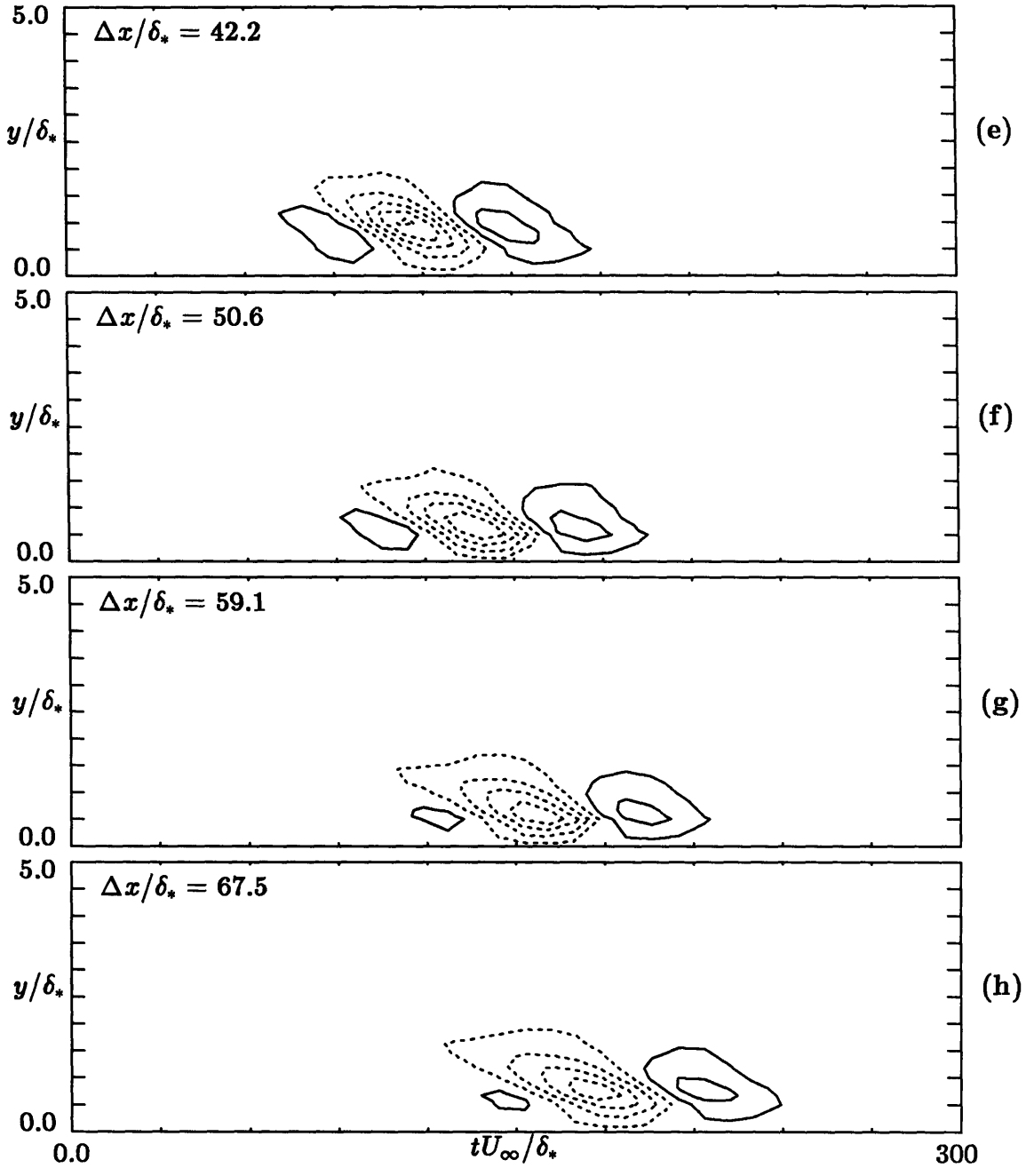

Figure 3.1: (Continued). Experimental data. Contours of streamwise perturbation velocity at $z = 0.0$. Contour levels: $0.003U_\infty$. Solid lines represent positive contours, dotted lines represent negative contours.

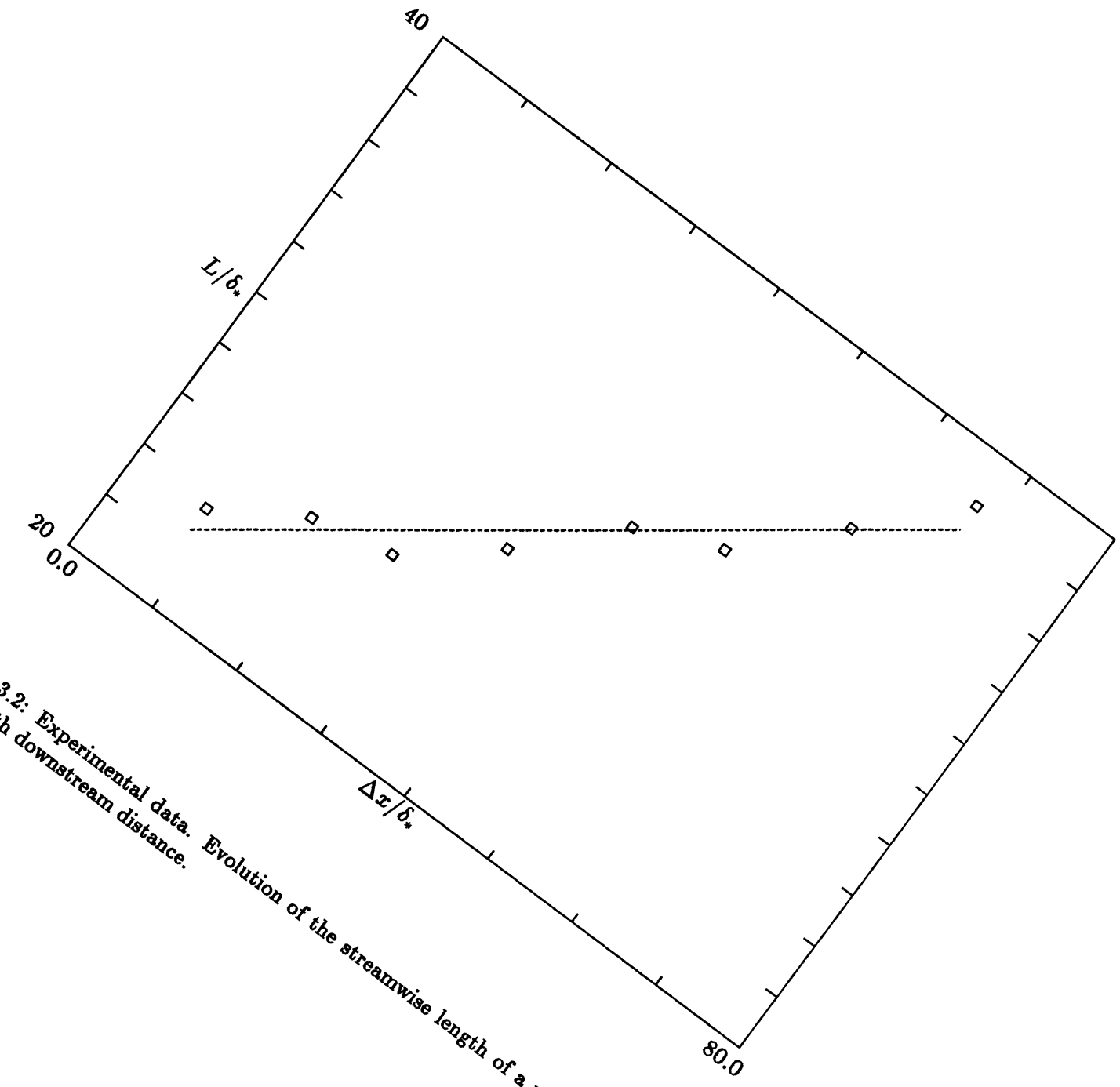

Figure 3.2: Experimental data. Evolution of the streamwise length of a weak disturbance with downstream distance.

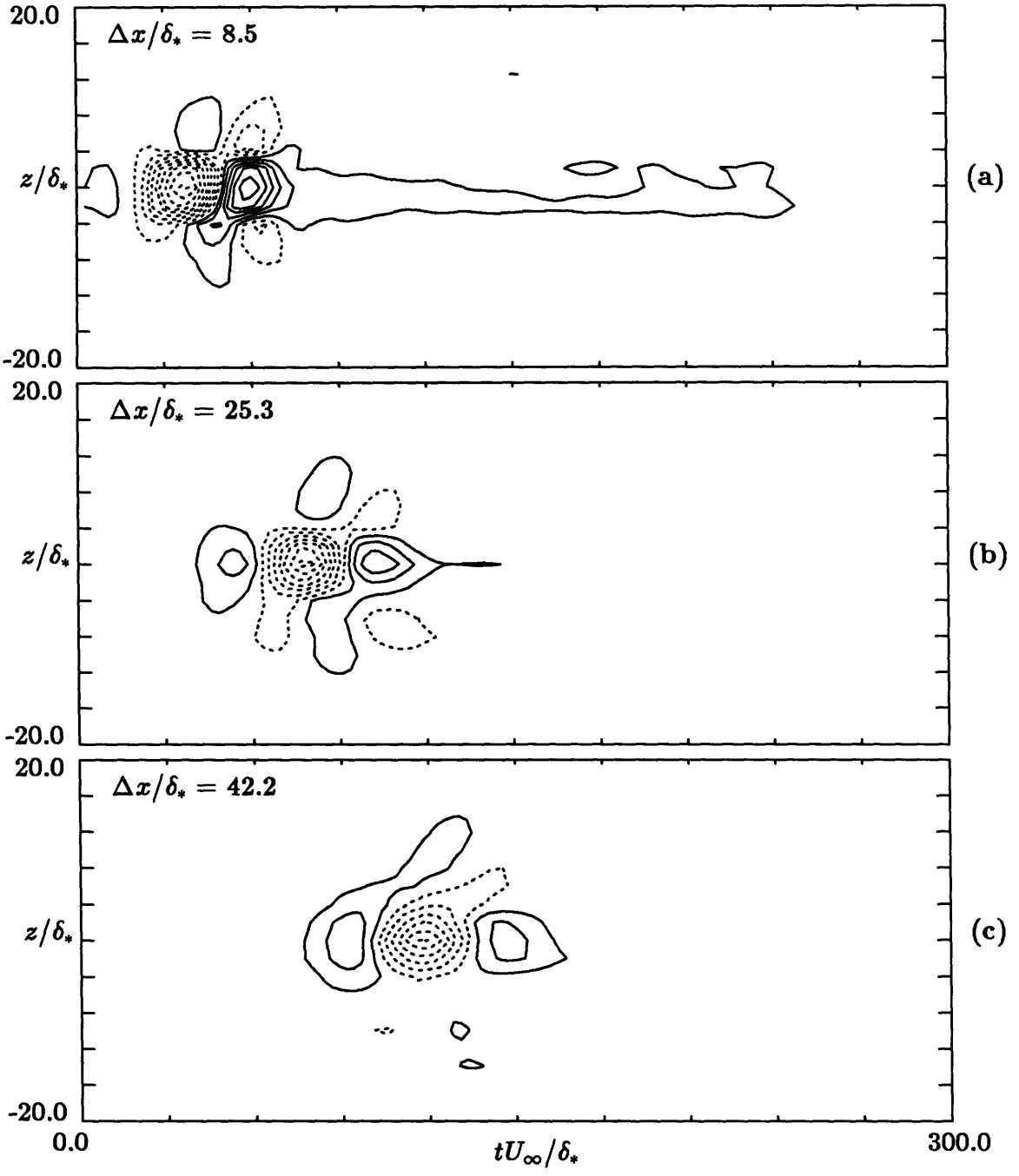

Figure 3.3: Experimental data. Contours of streamwise velocity at $y/\delta_* = 0.5$. Contour levels: $0.0005U_\infty$. Solid lines represent positive contours, dotted lines represent negative contours.

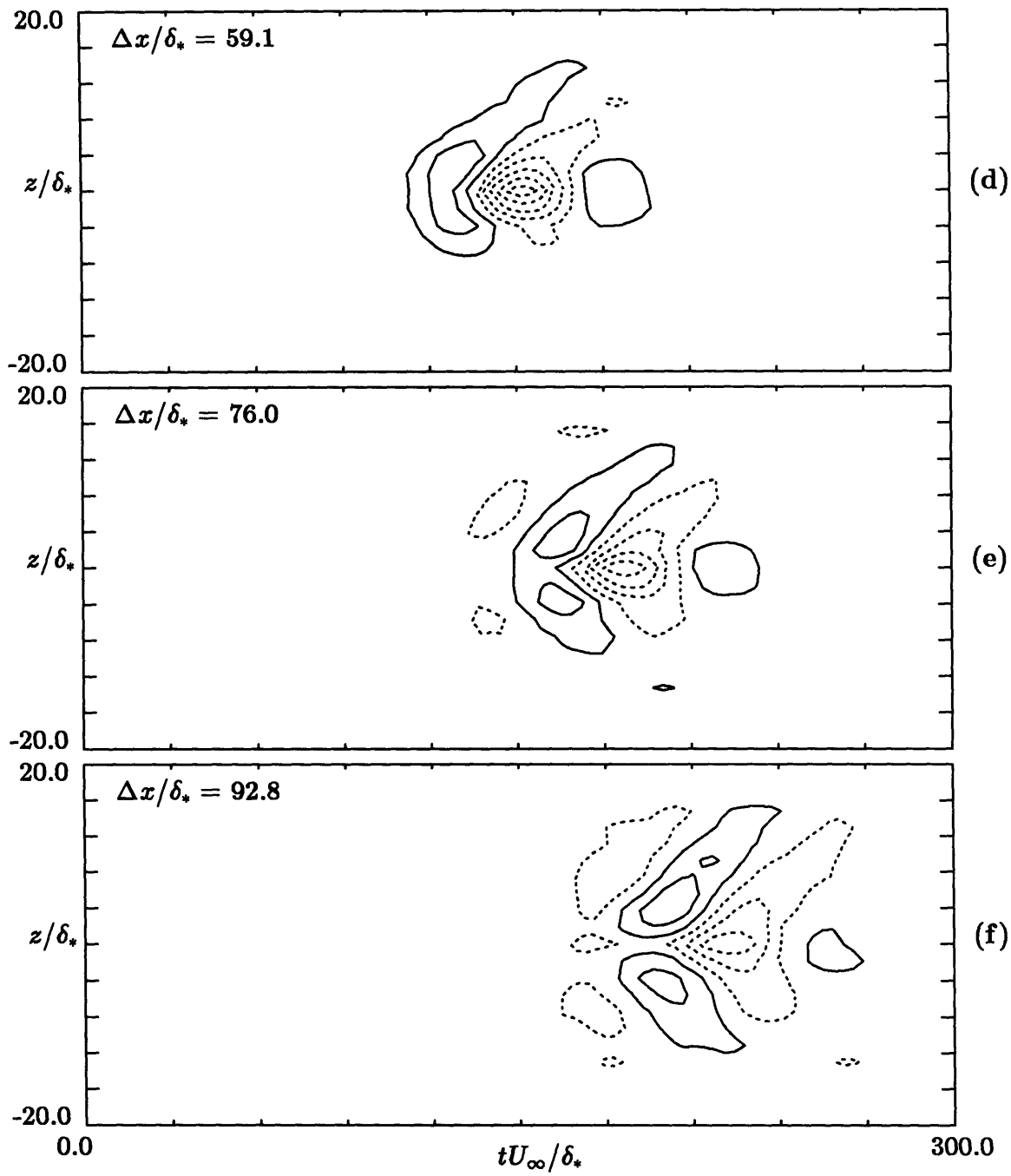

Figure 3.3: (Continued). Experimental data. Contours of streamwise velocity at $y/\delta_* = 0.5$. Contour levels: $0.0005U_\infty$. Solid lines represent positive contours, dotted lines represent negative contours.

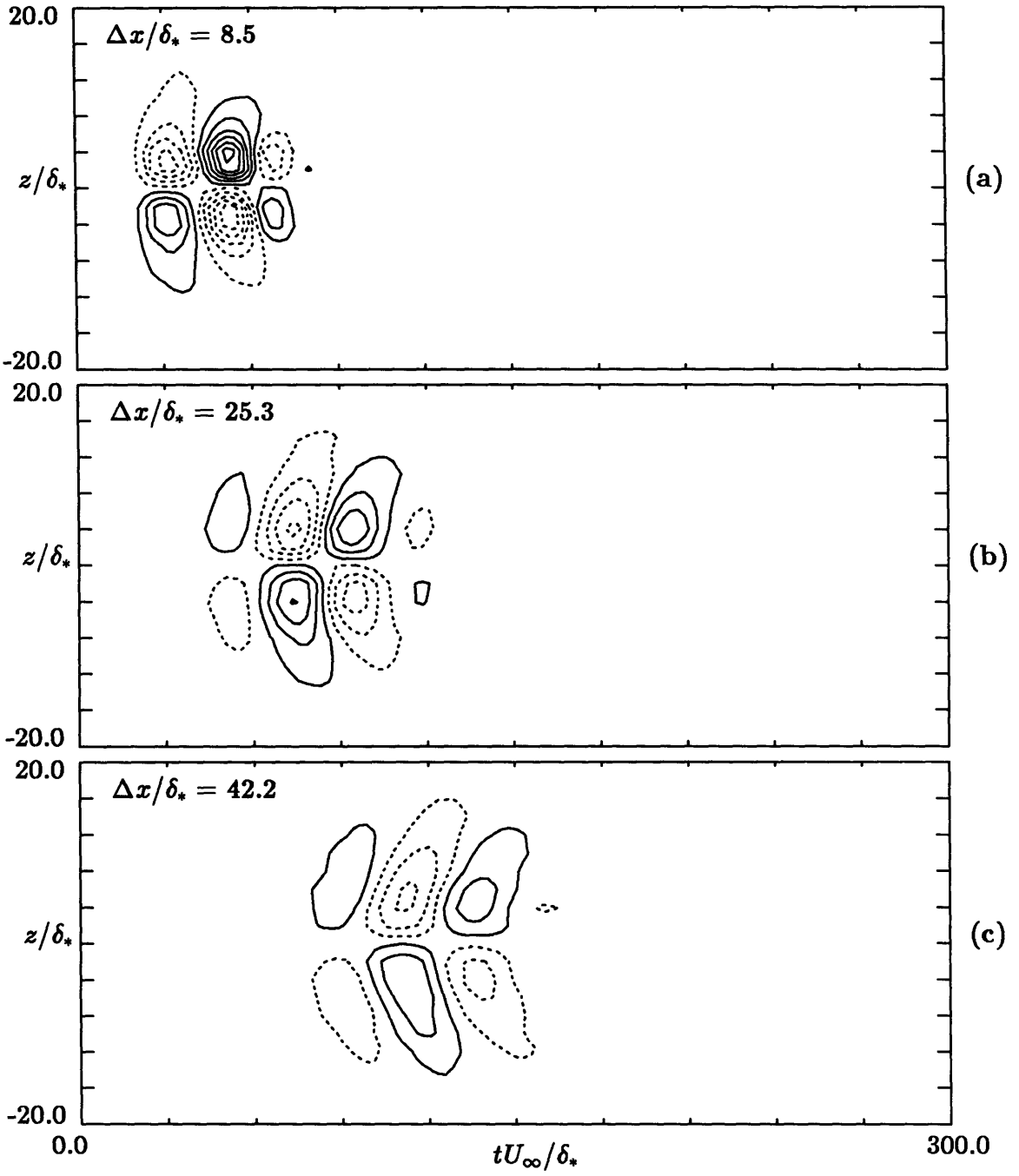

Figure 3.4: Experimental data. Contours of spanwise velocity at $y/\delta_* = 0.5$. Contour levels: $0.0005U_\infty$. Solid lines represent positive contours, dotted lines represent negative contours.

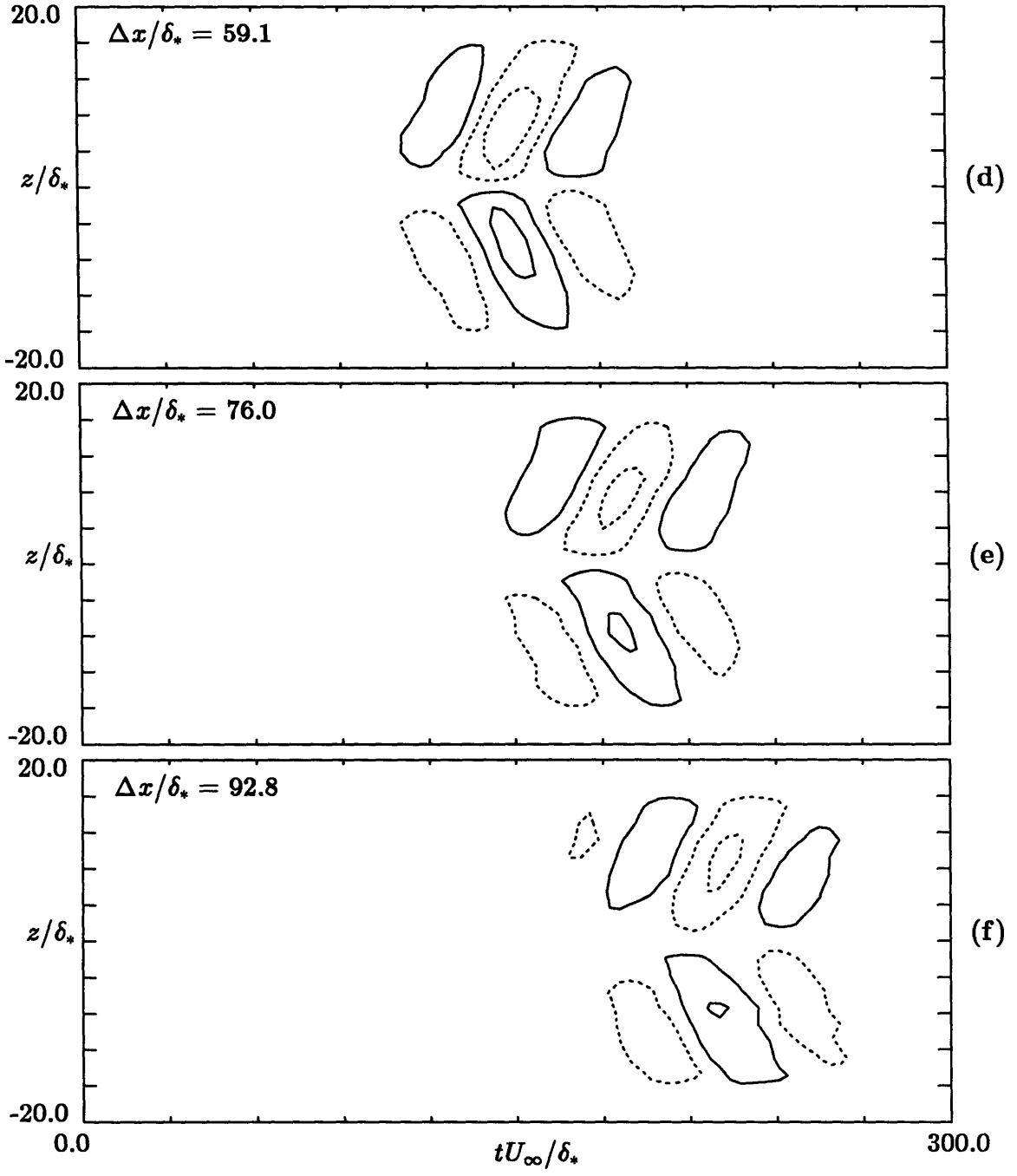

Figure 3.4: (Continued). Experimental data. Contours of spanwise velocity at $y/\delta_* = 0.5$. Contour levels: $0.0005U_\infty$. Solid lines represent positive contours, dotted lines represent negative contours.

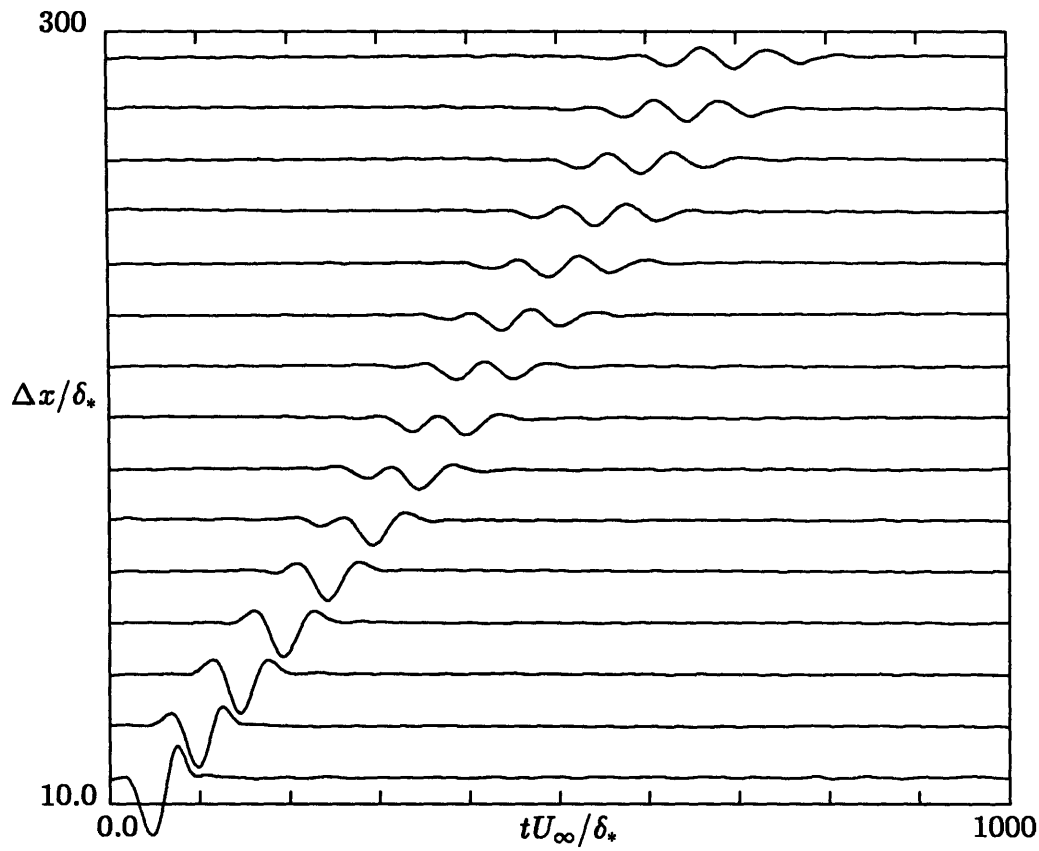

Figure 3.5: Experimental data. Evolution of streamwise velocity at $z = 0$ and $y/\delta_* = 0.5$ showing transition from transient to wave regimes.

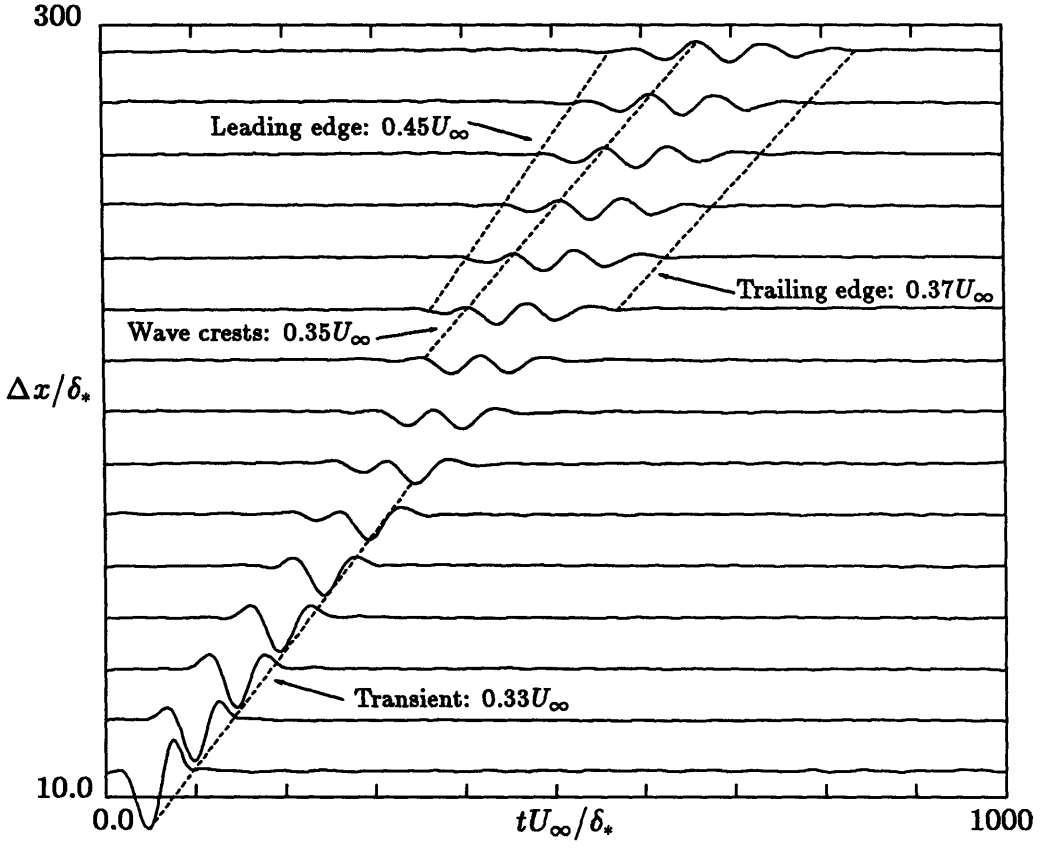

Figure 3.6: Experimental data. Propagation speeds of the weak disturbance at different phases of its evolution. Transient propagation speed, wave propagation speed and leading and trailing edge propagation speeds.

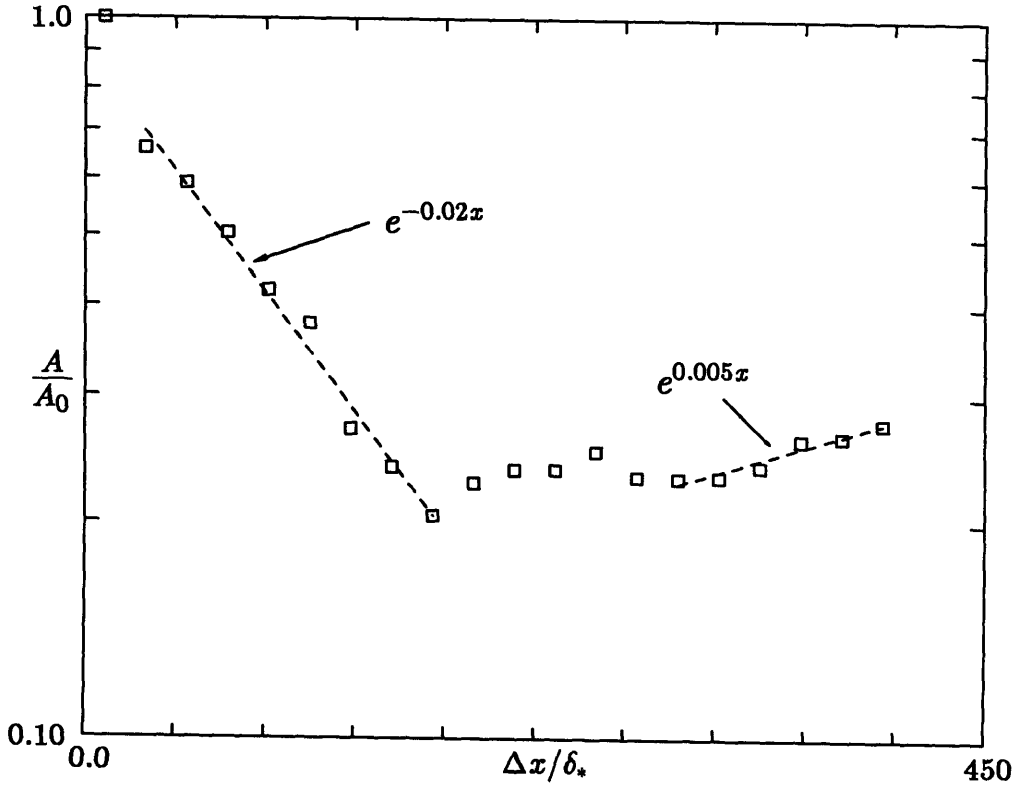

Figure 3.7: Experimental data. Evolution of peak-to-peak amplitude of the streamwise disturbance velocity at $z = 0$ and $y/\delta_* = 0.5$. Exponential decay of initial transient structure and slow exponential growth of wave packet.

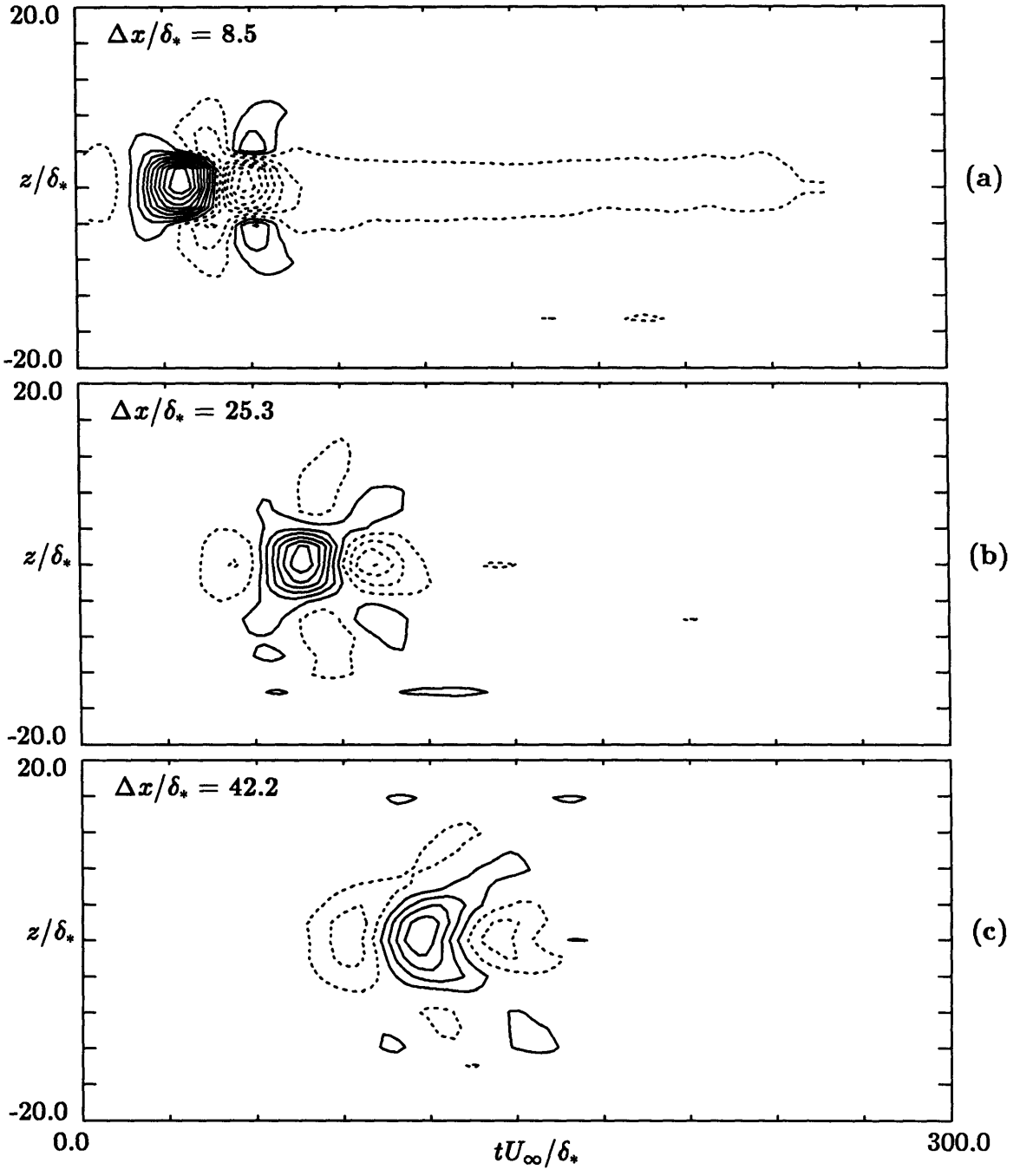

Figure 3.8: Experimental data. Contours of streamwise velocity at $y/\delta_* = 0.5$. *Negative* disturbance. Contour levels: $0.0005U_\infty$. Solid lines represent positive contours, dotted lines represent negative contours.

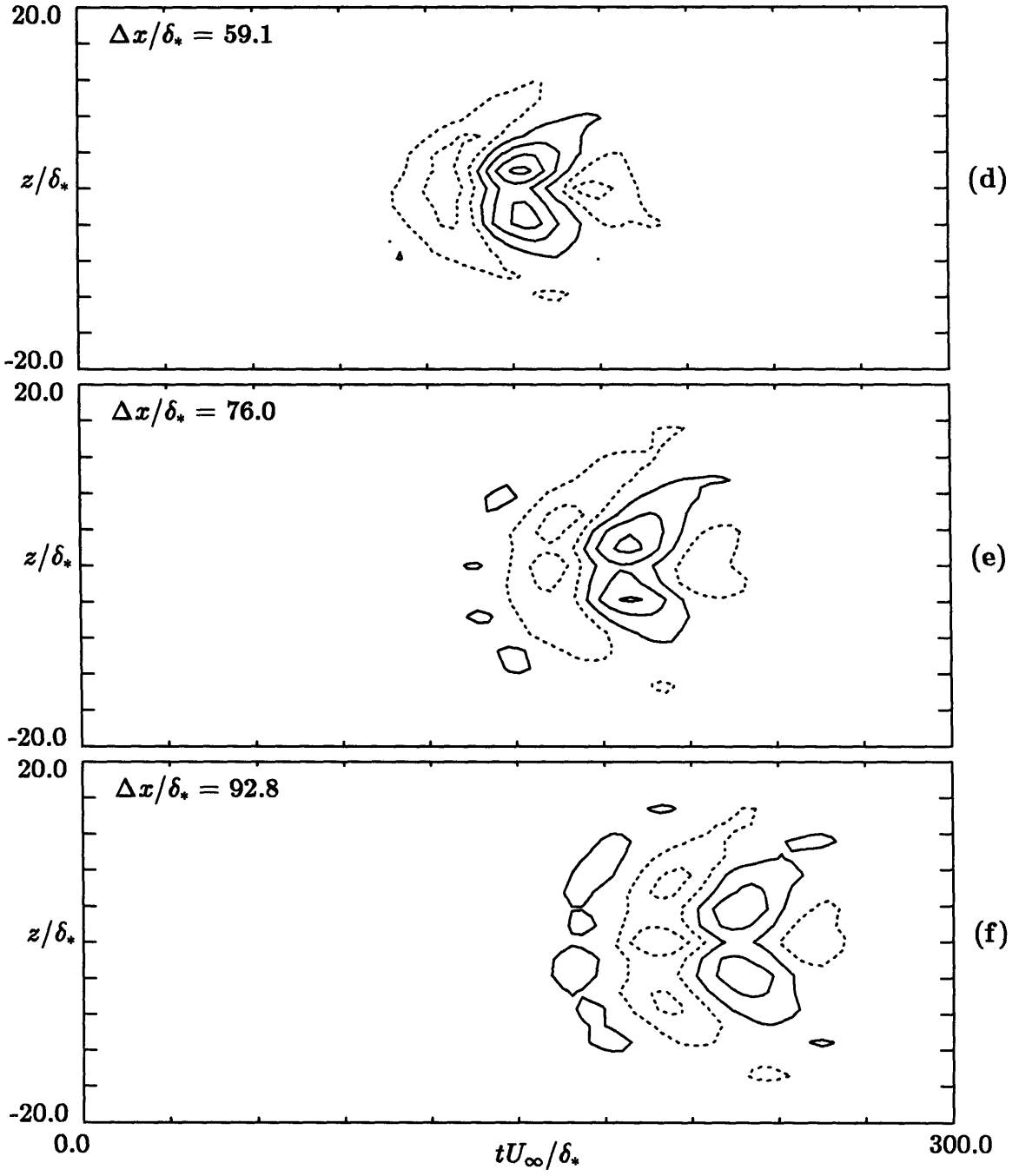

Figure 3.8: (Continued). Experimental data. Contours of streamwise velocity at $y/\delta_* = 0.5$. ***Negative*** disturbance. Contour levels: $0.0005U_\infty$. Solid lines represent positive contours, dotted lines represent negative contours.

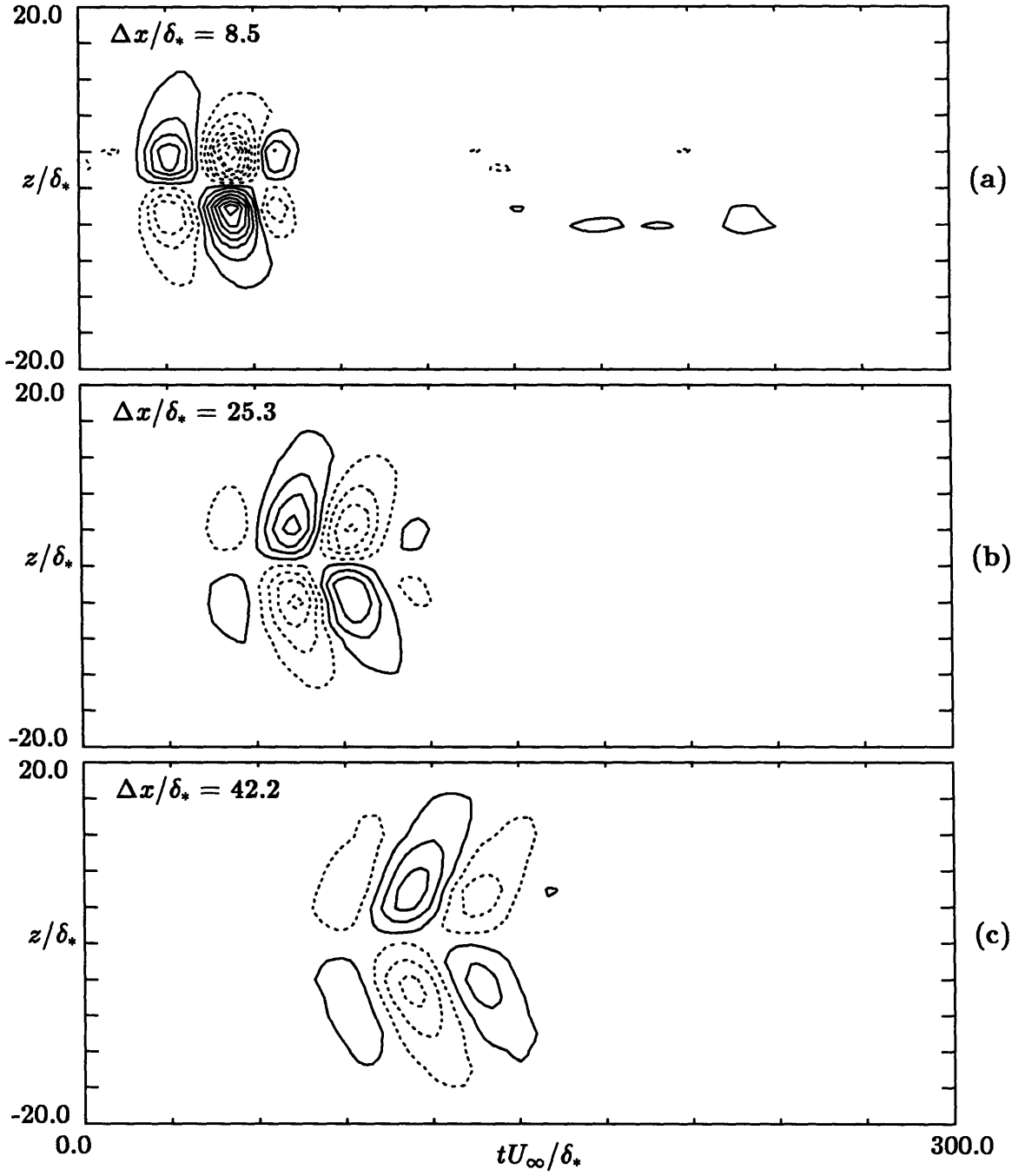

Figure 3.9: Experimental data. Contours of spanwise velocity at $y/\delta_* = 0.5$. *Negative* disturbance. Contour levels: $0.0005U_\infty$. Solid lines represent positive contours, dotted lines represent negative contours.

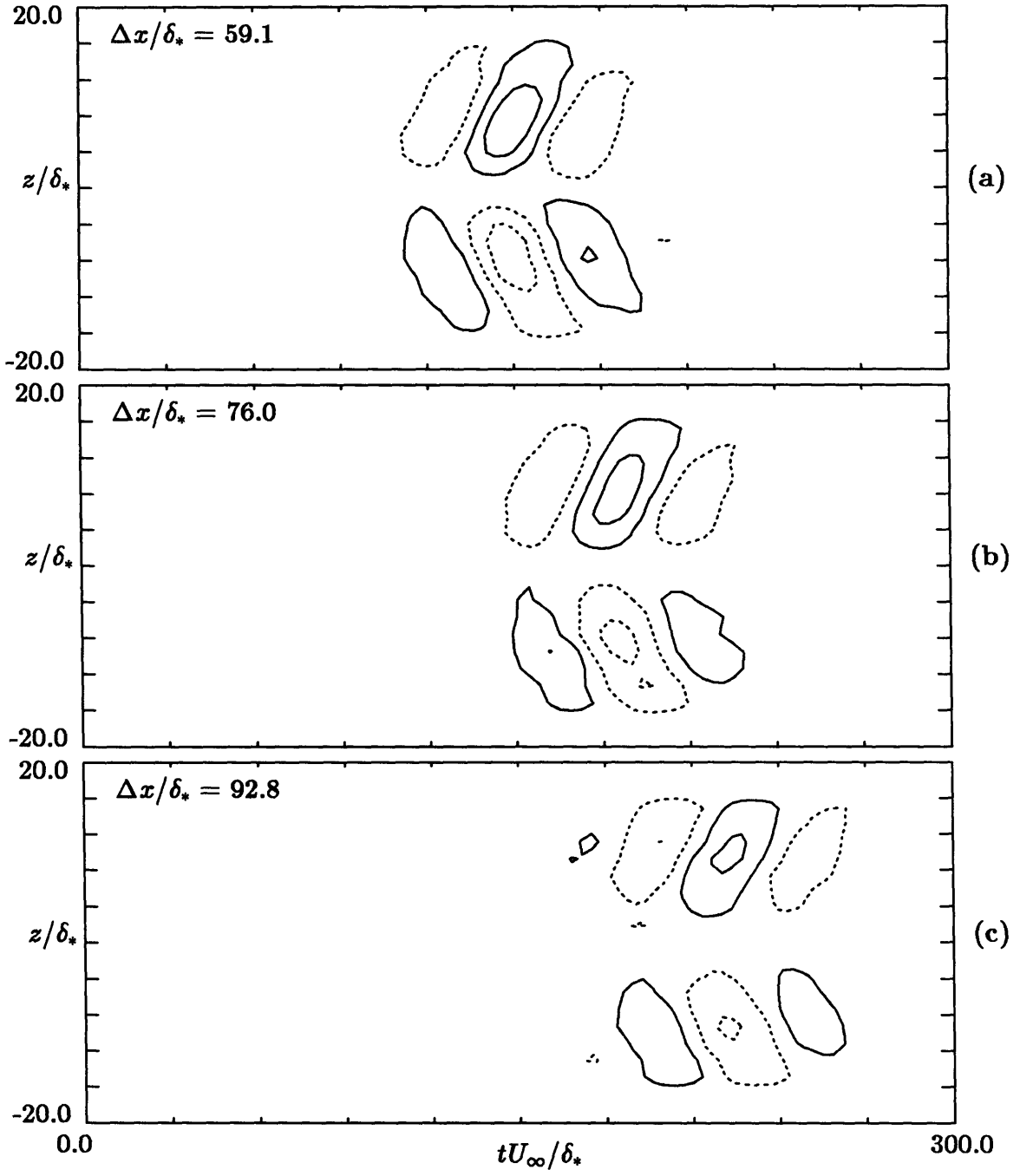

Figure 3.9: (Continued). Experimental data. Contours of spanwise velocity at $y/\delta_* = 0.5$. ***Negative*** disturbance. Contour levels: $0.0005U_\infty$. Solid lines represent positive contours, dotted lines represent negative contours.

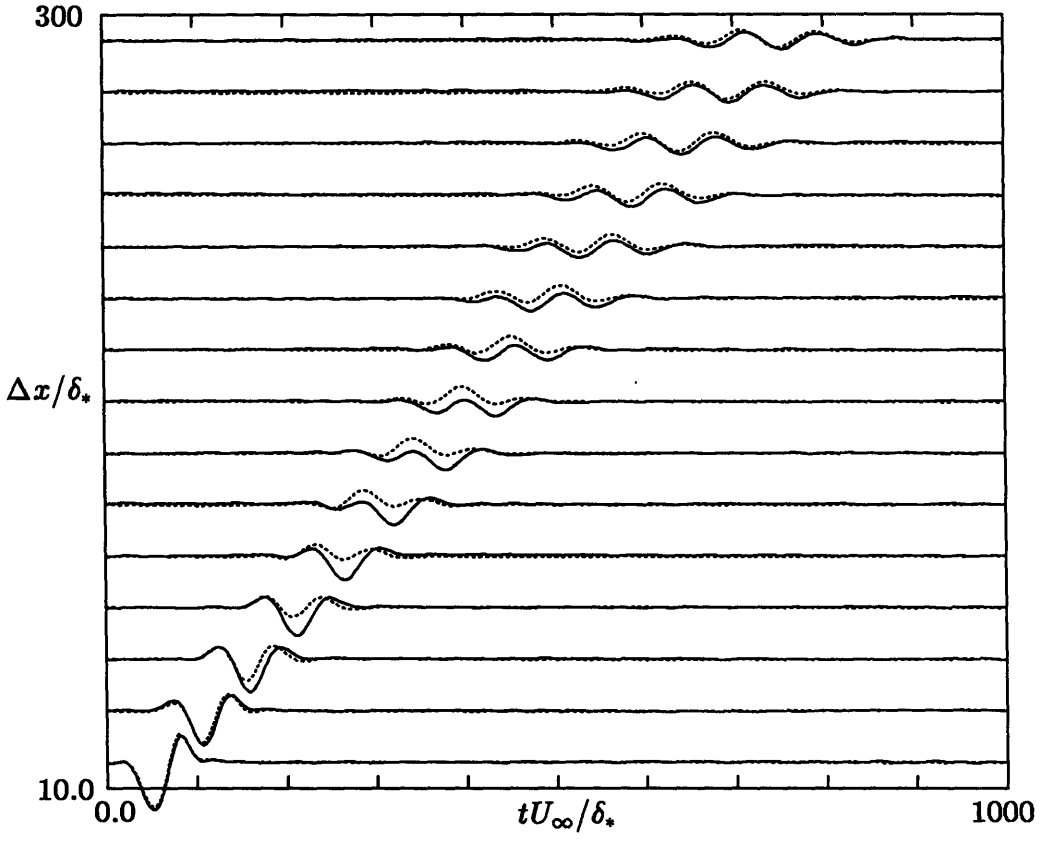

Figure 3.10: Experimental data. Evolution of two disturbances at $z = 0$ and $y/\delta_* = 0.5$. Solid line represents 'positive' disturbance created by up-down membrane motion. Dotted line represents the 'negative' disturbance, *inverted* for plotting purposes.

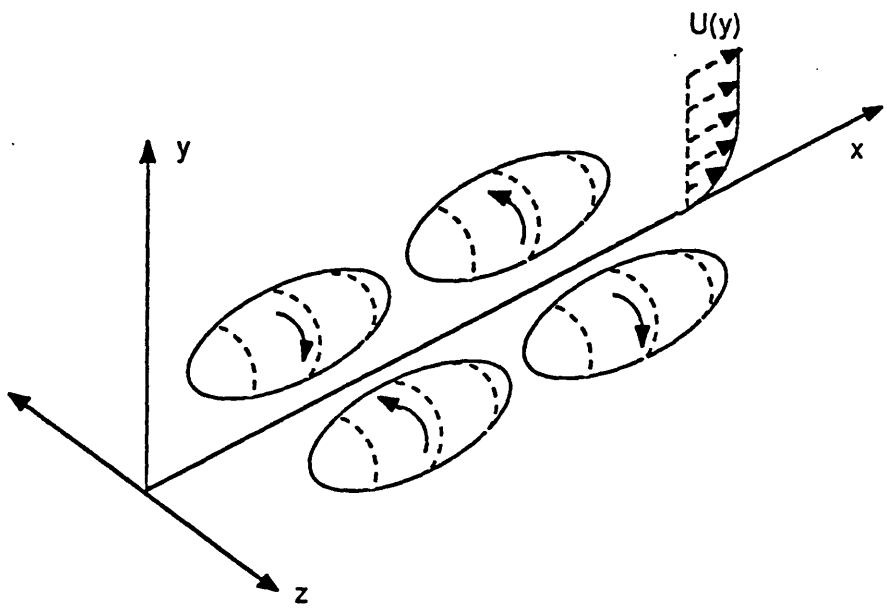

Figure 3.11: Schematic of initial conditions used in numerical studies to simulate membrane motion. Perturbation represents two pairs of counter-rotating streamwise vortices

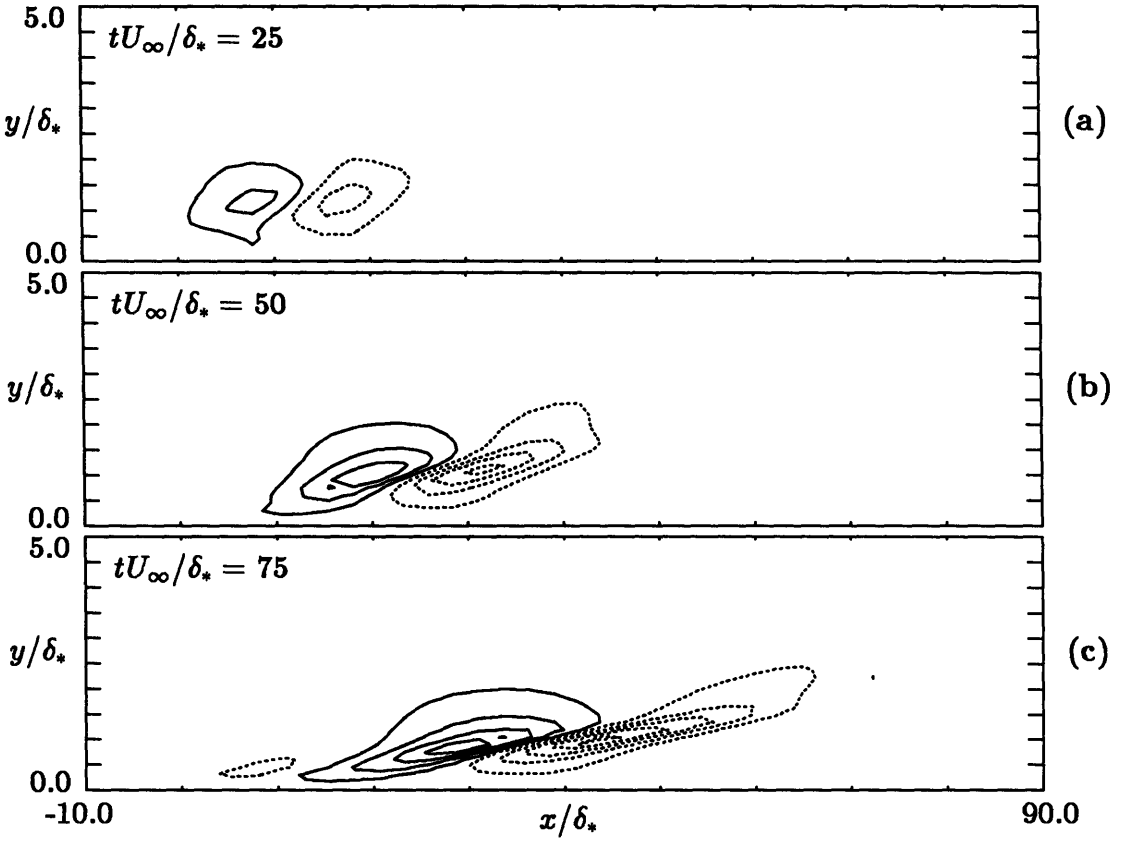

Figure 3.12: Linear initial value problem. Contours of streamwise perturbation velocity at $z = 0.0$. Solid lines represent positive contours, dotted lines represent negative contours.

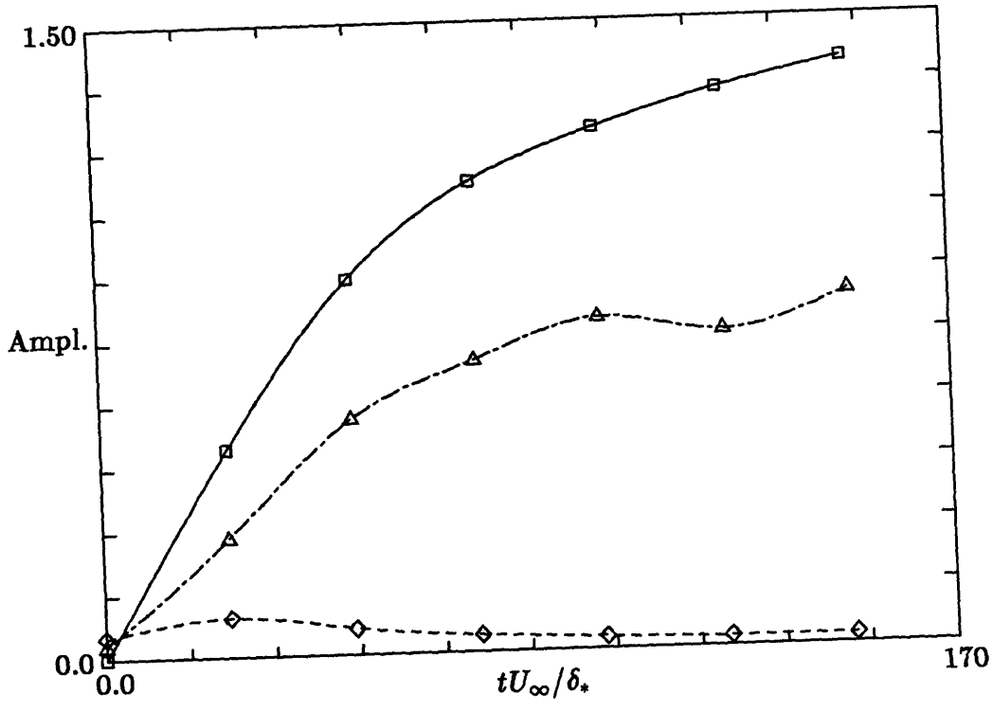

Figure 3.13: Linear initial value problem. Amplitude of u, v and w components as functions of time.

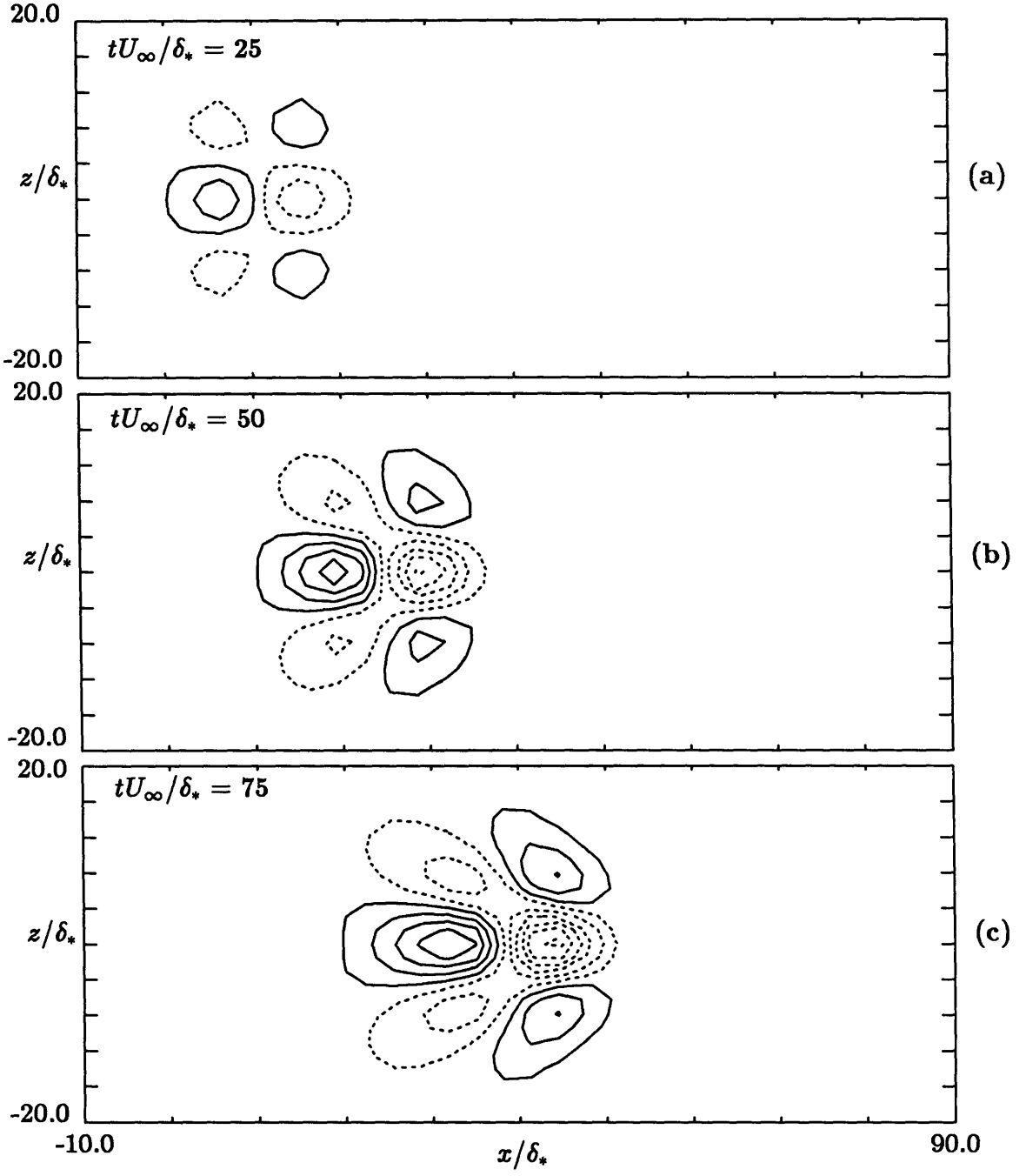

Figure 3.14: Linear initial value problem. Contours of streamwise perturbation velocity at $y/\delta_* = 1$. Solid lines represent positive contours, dotted lines represent negative contours.

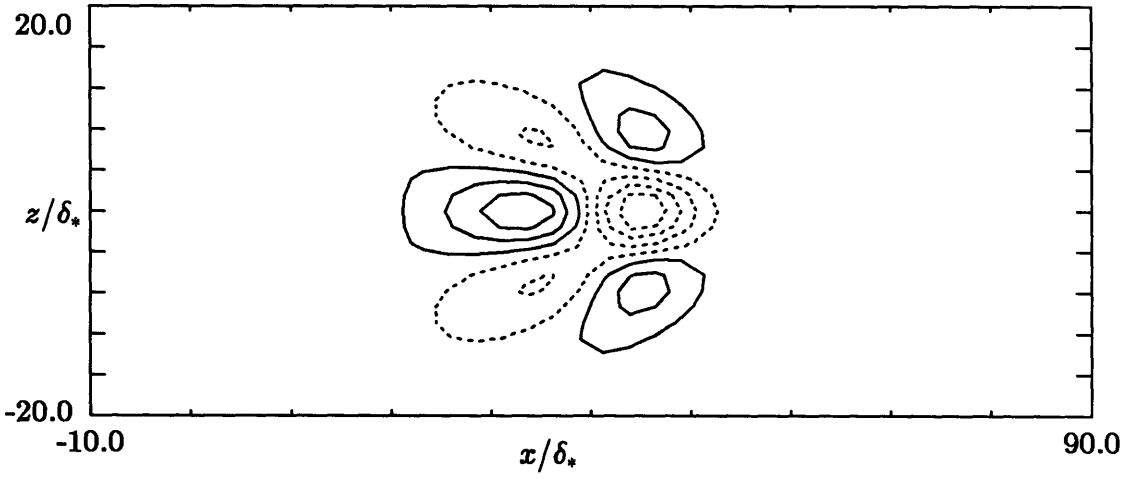

Figure 3.15: Linear initial value problem. Contribution to flow field at $t = 75$ from normal vorticity part of solution (w_1). $y/\delta_* = 1$

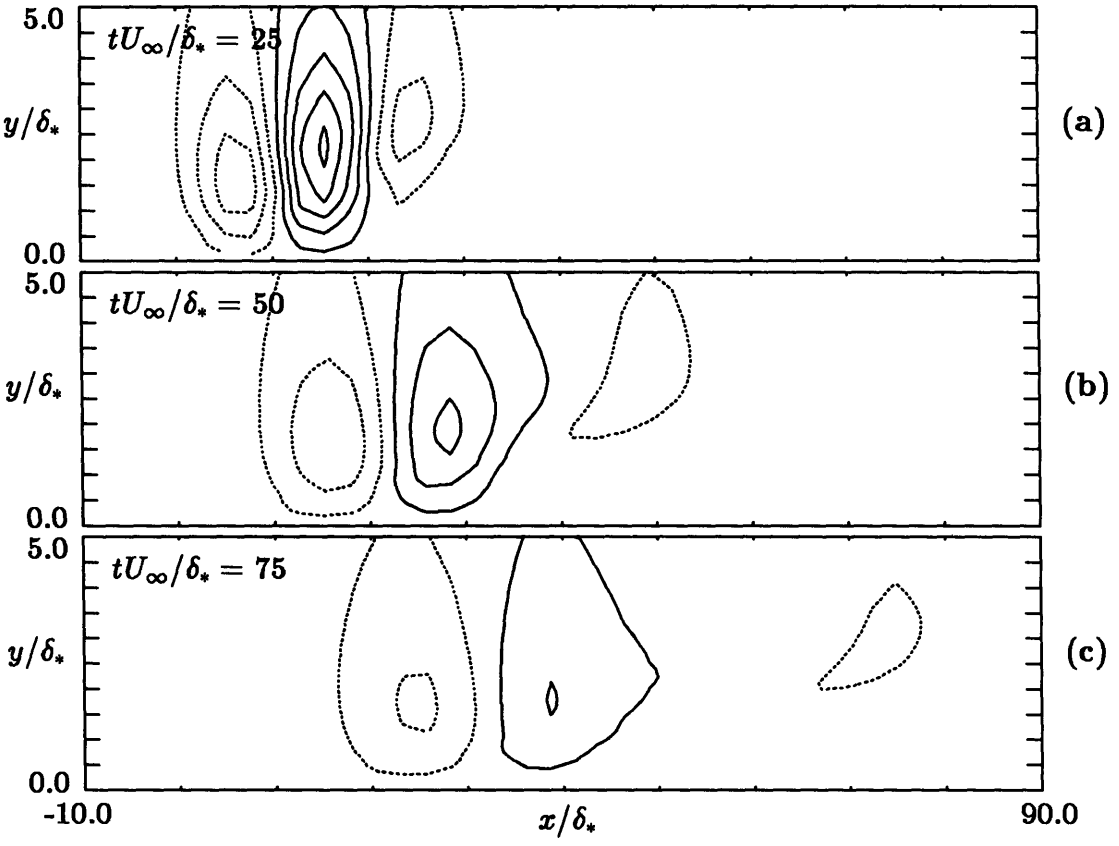

Figure 3.16: Linear initial value problem. Contours of normal velocity at $z = 0.0$. Solid lines represent positive contours, dotted lines represent negative contours.

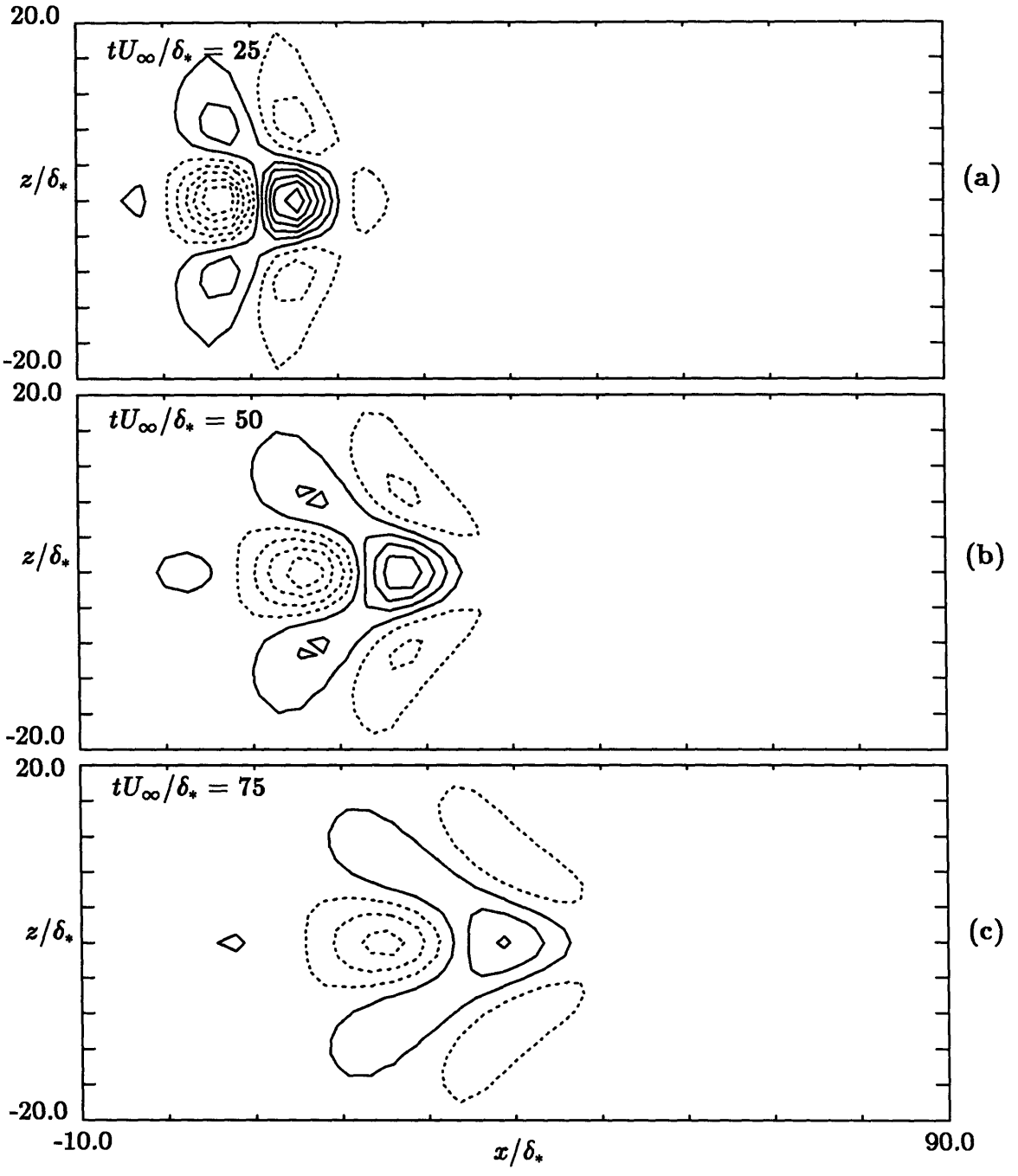

Figure 3.17: Linear initial value problem. Contours of normal velocity at $y/\delta_* = 1$. Solid lines represent positive contours, dotted lines represent negative contours.

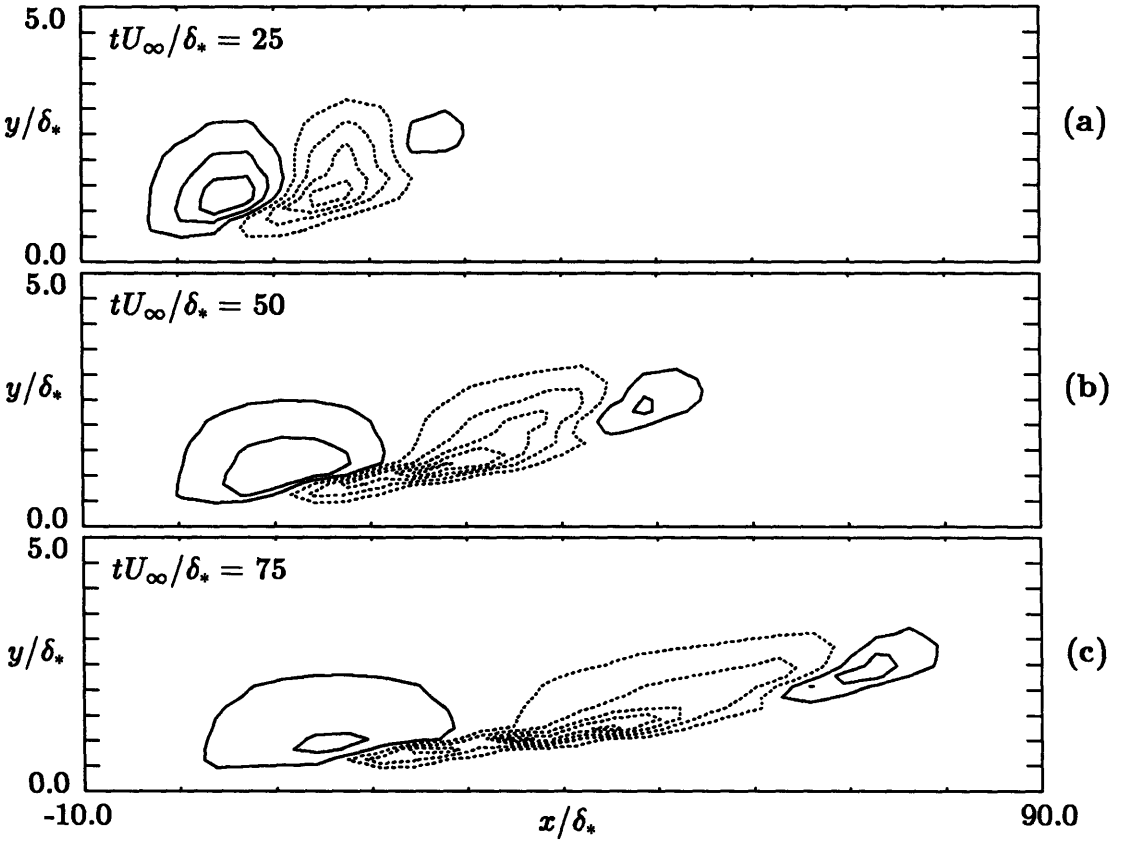

Figure 3.18: Flat-Eddy calculation. Contours of streamwise perturbation velocity at $z = 0.0$. Contour levels: $0.002U_\infty$. Solid lines represent positive contours, dotted lines represent negative contours.

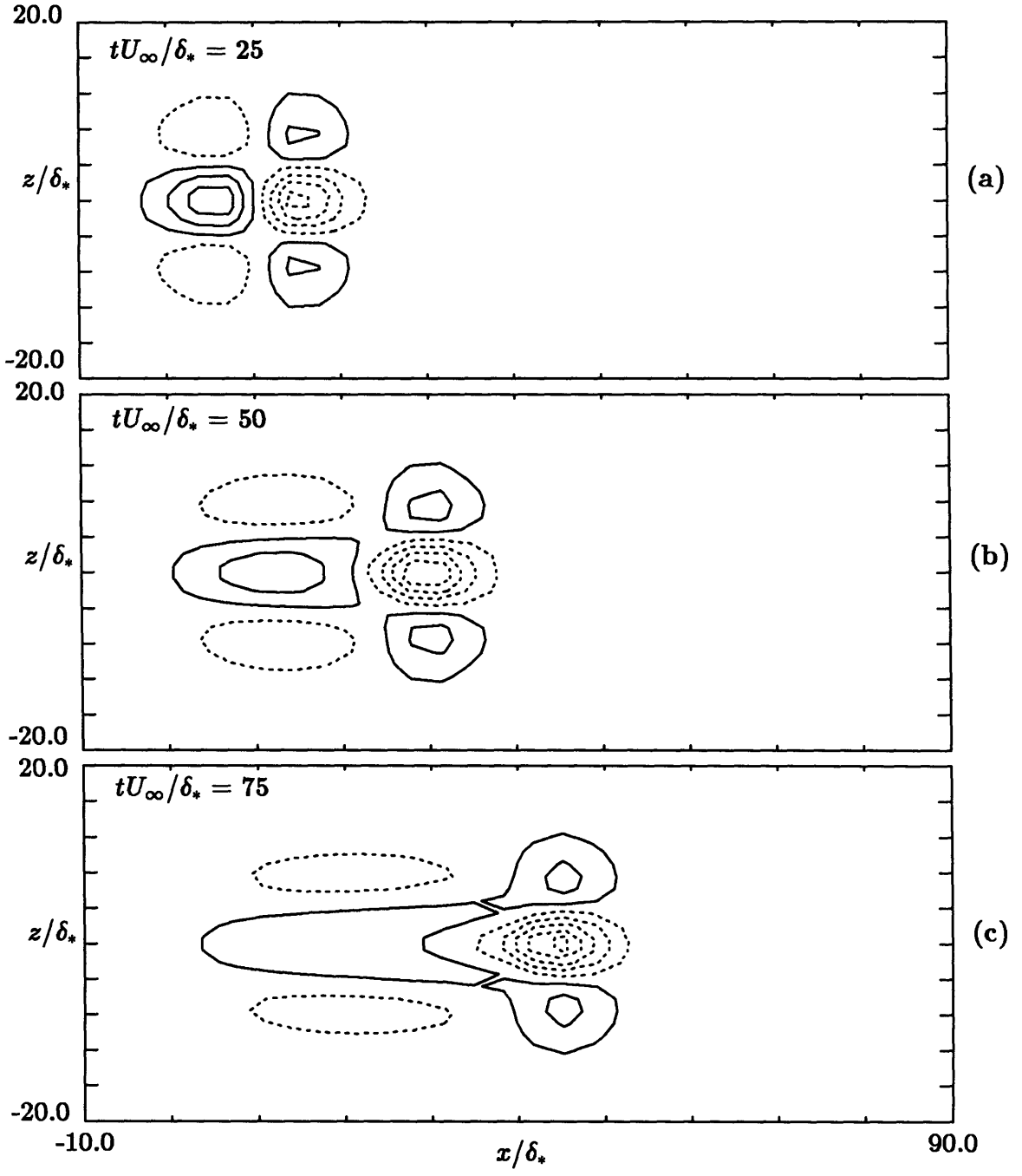

Figure 3.19: Flat-Eddy calculation. Contours of streamwise perturbation velocity at $y/\delta_* = 1$. Contour levels: $0.002U_\infty$. Solid lines represent positive contours, dotted lines represent negative contours.

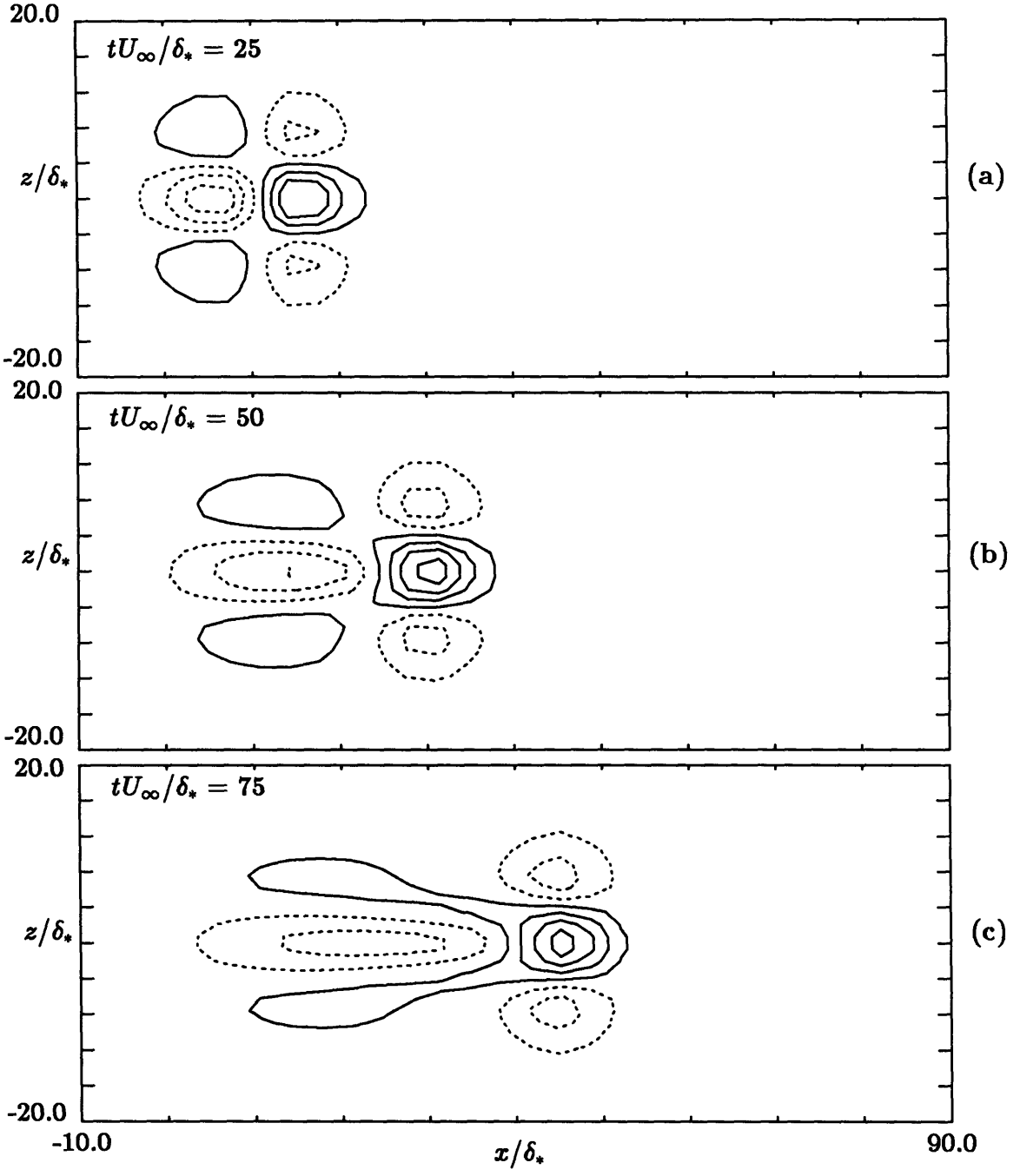

Figure 3.20: Flat-Eddy calculation. Contours of streamwise perturbation velocity at $y/\delta_* = 1$. *Negative* disturbance. Contour levels: $0.002U_\infty$. Solid lines represent positive contours, dotted lines represent negative contours.

Chapter 4

Strong Disturbances

This chapter discusses the evolution of disturbances in which the transient modes do not decay, as was seen in the previous chapter. As we shall demonstrate, two processes govern the growth of the strong initial disturbance. The first is growth driven by nonlinear processes, which are now strong enough to overcome viscous effects and drive the disturbance to amplify as it advects, generating an increasingly sharp spanwise structure. The second mechanism is a secondary instability that develops on the distorted mean profile. The transient disturbance is strong enough such that the internal shear layer formed distorts the mean profile with enough amplitude, and for enough time to allow a secondary instability to grow on the inflectional profile. As we shall see, the growth rates for the secondary instability are significantly higher that the Tollmien-Schlichting wave growth rates for the Blasius boundary layer.

The majority of the results presented here will be from a full Navier-Stokes simulation of the initial-value problem. These results are uniquely valuable in that the pressure and all three components of velocity are available throughout the entire flow field. In addition to these results, we shall present some additional calculations from the flat-eddy model[63], and also some accompanying experimental results.

4.1 Numerical Simulation

The initial-value problem was solved numerically using a full Navier-Stokes boundary layer code developed by Spalart[68] at NASA Ames Research Center. We shall briefly outline the numerical method on which it is based, but the reader is referred to Spalart's papers[68,69] for the details of the technique.

4.1.1 Numerical Scheme

The boundary layer code is designed to solve the three-dimensional, incompressible time-dependant Navier-Stokes equations for the flow over a flat plate. The boundary conditions in the horizontal plane are periodic, and a Fourier decomposition is used in the $x-z$ plane. For the initial-value problem, this means that we are actually computing the evolution of an infinite array of disturbances, each evolving simultaneously. In order to enforce periodicity in the x-direction, the downstream growth of the boundary layer must be accounted for. This is achieved by writing the equations in a similarity form so that the boundary layer height remains fixed in the new coordinate system. Once this has been accomplished, the spatial growth of the boundary layer is simulated by a temporal growth introduced into the equations of motion. This effectively transforms the computational box into a moving frame of reference so that, as the disturbance propagates downstream, the computational box follows with it, and the boundary layer thickens accordingly.

The discretization in the vertical direction is accomplished with Jacobi polynomials which give good resolution near the wall and decreasing resolution in the free stream. They do have the disadvantage that there does not exist a fast Jacobi transform, sim-

ilar to the fast Fourier transform or the fast Chebychev transform, and so the vertical decomposition requires $O(N^2)$ operations rather than $O(N \log N)$ operations possible using FFT routines. This means that for a large number of vertical modes, the calculation slows significantly. For the present problem, the number of vertical modes needed to achieve the desired accuracy was only 35 and so the inversion of the Jacobi polynomials was not computationally expensive. The code is written in VECTORAL, a programming language developed at NASA Ames Research Center which implements vectorized calculations very efficiently on the NASA Ames Cray X-MP computer. The results presented here were run using a $128 \times 128 \times 35$ grid, (in the x, z and y directions respectively) and the computational box was $100\delta_* \times 50\delta_*$ in the x and z directions. (The entire semi-infinite half plane: $y = 0$ to ∞ is calculated by an exponential mapping into a finite domain). Each time-step took about 15 seconds of CPU time, and about 50 time-steps were needed to advance the solution 100 non-dimensional time units, tU_∞/δ_*.

For the present results, the initial conditions were placed at $x = 0, z = 0$ at time $t = 0$ and the flow field was integrated forward in time. The initial conditions used were the pair of counter-rotating eddies that were considered in the previous chapter. For the current calculations, the value for the amplitude factor used in the initial conditions was $A = 0.2$. This value corresponded to an initial peak-to-peak v perturbation of 1% of U_∞.

4.1.2 Velocity Contours

Horizontal Velocities

The series of plots shown in Figure 4.1a-f show the centerline perturbation velocity field in the $x-y$ plane at several non-dimensional times. The picture in the first few frames is by now very familiar. The lift-up effect creates two adjoining regions of fluid, a low-speed region and a high-speed region further upstream. The action of the mean shear tilts the structure over and stretches it and an internal shear layer is formed in the flow. Note that the perturbation levels here are quite high: the peak-to-peak perturbation at $t = 43$ is of the order of 5% of U_∞ and as the disturbance travels downstream, the amplitude of u grows at a slow rate until it begins to rise sharply at $t = 117$. At later times, there are some new features that were not seen in the low-amplitude results. At $t = 99$, a 'necking' of the structure begins to appear at $x = 45$. This necking intensifies, and by $t = 136$ the structure seems to have broken into two parts. As we shall see, this is in fact a wave which is growing on the back of the shear layer and causing the structure to break down eventually. The contours are not very descriptive in this regard, but the nature of the secondary disturbance will be clearer in the following discussion.

The spanwise structure of the disturbance is shown in Figure 4.2a-f. Again, several similarities with the low-amplitude results can be seen. The initial pattern of the u component is the same as in the linear results, and as time increases, the surrounding wave packet develops and grows as we saw in the weak disturbance. The necking seen in Figure 4.1 is reflected along the centerline of the contour plots at times $t = 117$ and $t = 136$. The most prominent feature that is new to the high-amplitude disturbance is the development of the strong spanwise shear layers and the long, thin regions of

high-speed fluid that straddle the central low-speed core of the disturbance as shown in Figure 4.2. This was hinted at in the linear calculations, although the intensity of the 'strips' and their spanwise inclination to the streamwise direction is a new aspect of the disturbance structure. The wave packet seen in the linear calculations accompanying the transient structure is also present in the full simulations, but by $t = 99$, it no longer contributes significantly to the structure of the disturbance. From that time, the waves are only a low-amplitude addition to the main part of the disturbance which has derived from the transient.

The 'streakiness' in the streamwise velocity is very suggestive of what is seen in turbulent flows, and this aspect of the flow will be discussed in detail in Chapter 5. Swearingen & Blackwelder[71] also noted that for a flow in which there are streamwise Görtler vortices, strong spanwise gradients, $\partial U/\partial z$, develop which are comparable in amplitude to the shear, $\partial U/\partial y$, in the normal direction. They suggested that the secondary instability was associated more with the spanwise gradients than with the normal gradients. The maximum perturbation velocity gradient in the x, y and z directions at each time are tabulated in Table 4.1. These values are normalized by the vertical velocity gradient at the wall. Note that the vertical shear does not include the shear from the mean (Blasius) profile. Even without this, the shear in the normal direction is considerably greater that the horizontal (spanwise) gradients, and close to the wall, this dominance will be more pronounced. However, the spanwise shear does become significant at later times, and the possibility of an instability deriving from the cross-stream gradient cannot be discounted, although it was not observed during the time span computed for this particular disturbance.

The spanwise velocities do not evolve in the same way as the u component as Fig-

Time	$\left(\frac{\partial u}{\partial x}\right)_{min}$	$\left(\frac{\partial u}{\partial y}\right)_{min}$	$\left(\frac{\partial u}{\partial z}\right)_{min}$	$\left(\frac{\partial u}{\partial x}\right)_{max}$	$\left(\frac{\partial u}{\partial y}\right)_{max}$	$\left(\frac{\partial u}{\partial z}\right)_{max}$
43	-0.034	-0.167	-0.034	0.017	0.192	0.042
62	-0.035	-0.242	-0.046	0.018	0.245	0.063
80	-0.035	-0.282	-0.058	0.018	0.273	0.094
99	-0.034	-0.293	-0.074	0.028	0.274	0.139
117	-0.040	-0.335	-0.100	0.041	0.399	0.193
136	-0.050	-0.439	-0.144	0.056	0.549	0.245

Table 4.1: Maximum velocity gradients in x, y and z directions. Velocity gradients are non-dimensionalized by the mean shear at the wall: $(\partial U/\partial y)_{y=0}$.

ure 4.3a-f shows. The initial conditions have a four-fold symmetry, and the original structure remains intact with additional lobes and waves adding onto the disturbance as time progresses. It is interesting to note that the highly oblique strips that so markedly characterized the streamwise velocity contours are not visible here, and the w component seems to be insensitive to the high spanwise gradients that the streamwise flow develops. We shall see that this was also true for the pressure.

Vertical Velocity

The centerline structure of the vertical velocity field is shown in Figure 4.4 and the distinction between the wave modes and the advective modes is made clear once again when we compare the v field with the u field. The normal component shows none of the structure of the streamwise component and the internal shear layer that the lift-up has created. Whereas the u perturbations are confined to the boundary layer $(y/\delta_* < 3)$, the normal velocity extends well into the free stream before decaying. This difference makes sense when one recalls the linear equations for the horizontal velocities

(Equation 3.22 and 3.23) which show that the w_1 component (which we demonstrated to be the dominant component) only exists in the presence of a mean shear. In contrast to this, the vertical component (governed in the linear case by the Orr-Sommerfeld equation or the Rayleigh equation, Eqn. 3.17) does not directly involve the mean shear, and decays in the free stream according to e^{-ky}, thus extending well beyond the edge of the boundary layer.

As time increases, the structure of the v field increases in complication and we see waves beginning to develop in the downstream side of the structure. These waves grow in the successive time frames, eventually filling the entire structure. In the linear problem, the v component decays, and this is partially reproduced in the upstream side of the disturbance. The negative perturbation, corresponding to an accelerated (and therefore stabilized) mean flow, does not develop any wave structure and simply propagates downstream, unchanged (and unstretched), slowly decaying in amplitude as time progresses.

The wave development is not very clearly depicted by the contour plots. So as to get a better look at the secondary wave, the actual u- and v-velocity trace is shown in Figure 4.6. Here $u(x)$ is shown by a solid line and $v(x)$ by a dotted line at different times at a height of $y/\delta_* = 1.05$, which cuts through the center of the wave field. v is plotted with a magnification of ten so that its plotted amplitude is comparable with that of the u signal.

The u component at $t = 43$ looks very similar to the experimental data from the weak disturbance in the previous chapter (Figure 3.5) reflecting the lift-up of fluid by the initial velocity field. Similarly, the v signal corresponds exactly to the initial perturbations that were prescribed in the counter-rotating eddies. However, as time

Time tU_∞/δ_*	Wavenumber $\alpha\delta_*$	Phase Speed c_r/U_∞
62	1.01	-
80	0.83	0.42
99	0.61	0.38
117	0.50	0.42

Table 4.2: Characteristics of secondary waves: Wavenumber and Phase Speed

progresses, a wave packet appears, riding on the back of the shear layer. Gustavsson commented[24] that because the v component is not affected by the lift-up effect, wave phenomena should be easier to detect in the vertical velocity than in the streamwise velocity, and this is true here. The u signal does not reflect any of the wave motion until $t = 99$ at which point the wave has grown to a high amplitude and a kink in the v profile appears. In the meantime, the v signal shows the wave packet growing and propagating downstream with the rest of the shear layer structure. By taking the power spectrum of each v signal in Figure 4.6, we can find the wavenumber of the most amplified mode in the wave packet. In addition to this, we can graphically estimate the phase speed of the wave by measuring the distance traveled by a wave crest between each time frame. These quantities are summarized in Table 4.2. The phase speed remains approximately constant at $0.4U_\infty$ which coincides with the average propagation speed of the shear layer on which it rides. The wavenumber, however, continues to decrease linearly until $t = 117$ at which time the scale of the wave is so similar to that of the rest of the disturbance, that the concept of wave perturbing a distorted mean flow no longer makes sense.

The spanwise structure of the v component (Figure 4.5) does not yield anything new. The strong oblique strips, seen in the u component are also seen here as regions

of strong downward motion. This is consistent with the lift-up effect (in reverse) and here the negative v motion brings high-speed fluid down from the upper part of the boundary layer to create the accelerated regions in the u component. The secondary wave motion is clearly seen in the $t = 62$ frame, and the transition of the wave from a two-dimensional wave to an oblique packet can be followed in the next few contour plots. Note that in agreement with the u plots, the wave packet originating from the initial conditions does not contribute significantly to the structure of the disturbance.

4.1.3 Pressure Contours

One of the features of the numerical data that makes it unique is that in addition to the velocity field, it gives the pressure throughout the entire flow field. This is, of course, impossible to achieve in the laboratory where the only pressure data available are at the wall, and even then usually only at a limited number of locations. We might expect that the pressure will depend little on y in accordance with the steady state boundary layer result. This is confirmed in Figure 4.7, in which the pressure at $z = 0.0$ remains approximately constant through the boundary layer, only decaying in the free-stream as $y \rightarrow \infty$. (note that the vertical coordinate in Figure 4.7 is stretched, and so the normal gradients are in fact somewhat higher than they appear. Nevertheless, the pressure only begins to change when $y > 2$) The decay of the pressure in the free stream is also predicted by the linear inviscid theory (Eqn. 3.16) in which the pressure in the free-stream is linearly related to $\partial v/\partial y$. Since v decays as e^{-ky} in the free stream, the pressure must decay accordingly. The reason for the jaggedness in the pressure contours is not clear, but it is thought that it lies in the numerical error accrued while calculating the pressure from the velocity field. The pressure does not actually appear directly in

the equations that are numerically integrated, and so it is calculated afterwards by solving a Poisson equation. This may have some inaccuracies associated with it which cause the saw-tooth lines in the pressure contours.

According to linear theory, the pressure depends solely on the vertical velocity and the mean profile but the nonlinear effects will generally include interactions with other velocity components. However, if one compares the pressure contours at $z = 0.0$ in Figure 4.7 with the similar plot for the vertical velocity (Figure 4.4), one sees that the two signals are strongly related, and that the pressure peaks coincide with the maxima in the streamwise gradient of the v component. This is exactly the leading term in the equation for the pressure derived in the previous chapter (Equation 3.16) and suggests that the dominant term in the pressure equation is the mean shear interaction, $U'\partial v/\partial x$. This is in agreement with the results of Johansson, Her and Haritonidis[35] who investigated the relationship between wall pressure and the velocity field in a fully turbulent boundary layer. We shall discuss this at length in Chapter 5 when we examine the associations between this flow and fully turbulent wall flows.

The spanwise structure of the pressure (Figure 4.8) also reflects the dependence on the streamwise gradient of v, although the structure is somewhat more complicated. For the early times, when the gradients in the flow are not very sharp, the pressure peaks do tend to align themselves with the streamwise gradients in v. However, as the flow becomes more complex, this correspondence is not so clear. However, there does not appear to be any effect on the pressure by the sharp spanwise gradients in the flow field and we do not observe the marked spanwise strips that both the u and the v exhibited (this is also true for the w component of velocity). This is to be expected, since the linear equation for the pressure (Equation 3.16) depends only weakly on the spanwise

gradients in v.

The pressure field is also useful in evaluating the validity of the flat-eddy model. The basic assumption of the flat-eddy approximation was that the horizontal pressure gradients were negligible, and this allowed us to write the equations in a simple form. The pressure contours of Figure 4.8 indicate that while the pressure does not initially develop strong gradients, by later times, substantial gradients in both the streamwise and the spanwise directions have developed, possibly associated with the secondary instability. These will contribute significantly to the breakdown of the flat-eddy model's validity.

4.1.4 Power Spectra

We have observed two features of the high-amplitude disturbance that were not seen in the weak disturbances discussed in Chapter 3. These features, namely the development of long alternating strips of high- and low-speed fluid, and the growth of secondary instabilities on the distorted mean profile, can be clearly seen by examining the power spectra of the velocity field for the disturbance. The wavenumber spectra for the v field are shown in Figure 4.9a-f. The initial spectrum has the oval shape and exponential decay corresponding to the initial conditions, but very quickly, at $t = 62$ we see that a peak is beginning to emerge at $\alpha\delta_* = 0.3$, $\beta\delta_* = 1.3$. This wave angle corresponds to the emergence of the two oblique strips of downward-moving fluid that have appeared on either side of the centerline in Figure 4.5c, and as they intensify, the peak in the power spectrum also intensifies. As the structure grows, it is elongated (by the stretching of the mean shear and the algebraic instability) and so the peak moves towards a lower value of $\alpha\delta_*$. By $t = 117$, a second oblique structure is beginning to

emerge, again at $\alpha\delta_* = 0.2$ but at a higher spanwise wave number: $\beta\delta_* = 2.5$. On examination of Figure 4.5f, it becomes clear that the original bar has subdivided into two sub-bars, each with a sharper spanwise gradient than the first, hence the higher value for $\beta\delta_*$. Although the calculation does not continue beyond $t = 137$, the spectra at that time indicate that this process seems to be repeating itself in a cascade of some sort: each new peak in the spectrum forming a platform from which the next peak develops at a smaller spanwise scale. By reading from the power spectra at $t = 136$, we find that the values of (α, β) at each peak are approximately: $(0.0, 0.7), (0.1, 1.3), (0.2, 2.0)$ etc., suggesting that each peak is a multiple of the first spanwise peak and that the nonlinear mechanism serves to introduce higher harmonics as time progresses. The selection of the value for α and β at the original peak is not clear and it must still be determined whether there is a linear or nonlinear selection mechanism, and what parameters govern that scale selection. The emergence of the initial spanwise peak at $tU_\infty/\delta_* = 62$ from the background suggests that it is a non linear selection mechanism, but this must be examined further.

By the later times, the distinct peaks in the spectrum are beginning to merge together. We would expect that at some later point, the spectrum will eventually become continuous and the disturbance will have degenerated into a turbulent spot.

The second process that was observed - the secondary wave growth - is also seen in the power spectra. Starting at $t = 99$ a small peak appears at $\alpha\delta_* = 0.7, \beta = 0.0$. This corresponds the two dimensional wave packet that was observed growing on the back of the distorted mean profile at $z = 0.0$. As the disturbance progresses, the wave number decreases, indicating that the instability wave stretches with the structure. In addition to this, the peak of the wave packet moves off the $\beta = 0.0$ axis. This development is

very similar to the development of the low-amplitude wave packet measured by Gaster and Grant[20] in which they noted that at the last station, the maximum amplitude of the power spectra had shifted from a two-dimensional mode, to an oblique mode. This is exactly what has happened to the secondary instability in the present case, and it raises the possibility that the nonlinear mechanism responsible for both flows may be the same. By $t = 136$, a subsequent peak at $\alpha\delta_* = 0.5$, $\beta\delta_* = 2$ is also emerging at this time. This suggests that the same mechanism that generated the cascade of scales in the oblique strips might also be responsible for this multiplication of scales resulting from the secondary instability.

4.1.5 Stability Calculations for Secondary Waves

One of the key mechanisms that was observed in the evolution of the initial disturbance was the growth of a secondary instability on the profile distorted by the strong initial perturbations. This was seen first in the v signal as a two-dimensional wave packet which rapidly grew and was eventually reflected in the u component. In an attempt to confirm the nature of this instability, calculations based on a parallel-flow instability theory were performed to examine the stability characteristics of the distorted mean profile. The application of parallel flow instability theory to this problem needs some justification since the flow is neither parallel, nor spatially homogeneous. However, the instability waves, which are first seen in the velocity signals at $t = 62$, have a typical wavelength which is initially an order of magnitude smaller than the dimension of the shear layer, and so we can make the assumption of a locally homogeneous mean flow. The problem of a non-parallel flow is dealt with by arguing that the vertical velocity is very small compared with the streamwise component (the vertical perturbations are

about 0.5% of the free stream velocity), and so they can also be discounted. While this is not a very rigorous argument, the results will indicate that the assumptions are surprisingly valid.

The waves are first seen emerging in the v signal by $t = 62$, and for this reason the calculations were performed for the flow field at that time. The distorted mean profile was extracted from the numerical simulation data at a single point in the flow field where the waves were observed: $x = 33, z = 0$. The extracted profile was smoothed to remove any jaggedness and the second derivative (which is needed in the stability calculations) was calculated using second-order finite differences. This profile is plotted in Figure 4.10 along with its first and second derivatives. The main feature of the distorted profile is that the shear layer caused by the initial conditions is sufficiently strong to produce two inflection points in the interior of the flow, at $y/\delta_* = 1.0$ and $y/\delta_* = 1.5$. The lower one of these is actually a stable inflection point with a minimum in dU/dy, but the upper one is destabilising with a maximum in the shear

On the basis of the Rayleigh inflectional criterion we would expect that this profile might be inviscidly unstable, unlike the Blasius profile for the undisturbed boundary layer. The power spectra discussed earlier showed that the instability started as a two-dimensional wave before developing oblique modes. For this reason, the stability characteristics of the chosen profile were calculated by solving the Orr-Sommerfeld equation for only two-dimensional waves. Since the selected profile is at $z = 0$, there is no cross-flow because of the symmetry properties of the flow, and so there was no need to consider the cross-stream velocity component.

The Orr-Sommerfeld solver used a finite difference shooting-method and employed orthonormalization to keep the two independent solutions distinct (cf. Conte[13]). The

equation was solved for the temporal case in which the selected wave number (α) is assumed to be real and the equation is integrated, iterating until an eigenvalue: $c = c_r + ic_i$ is found. In this formulation, the wave will be unstable if $c_i > 0$.

Figure 4.11 shows the dispersion relation: $c(\alpha\delta_*)$ for a two-dimensional wave on the specified profile for $\alpha\delta_*$ ranging from 0.05 to 1.3. The solid line indicates the solution for the distorted profile, while the dotted line shows the stability characteristics of the Blasius profile for comparison. Two aspects of the figure should be pointed out. The first is that the range of linearly growing waves ($c_i > 0$) is very broad, and that one can essentially consider the profile to be unstable for almost all relevant wave numbers. For very low values of $\alpha\delta_*$, the profile is stable, but above $\alpha\delta_* = 0.1$, c_i is positive and reaches a maximum at about $\alpha\delta_* = 0.5$ before decreasing slowly as $\alpha\delta_*$ increases. The second aspect of the profile's stability is that the growth rates are very large. The maximum value of c_i is 0.09, which is an order of magnitude larger than the maximum growth rate for the Blasius profile. These growth rates are typical for shear layer instabilities (cf. Cohen and Wygnanski[11]) and this correspondence is not unexpected. The inflection point in the mean profile dominates the stability characteristics of the flow and so the growth rates will reflect more a shear layer than a traditional boundary layer. The phase speed of the waves shows a steadily growing c_r as $\alpha\delta_*$ increases in contrast to the Blasius solution which peaks at $\alpha\delta_* = 0.5$ and decreases slowly for higher values of $\alpha\delta_*$. From this curve, the group velocity of the wave train can be determined by taking the derivative of the dispersion relation: $c_g = d(\alpha c_r)/d\alpha$. This is shown in Figure 4.12 which indicates that c_g increases steadily until about $\alpha\delta_* = 0.5$, at which point it levels off at about $0.7U_\infty$.

The vertical amplitude distribution of the instability should also follow the eigen-

function of the Orr-Sommerfeld equation. This was investigated by taking the v component of velocity from the full simulation data and filtering it with a high-pass filter at $\alpha\delta_* = 0.7$ so as to remove the background flow and leave only the wave packet. The maximum amplitude of this signal was then computed at different y/δ_* through the boundary layer, yielding a vertical amplitude distribution for the instability wave. This is plotted in Figure 4.13 along with theoretical eigenfunction for the $\alpha\delta_* = 1.0$ wave based on the distorted profile of Figure 4.10. The agreement between the two is quite good, especially the decay of the signal from $y/\delta_* = 1.8$ to the free-stream. The full simulation data grows somewhat quicker than the linear theory would predict, and it peaks at a point closer to the wall, but the overall behaviour is consistent with the linear eigenfunction. The point at which the eigenfunction reaches a maximum corresponds to the location of the inflection point in the distorted profile, which we would expect in a shear layer instability, again emphasizing the dominance of this feature on the stability characteristics of the flow. The simulation data also appears to have a twin peak at its maximum, indicating that in the full flow, there are more modes influencing the perturbation distribution than the single $\alpha\delta_* = 1$ wave considered in the linear calculation, and that the assumption of a parallel flow instability, while it does produce surprisingly good agreement, is an overly simple treatment of the problem.

4.1.6 Negative disturbances

We shall briefly discuss some results which derive from the computation of the high-amplitude initial-value problem for a 'negative' disturbance. This disturbance has exactly the same structure and amplitude as the disturbance discussed thus far, but with opposite sign. There was some discussion of this kind of disturbance in the

previous chapter, and this is an extension of those results. The comparison of the two disturbances: one with $A = 0.2$ (a 'positive' disturbance) and the other with $A = -0.2$ (a 'negative' disturbance) highlights the similarities and the differences between the two that arise from the linear and nonlinear processes that influence these strong disturbances. The results presented here only cover the time range from $t = 0$ to 100, and so the results at later times cannot be compared. This was because of the limited time available at NASA Ames for carrying out these calculations, and it is hoped that in the future the later times will be calculated.

The vertical structure of the streamwise perturbation velocity (Figure 4.14) shows the formation of the shear layer and the effect of the algebraic instability that causes it to elongate. This initially looks very similar to the positive disturbance except that the distorted profile that arises from the initial perturbation is not an inflectional shear layer, but a fattened profile near the wall and a decelerated region further away, towards the free stream. As with the positive disturbance, this flow structure is a consequence of the lift-up effect, and we observed in Chapter 3 that for a weak disturbance, the transient will decay leaving the wave modes which are identical and of opposite sign to the wave structure of the positive disturbance. For higher amplitudes, as Figure 4.14 indicates, the transient does not decay but grows. The mechanism by which the negative disturbance grows has some similarities with the positive disturbance, but also some differences. The appearance of long high-speed strips in the streamwise velocity (Figure 4.15) is very similar to the patterns that characterized the positive disturbance. Even the power spectra of the v component (Figure 4.16) show the growth of a new peak at $\alpha\delta_* = 0.15, \beta\delta_* = 1.0$ which is at a similar location in wavenumber space to the peak that emerged in the positive disturbance. This suggests that it is probably the same nonlinear mechanism that generates these strips, despite the opposite starting

configuration.

However, the second mechanism that was seen to drive the evolution of the positive disturbance - the secondary wave growth - is not observed here. Neither the v velocity contours nor the power spectra indicate any two-dimensional wave growth which was observed in the positive disturbance. This is not very surprising since the distorted mean profile does not have an unstable shear layer imbedded in it as did the profile analysed from the positive disturbance. Since there is not an inflectional profile created by the lift-up effect, there will not be any associated wave growth. This is not to say that linear instabilities will not play a role in the disturbance's growth and ultimate breakdown. Although secondary wave growth is not observed here, it is still likely that some part of the disturbance - perhaps off the centerline, or at a later time - will develop a linearly unstable profile. In the presence of a spanwise velocity component, the profile becomes inflectional in nature to a sufficiently oblique wave (cf. Landahl & Mollo-Christensen[48], p93) and thus susceptible to a linear instability. Because of this, the negative disturbance most likely will become unstable as time progresses and the mean profile becomes more distorted. However, for the time span calculated, no instability waves were observed.

One interesting point to note is that the weak nonlinearity observed in Chapter 3 which distinguished between the positive and negative disturbances is again reproduced here, except this time it becomes a dominant feature of the flow. For both the positive and negative disturbances, the features that grow into long, thin streamwise patches of fluid are the *positive* perturbations. In the case of the positive disturbance, the strips develop from the side lobes of the disturbance, while for the negative disturbance, the two elongated strips are created from the single central core of the disturbance which

splits into two. The end result: two high-speed regions on either side of a low-speed region, is the same. This is very similar to the development of the two positive peaks in the weak experiments described in the previous chapter, and suggests that the nonlinear mechanism that is present in the strong disturbances might be the same one as was seen in the weak disturbances and thus might be treated theoretically by a weakly nonlinear analysis. There might also be a strong connection between this kind of nonlinearity and the nonlinear development in the evolution of low-amplitude wave packets seen by Gaster and Grant[20] and Cohen[12]. This analysis is a step which still needs to be taken, but which promises to yield some illuminating information about the nonlinear processes involved in the localized disturbance's evolution.

A last difference between the positive and negative disturbances is shown in Figure 4.17, which plots the peak-to-peak amplitudes of the streamwise disturbance velocity component as a function of time. The solid line shows the amplitude of the positive disturbance while the dotted line shows the amplitude of the negative disturbance. The difference between the two is striking. The positive disturbance grows exponentially with time, while the negative disturbance only grows linearly with time. It is not necessarily true that all of this can be accounted for by the secondary wave growth on the unstable shear layer that was seen in the positive disturbance, but that is one difference between the two that will influence their respective growths.

4.2 Experimental Work

The experiments involving the strong disturbances were carried out using the same techniques as with the weak disturbances discussed in the previous chapter. For these

results, the membrane used to generate the disturbance was the one described in Chapter 3, except that it was positioned so that its long dimension was aligned with the flow. This is in contrast to the weak disturbances which were generated with the membrane positioned across the flow. The reason for the 90° rotation of the membrane was that it was determined that the strong disturbance broke down more easily with the smaller spanwise scale provided by the membrane in the aligned position. In fact, getting the disturbance to break down proved to be somewhat of a problem. The Reynolds number at which the weak measurements were taken ($Re_{\delta_*} = 950$) proved to be too low to be able to create a controlled but unstable disturbance with a reasonable amplitude, and so the free-stream velocity was increased for the strong disturbances from 6 m/s to 7.5 m/s, increasing the Reynolds number at the point of generation to 1050. At this velocity, the disturbance structure was controlled, but it broke down very rapidly, becoming turbulent by $\Delta x/\delta_* = 75$. There did not seem to be any middle ground in adjusting the velocity: either the disturbance remained laminar, with the transient slowly decaying, or it broke down very quickly. As the results will show, these changes in the operating conditions did not fundamentally change the kind of disturbance generated, or the kind of phenomena observed in the disturbance's evolution. However, the structure generated did differ in some respects from both the low-amplitude disturbances measured and the numerical results presented in the previous section. These differences will be discussed later on in the chapter.

The measurements of the evolution of the localized disturbance reproduce several of the features that were observed in the numerical results. The streamwise perturbation velocity, shown in Figures 4.18 and 4.19 show the creation of the shear layer by the lift-up of fluid elements and the subsequent breakdown of the shear layer by what appears to be the secondary wave growth on the distorted mean profile. As with the Navier-

Stokes calculations, the wave growth has its origin in the shear layer created by the lift-up of fluid forced by the membrane's motion. Specifically, the break-down occurs in the decelerated region of the disturbance where the distortion of the Blasius flow is at a maximum and yields an unstable inflectional profile. Since we are measuring the streamwise velocity perturbations, the wave motion is not as clear as it would be had we access to the normal velocity component. As we discussed earlier, this is because the vertical velocity component is not contaminated by the effects of fluid lift-up and the vertical vorticity modes inherent in the three-dimensional disturbance. However, despite this, the waves become so large, that they are still reflected in the streamwise component.

These results must be interpreted carefully because the assumption of a frozen flow field that allowed us to use a Taylor's hypothesis in the discussion of the results in Chapter 3 is probably no longer true. As Figure 4.18 indicates, the development of the structure between $\Delta x/\delta_* = 18.9$ and $\Delta x/\delta_* = 47.1$ is quite rapid, and we must conclude that the structure is evolving as it travels past the stationary hot-wire probe. This means that we can no longer infer detailed spatial information about the flow from the temporal record. The spatial structure will show the same features that we observe in the time series - the shear layer, the elongation of the disturbance and the wave growth etc, but the association between temporal and spatial structure is no longer straightforward.

The spanwise structure of u also agrees quite well with the picture presented in the calculations with a few notable differences. From the very first x-location the structure of the disturbance does not exactly correspond to the structure seen in the numerical simulation. Whereas the numerical results started with the familiar low-speed – high-

speed regions of u, one following the other, the experimental results are strongly skewed towards the low-speed region. The high-speed region, created by the membrane's return to its rest position, is present but much weaker. The consequence of this is that the strong streamwise strips that were observed to develop in the Navier-Stokes calculations appear almost instantly in the measurements, and they intensify and elongate further as the structure moves downstream. These strips grow predominantly in the front of the structure, but by $\Delta x/\delta_* = 37.7$ a second peak appears in the rear part of the strip. This splitting of a single oblique strip to two smaller strips was also observed in the numerical results and it was associated there with the series of cascading peaks in the power spectra and the development of higher harmonics. In keeping with the character of the strong disturbance, the dispersive wave field accompanying the disturbance is negligibly small in comparison to the transient core. The low speed lobes on either side of the main disturbance are all that we see of the associated wave packet, and this is in good agreement with what was observed in the numerical calculations.

Spanwise velocities

The spanwise velocities measured (shown in Figure 4.20) do not agree very well with the corresponding results from the numerical simulation and the differences stem from the same differences that were noted in the streamwise velocities. Whereas the numerical results showed the four-leafed w-structure that was present in the initial conditions, the experimental results show only two streamwise strips, and only a hint of the second pair of w lobes. At $\Delta x/\delta_* = 28.3$, the four lobes are visible, flanked on either side by two long strips, but at earlier x-locations, there is only a suggestion that this four-fold structure is present in the disturbance. Since the anti-symmetry of the measurements

is generally very good, their accuracy is not suspect, and we must conclude that the disturbance generated by the membrane is significantly different from the analytic disturbance computed in the previous section. The two w lobes that we see correspond to a flow converging towards the centerline, and this is consistent with the motion of the membrane during the disturbance's generation. The upward motion of fluid generated by the membrane's upward motion will do two things: firstly it lifts up fluid elements from near the wall creating the low-speed region seen in the u contour plots. Secondly, the positive v will force a converging spanwise flow near the wall and a diverging w field away from the wall in order to satisfy continuity. Since we are measuring close to the wall ($y/\delta_* \approx 0.5$), we will measure that converging flow. If we assume that for some reason, the return motion of the membrane is weak, it will not pull down very much high-speed fluid (resulting in a weak high-speed region in the u signal) and also will not induce a very strong spanwise flow pattern - resulting in a weak diverging flow at the back of the disturbance.

This explanation seems to account for the flow structures observed, but the question remains as to why the membrane's motion is so biased towards the upward part of the cycle and why the return movement of the membrane does not induce a strong flow field. We should note that the weak disturbance did not exhibit this problem, and the upward and downward motions of the membrane created equal amplitude perturbations in the streamwise and spanwise velocity components. This problem is therefore not intrinsic to the membrane itself, but only when it generates large amplitude disturbances.

The strength of the upward motion, and the long streamwise extent of the low-speed region in the u component can be explained by the orientation of the membrane. For the strong disturbance, the membrane was positioned such that it lay aligned with the flow.

This means that when the membrane moved up, a long column of fluid was pushed up, creating the long low-speed region in the u and the long region of converging spanwise flow that we observe. This explains what we *do* see, but not what we *don't* see, and the weakness of the return motion is still a mystery. One possibility is that when the pressure is released from the membrane during the return cycle, the escaping air is choked by the physical design of the valve and instead of losing pressure instantly, there is a slow return to equilibrium. This would mean that the membrane returns to its rest position rather slowly, and does not pull down very much fluid as it moves. Another cause might be related to the change in orientation of the membrane - from lying with the flow to lying across the flow, although it is not clear how the orientation or of the membrane would cause these differences to appear.

4.3 Flat Eddy Calculations

The Flat-Eddy equations that were developed in Chapter 3 were integrated for the case of strong disturbance, and the results can be compared with the Navier-Stokes results and the experimental measurements. As was discussed in the previous chapter, the flat-eddy approximation gives the behaviour of the transient part of the disturbance, while ignoring the dispersive effects and the redistribution of momentum by pressure gradients. For the weak disturbance, this gave a good qualitative agreement with the experimental results but it was noted that in the weak disturbance, the dispersive portion of the disturbance is ultimately important since the transient decays. For this reason, the flat-eddy equations could only model short time behaviour. In contrast to this, we have seen that the strong disturbance is characterized by the fact that the wave modes associated with the initial disturbance are essentially unimportant. This is not

to say that wave modes in general are unimportant as we have seen that one of the growth mechanisms for the disturbance is secondary wave growth. The pressure field results, from the full simulation, indicated that the horizontal pressure gradients are not initially very large although they do develop and this will introduce errors in the flat-eddy solutions. Despite this, however, the flat-eddy equations should successfully model the initial lift-up and algebraic growth of the disturbance as well as the nonlinear mechanisms that are associated with the development of the high-speed strips that are observed in the streamwise velocity perturbations in both the Navier-Stokes solutions and the experimental results. All of these effects were first observed in the early stages of the disturbance's evolution, and before the very strong pressure gradients developed.

The flat eddy equations (Eqns 3.56 – 3.58) were integrated as before with a fourth-order Runge-Kutta method. The initial conditions used were the pair of counter-rotating eddies that have been used thus far, and the amplitude factor was chosen to be $A = 0.2$. This is the same amplitude as was chosen for the Navier-Stokes simulation.

The results, shown in Figure 4.21 and 4.22 do indeed give the features that we expected. The cut through the boundary layer along the centerline, (Figure 4.21) shows the formation of the shear layer, the strong intensification of the decelerated region and the decreasing intensity of the accelerated region. This is in agreement with all of the results thus far, and needs no more comment. The $x - z$ plot, in Figure 4.22 is also very similar to the previous flat eddy calculation, but this time, the similarities with the strong disturbance are more evident. As we had predicted, one main feature of the flow that the flat-eddy calculation was able to reproduce was the development of the alternating strips of high-speed and low-speed fluid. In good qualitative agreement with the full simulation, the flat-eddy calculation indicates that front part of the disturbance

quickly becomes the dominant part, leaving the rear part behind. Of course, there are significant differences between the flat-eddy approximation and the full simulation. The high-speed strips are at an angle to the x-axis in the Navier-Stokes solution, while they lie aligned with the flow in the flat-eddy results. This is probably due to a nonlinear wave interaction which of course will be missing in the flat-eddy solution. Also, the flat-eddy results grow unbounded for large times, and the equations blow up[63]. This singularity derives from the lack of viscous dissipation and pressure redistribution of momentum, and it limits the extent of the calculations to moderate times. However, as a first approximation to what the disturbance will look like, the flat-eddy calculations are a good (and cheap) guide.

4.4 Summary

The analysis of a strong localized disturbance incorporates many of the concepts that were introduced in the discussion of the weak disturbance. The disturbance can still be thought of as consisting of two portions: a wave part and a transient part. However, unlike the weak disturbance, the transient portion of the flow no longer decays but grows and provides a platform for the rapid nonlinear breakdown of the disturbance to a turbulent spot. Two mechanisms for this breakdown have been identified. The first is a nonlinear mechanism by which long strips of high-speed fluid surrounding a low-speed region develop in the front of the disturbance. This was seen to occur for both positive and negative disturbances (i.e. disturbances of identical structure but opposite sign) and there was evidence that the mechanism 'cascaded' - that is to say that the power spectra seemed to indicate a similarity between scales. A similar nonlinear mechanism was also observed in the weak disturbances (Chapter 3), and it is thought that the two

may be driven by the same underlying process.

The second mechanism observed was the growth of a linear instability wave on the distorted mean velocity profile. The initial lift-up of fluid was strong enough to create an inflectional mean profile. This profile remained inflectional for a sufficiently long time (before being stretched out and dissipated by viscosity) to enable a linear, two-dimensional wave to grow. The instability was characteristic of a free-shear instability, with growth rates an order of magnitude larger than the Tollmien-Schlichting modes for a Blasius boundary layer, and a domain of instability spanning a wide range of wavenumbers.

In all of this discussion, the role of the wave modes associated with the initial disturbance is minimal. A low-amplitude wave packet does accompany the disturbance, and it does grow slowly. However, the growth of the disturbance that is associated with the transient is much faster and ultimately, the wave packet does not contribute significantly to the development of the disturbance.

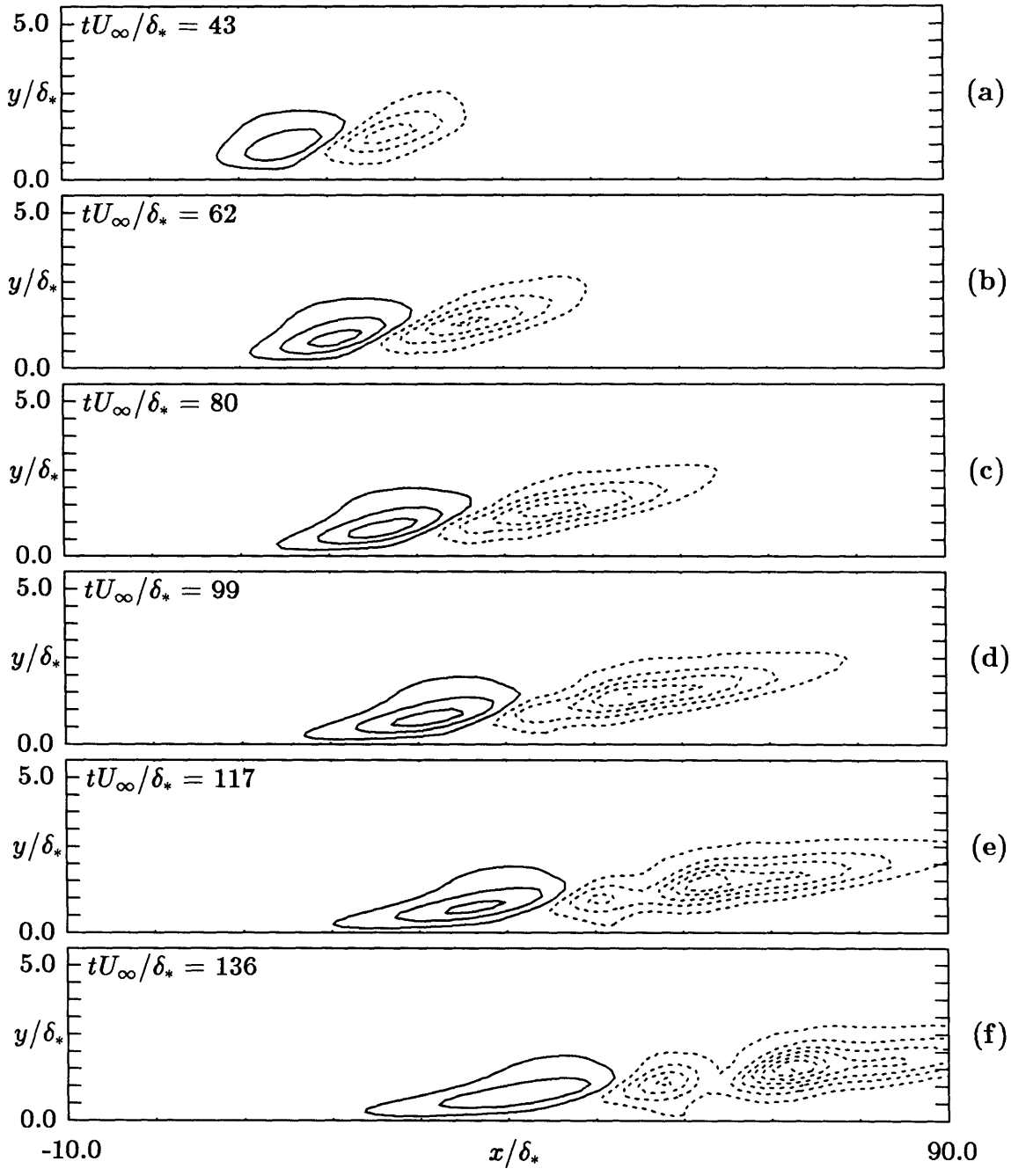

Figure 4.1: Full simulation. Contours of streamwise perturbation velocity at $z = 0.0$. Contour levels: $0.02U_\infty$. Solid lines represent positive contours, dotted lines represent negative contours.

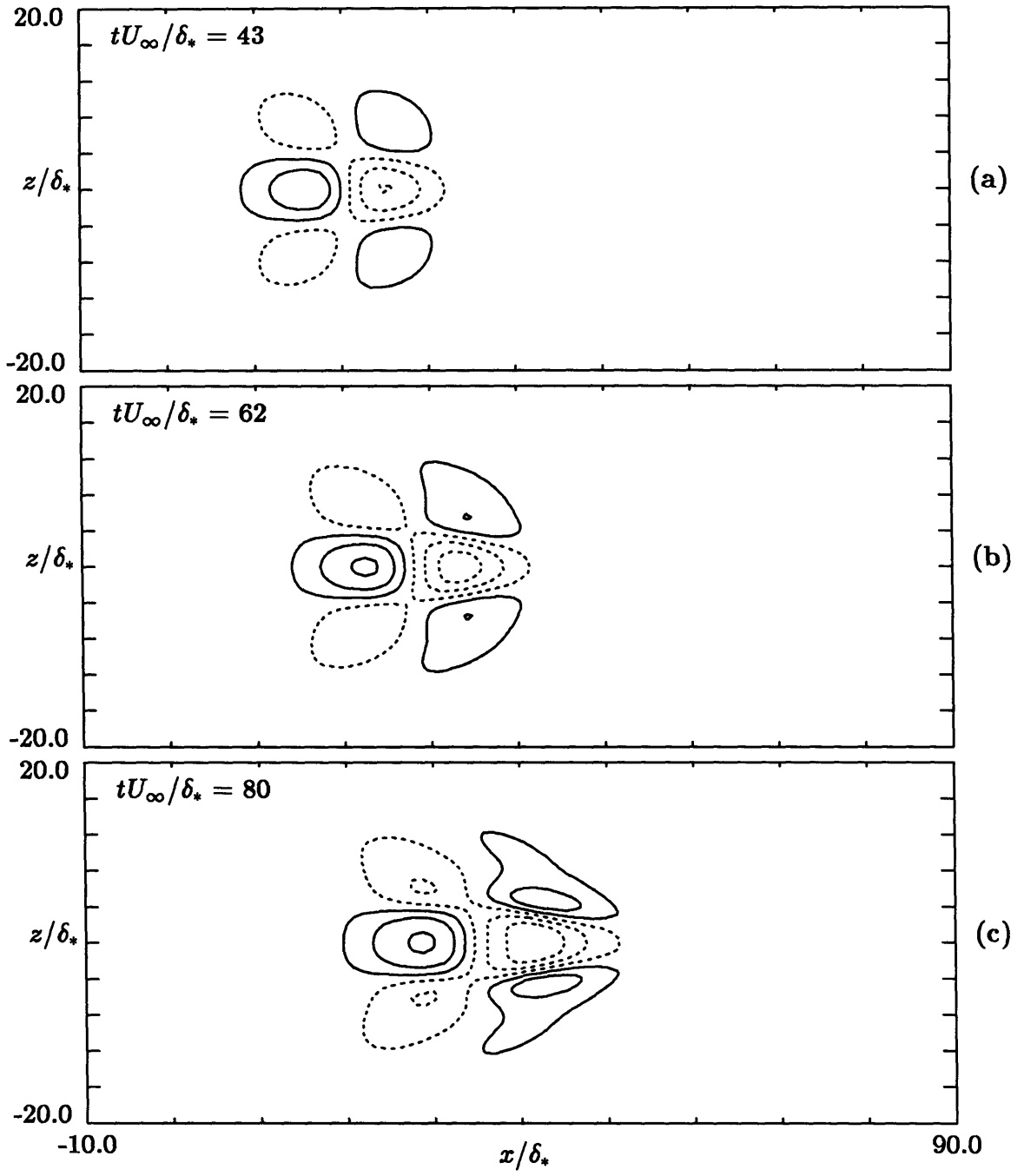

Figure 4.2: Full simulation. Contours of streamwise perturbation velocity at $y/\delta_* = 1.05$. Contour levels: $0.02U_\infty$. Solid lines represent positive contours, dotted lines represent negative contours.

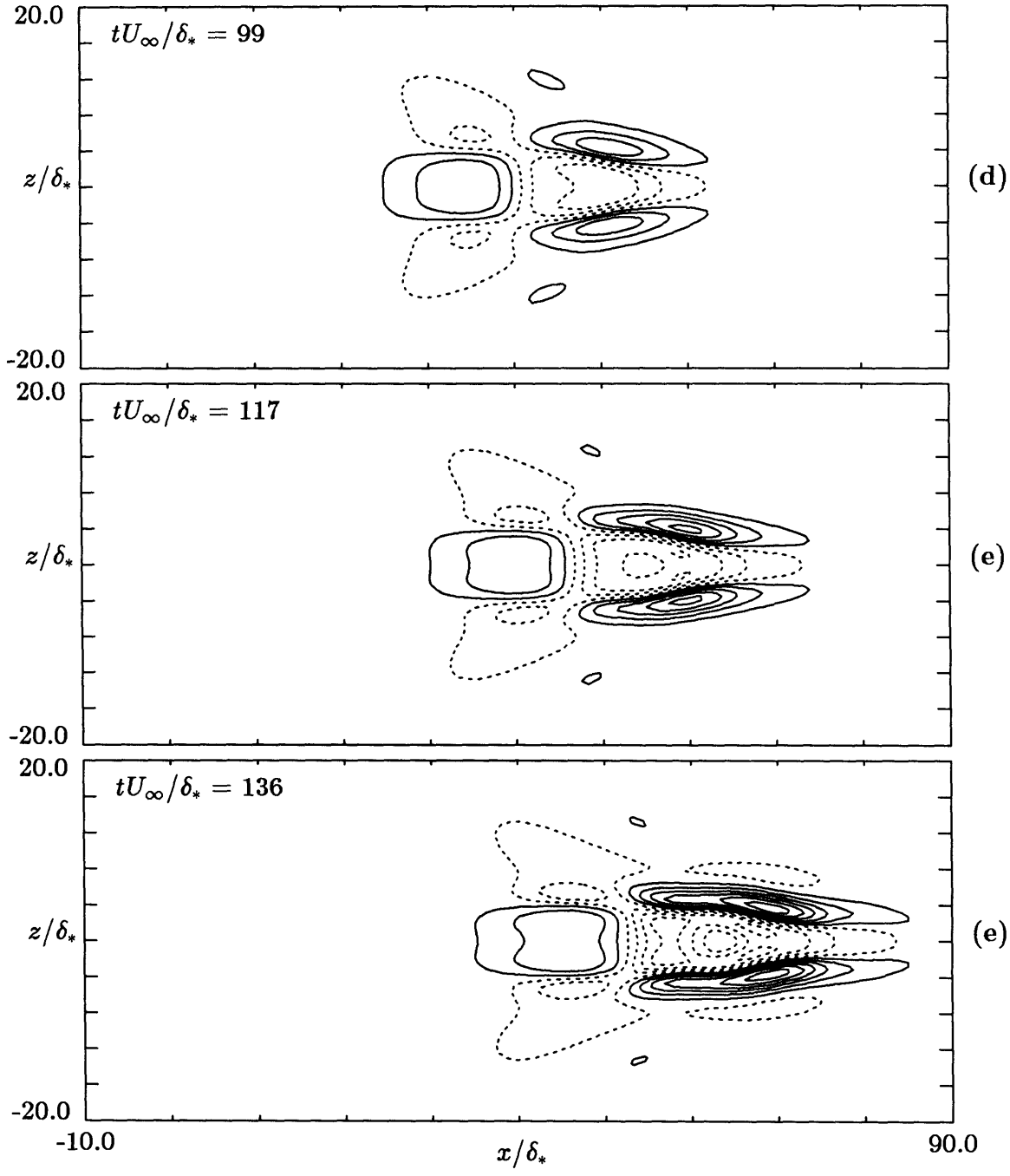

Figure 4.2: (Continued). Full simulation. Contours of streamwise perturbation velocity at $y/\delta_* = 1.05$. Contour levels: $0.02U_\infty$. Solid lines represent positive contours, dotted lines represent negative contours.

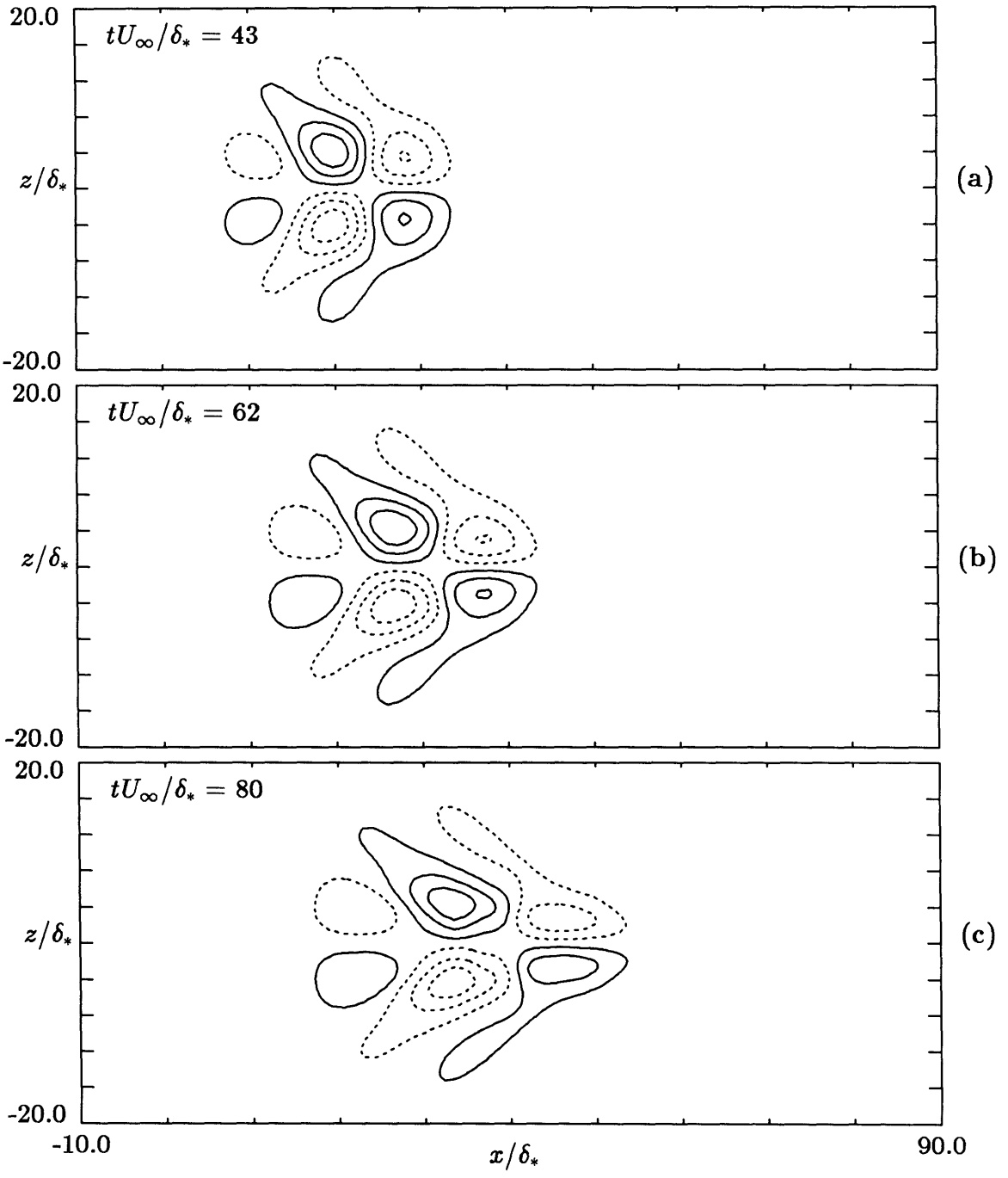

Figure 4.3: Full simulation. Contours of spanwise velocity perturbations at $y/\delta_* = 1.05$. Contour levels: $0.01U_\infty$. Solid lines represent positive contours, dotted lines represent negative contours.

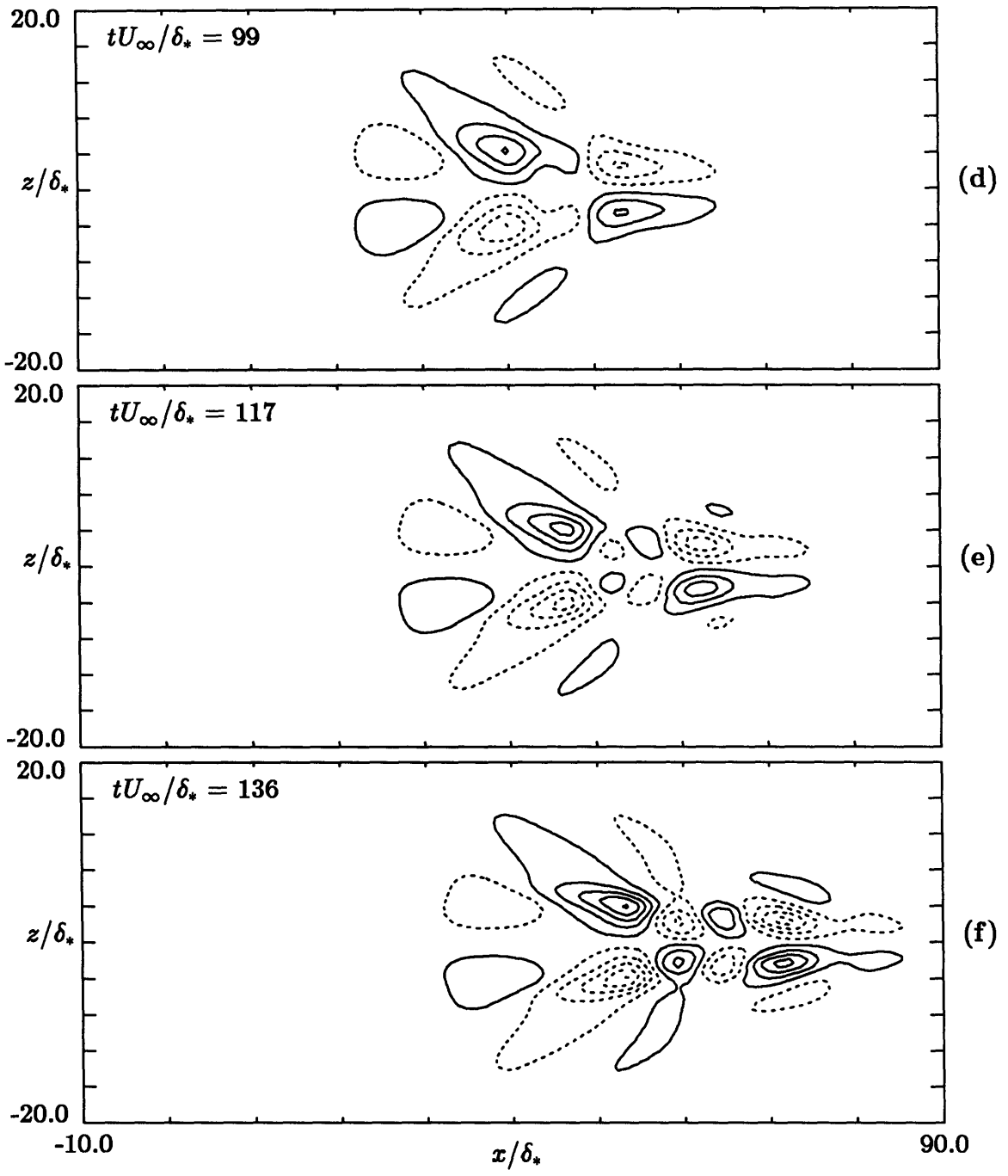

Figure 4.3: (Continued). Full simulation. Contours of spanwise velocity perturbations at $y/\delta_* = 1.05$. Contour levels: $0.01U_\infty$. Solid lines represent positive contours, dotted lines represent negative contours.

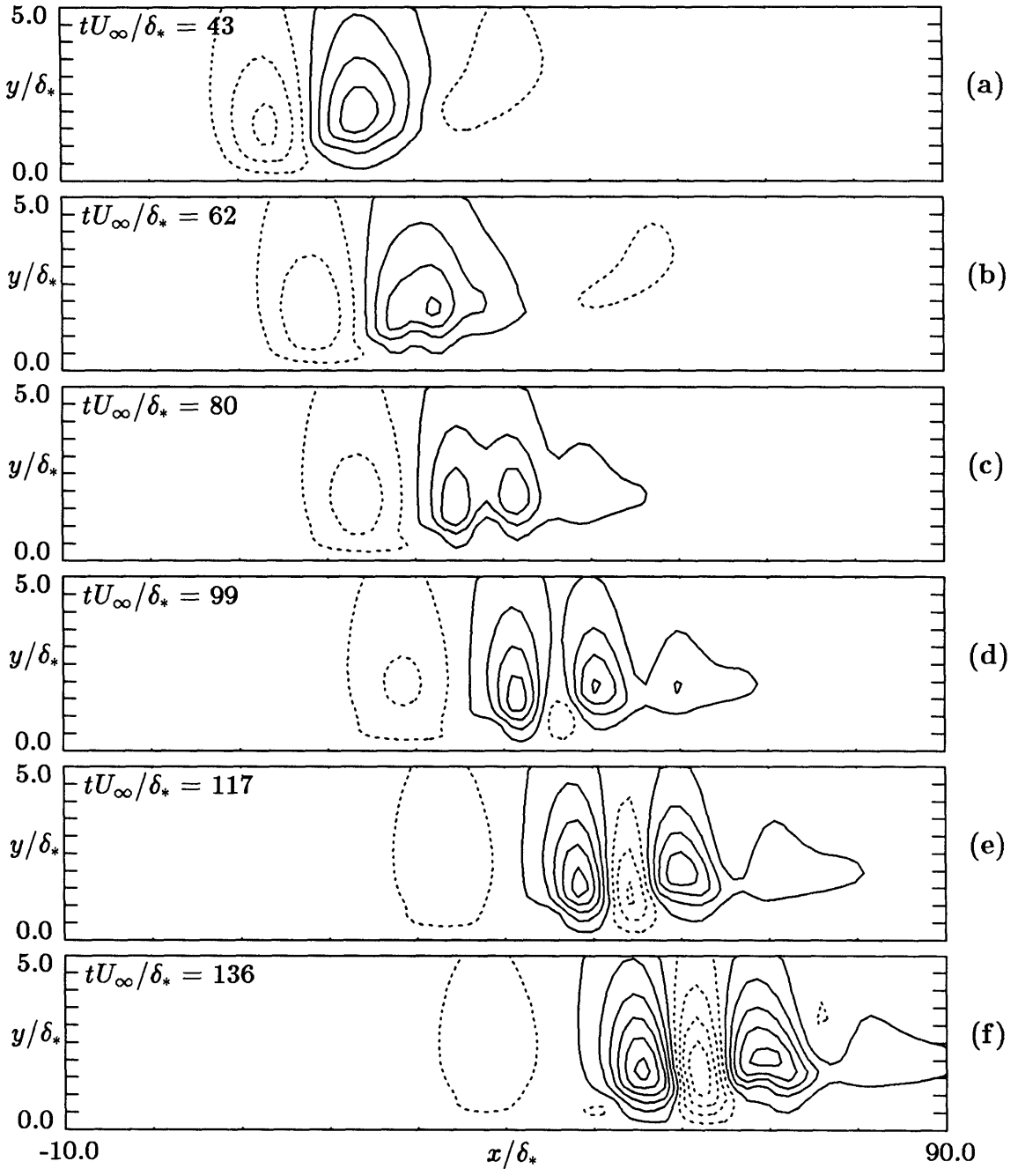

Figure 4.4: Full simulation. Contours of normal velocity at $z = 0.0$ Contour levels: $0.002U_\infty$. Solid lines represent positive contours, dotted lines represent negative contours.

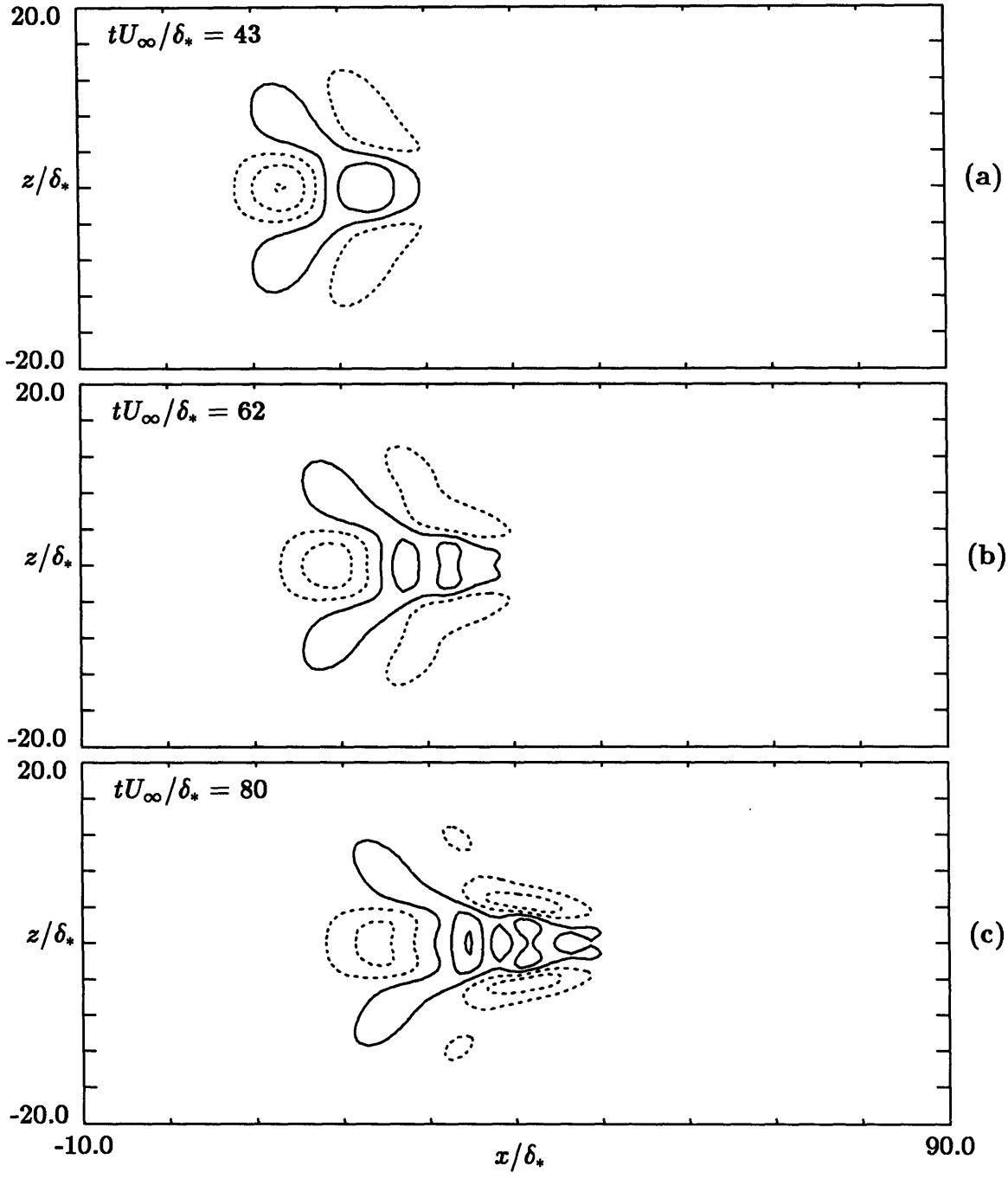

Figure 4.5: Full simulation. Contours of normal velocity at $y/\delta_* = 1.05$. Contour levels: $0.002U_\infty$. Solid lines represent positive contours, dotted lines represent negative contours.

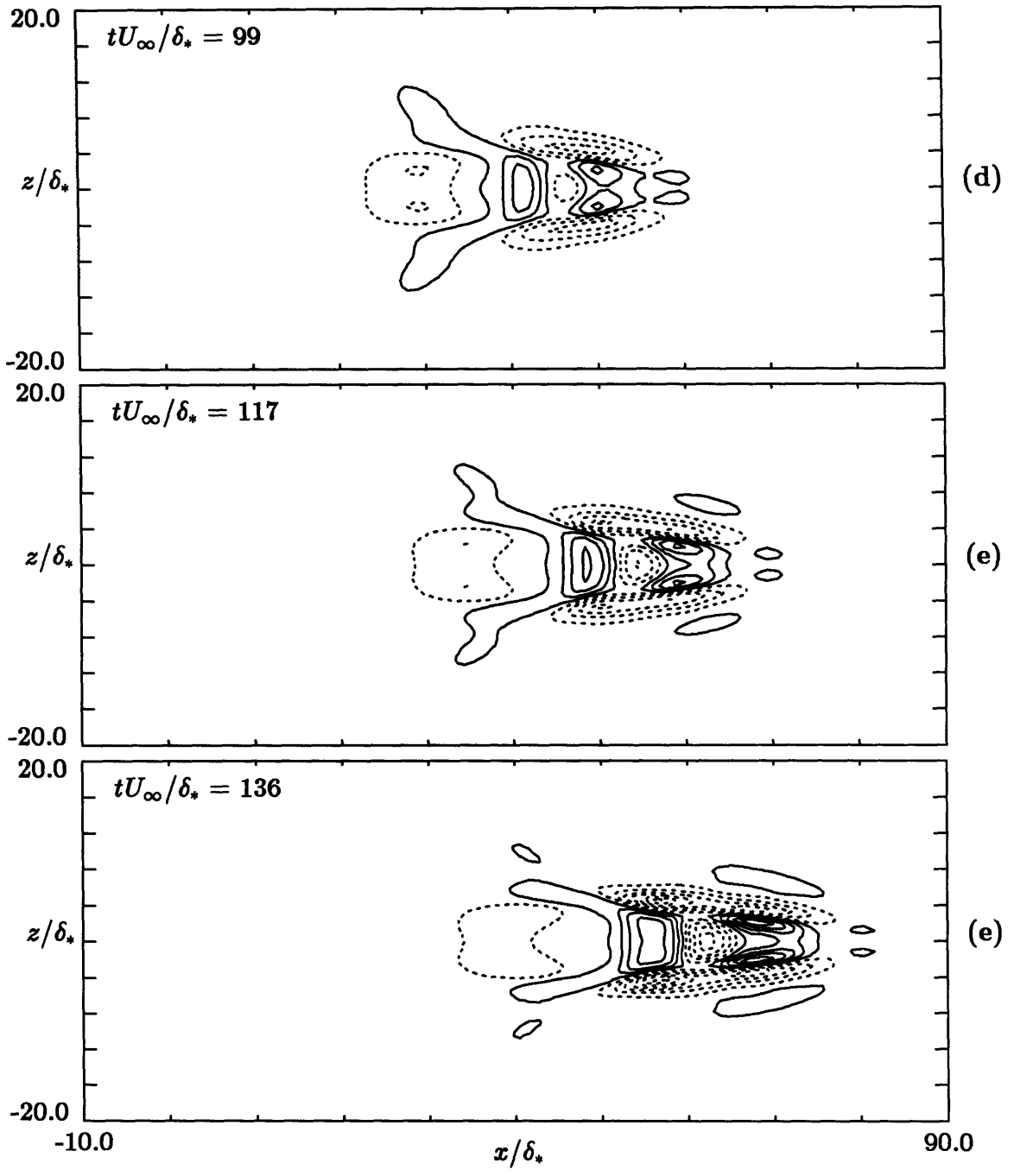

Figure 4.5: (Continued). Full simulation. Contours of normal velocity at $y/\delta_* = 1.05$. Contour levels: $0.002U_\infty$. Solid lines represent positive contours, dotted lines represent negative contours.

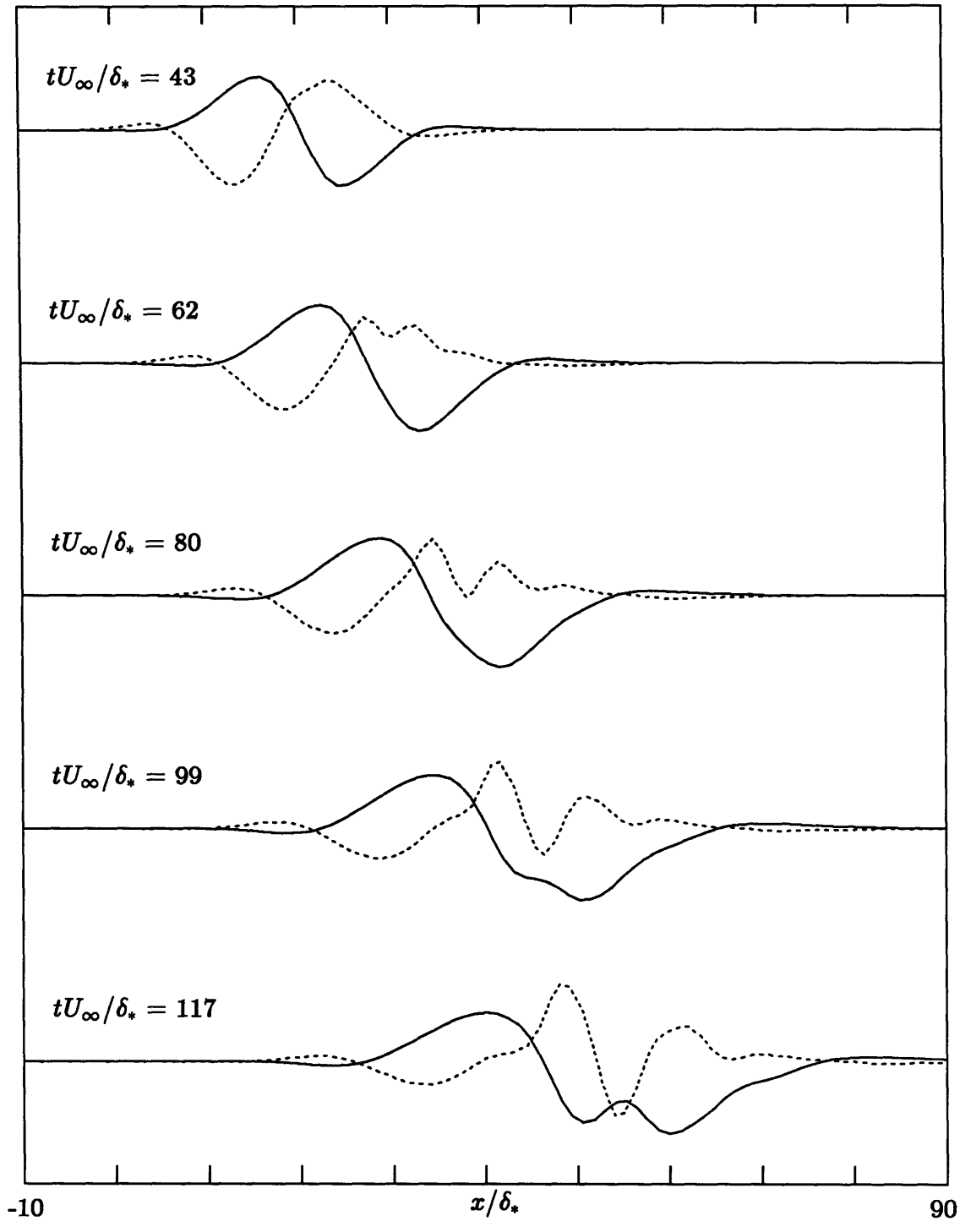

Figure 4.6: Full simulation. u and v components of velocity at $z = 0.0$, $y/\delta_* = 1.05$. v signal magnified $\times 10$.

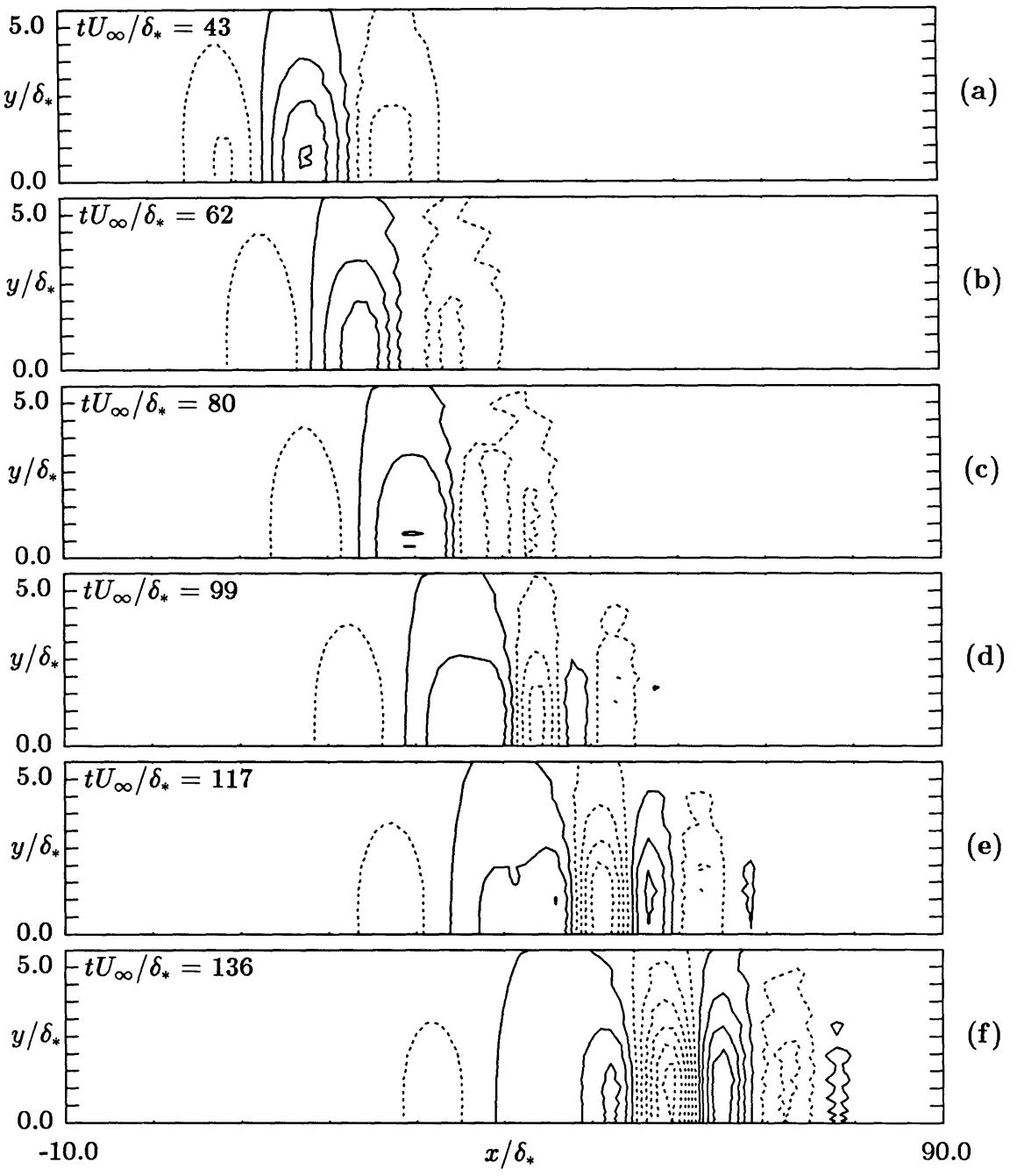

Figure 4.7: Full simulation. Contours of pressure at $z = 0.0$. Contour levels: $0.001U_\infty^2/\rho$. Solid lines represent positive contours, dotted lines represent negative contours.

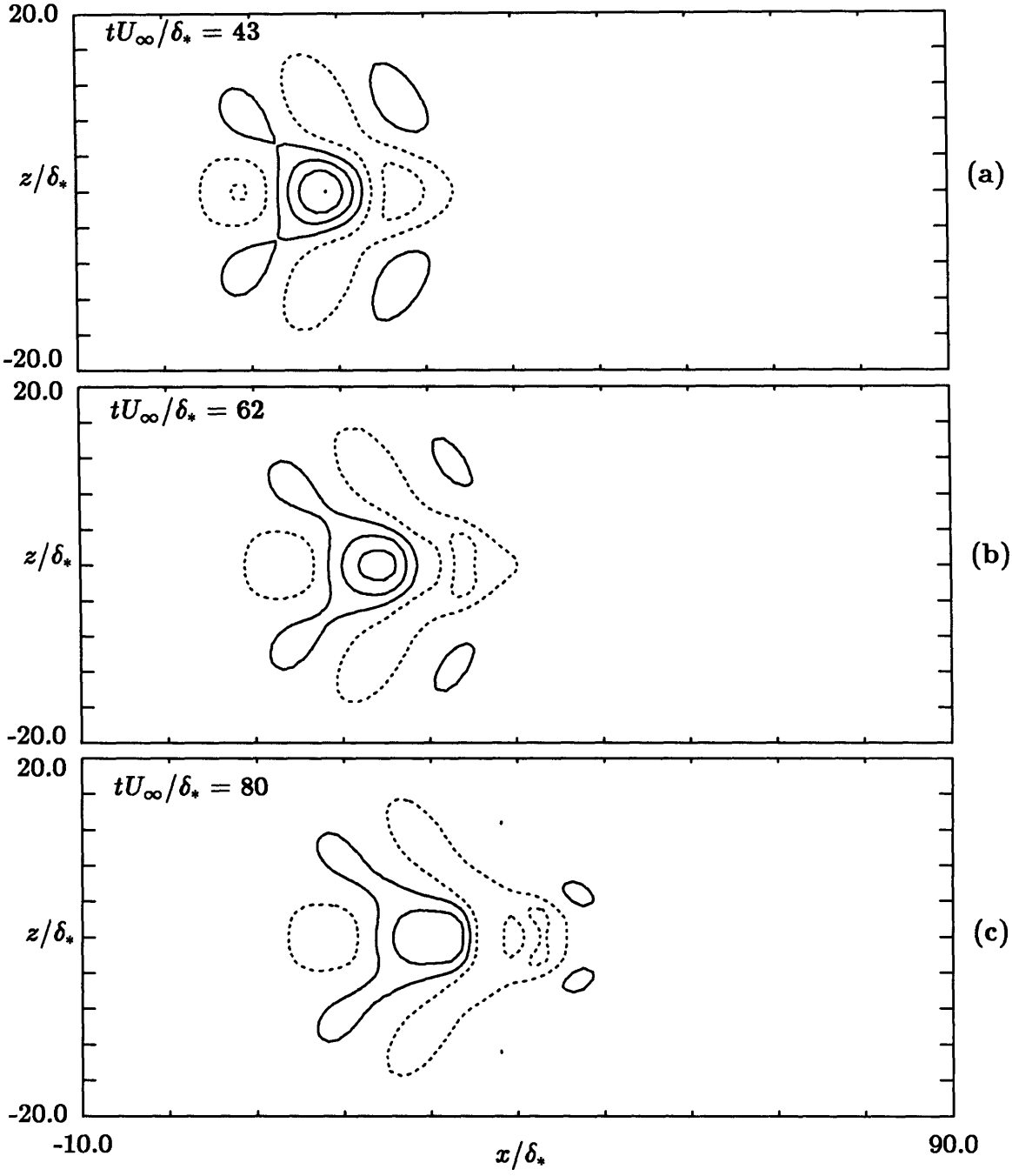

Figure 4.8: Full simulation. Contours of pressure at $y/\delta_* = 1$. Contour levels: $0.001U_\infty^2/\rho$. Solid lines represent positive contours, dotted lines represent negative contours.

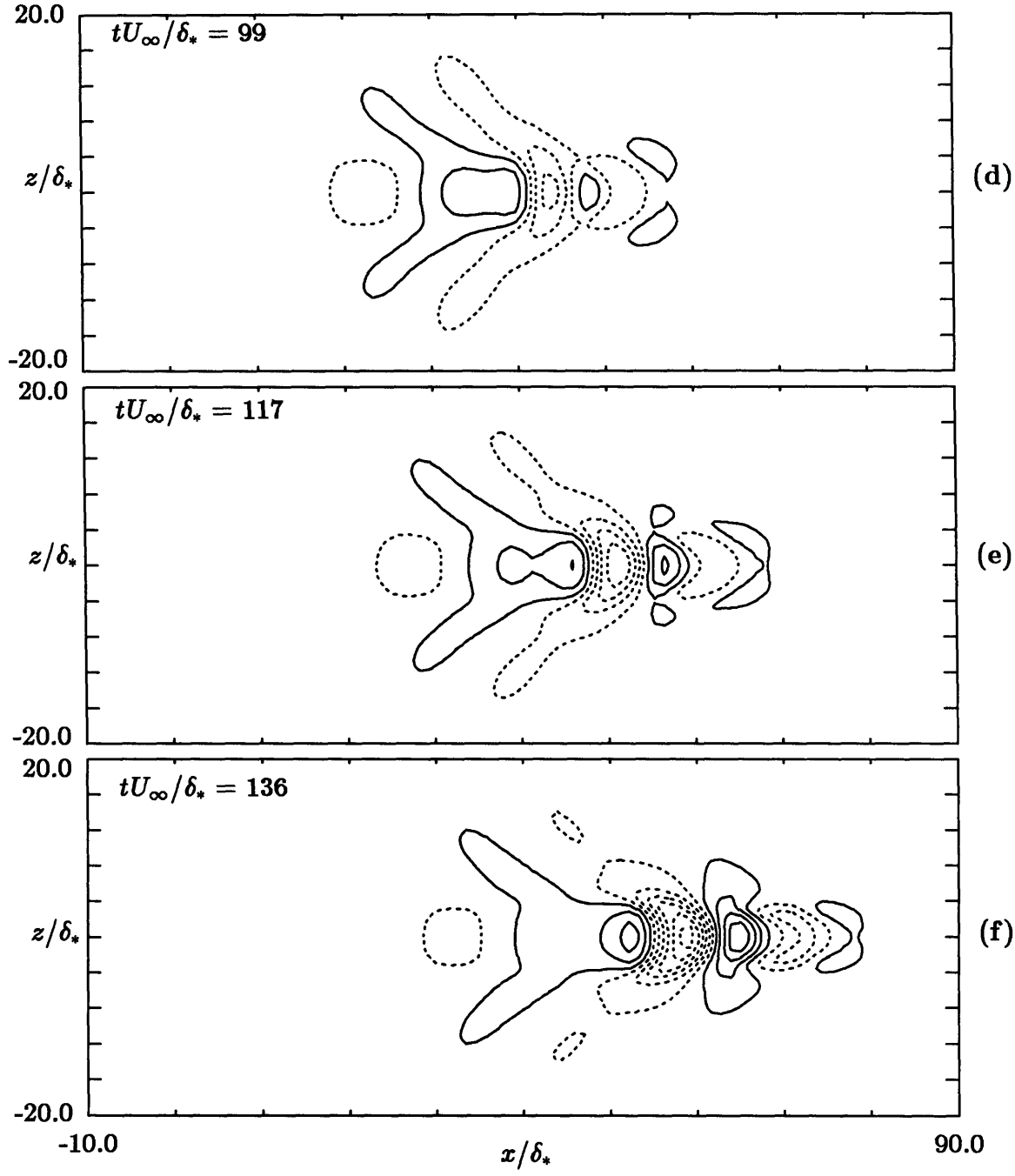

Figure 4.8: (Continued). Full simulation. Contours of pressure at $y/\delta_* = 1$. Contour levels: $0.001U_\infty^2/\rho$. Solid lines represent positive contours, dotted lines represent negative contours.

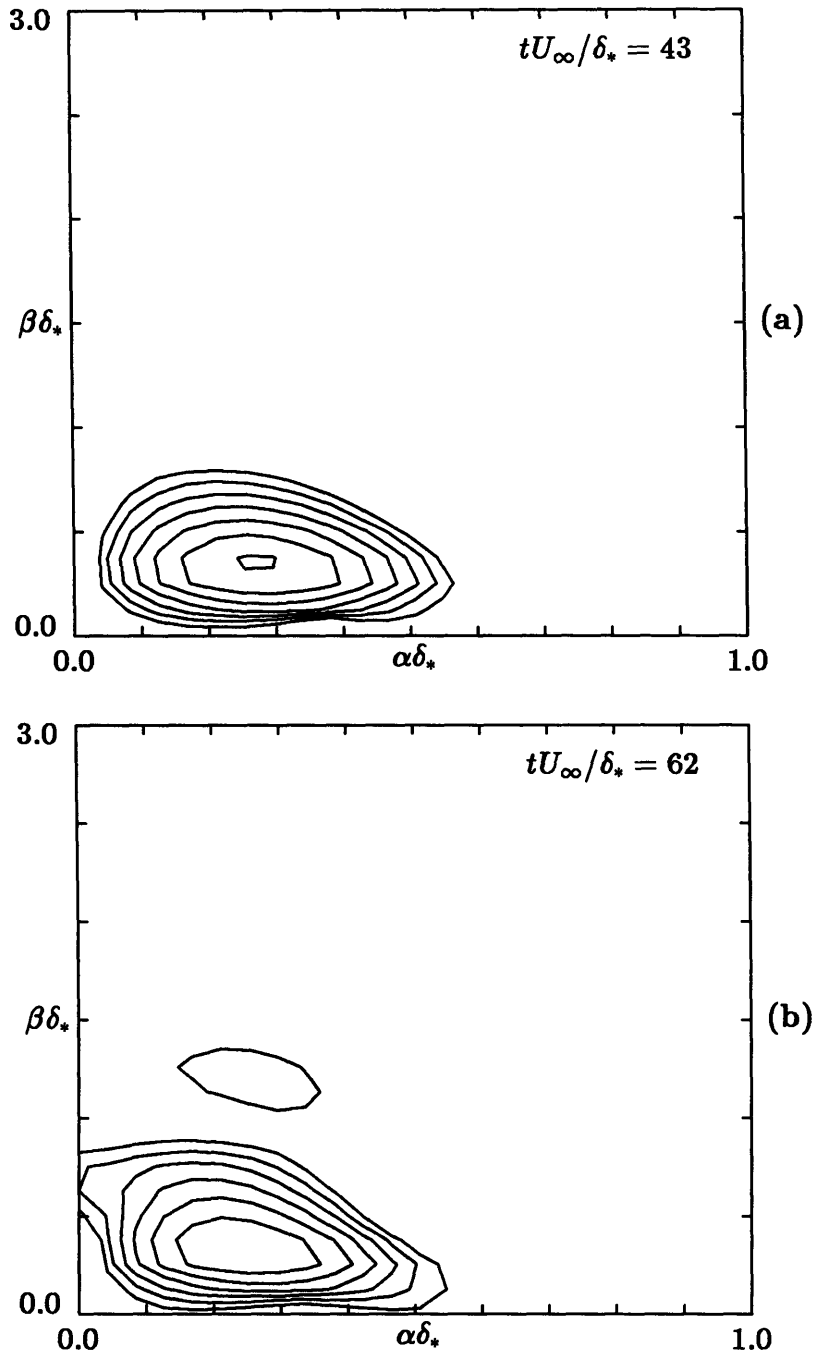

Figure 4.9: Full simulation. Power spectra of v component of velocity at $y/\delta_* = 1.05$. Contour levels are plotted on a logarithmic scale.

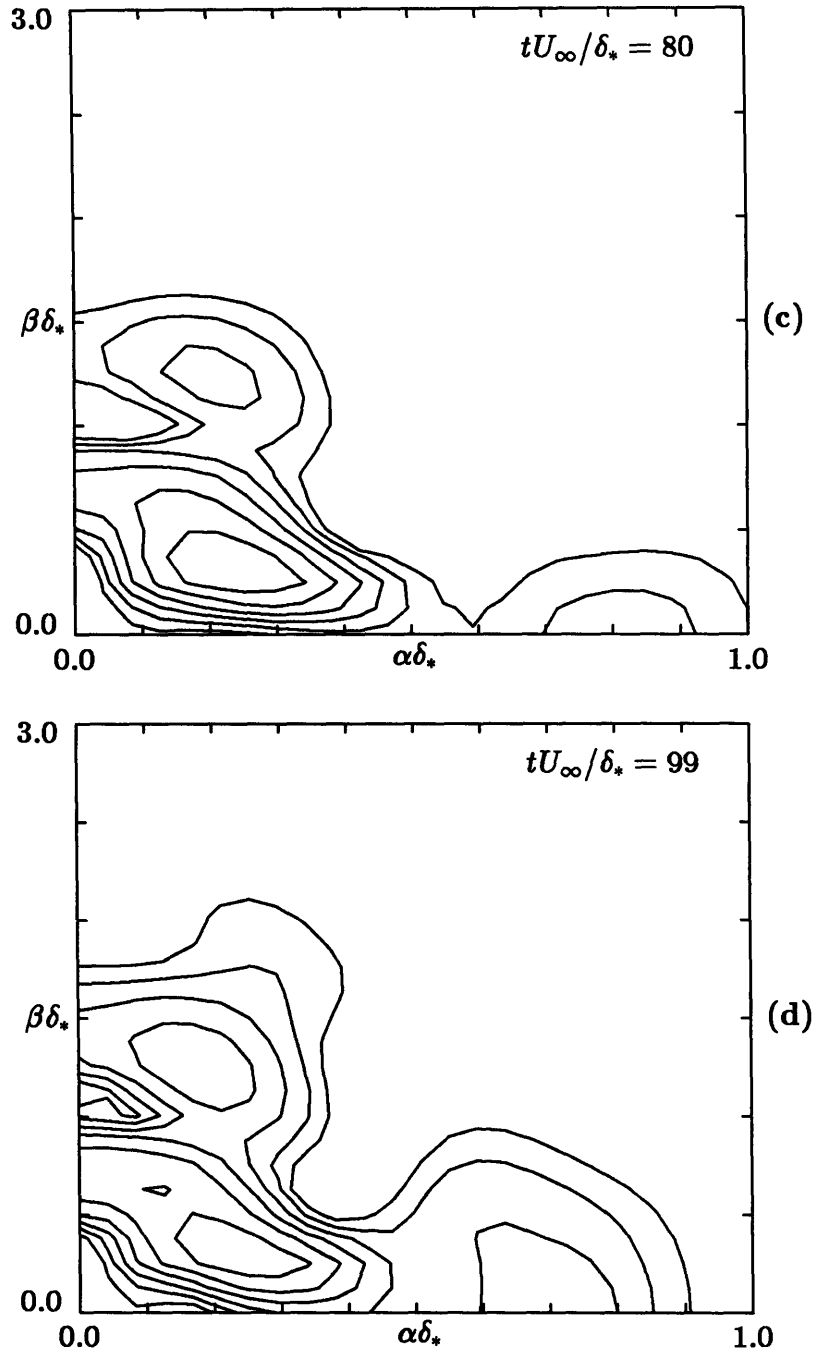

Figure 4.9: (Continued). Full simulation. Power spectra of v component of velocity at $y/\delta_* = 1.05$. Contour levels are plotted on a logarithmic scale.

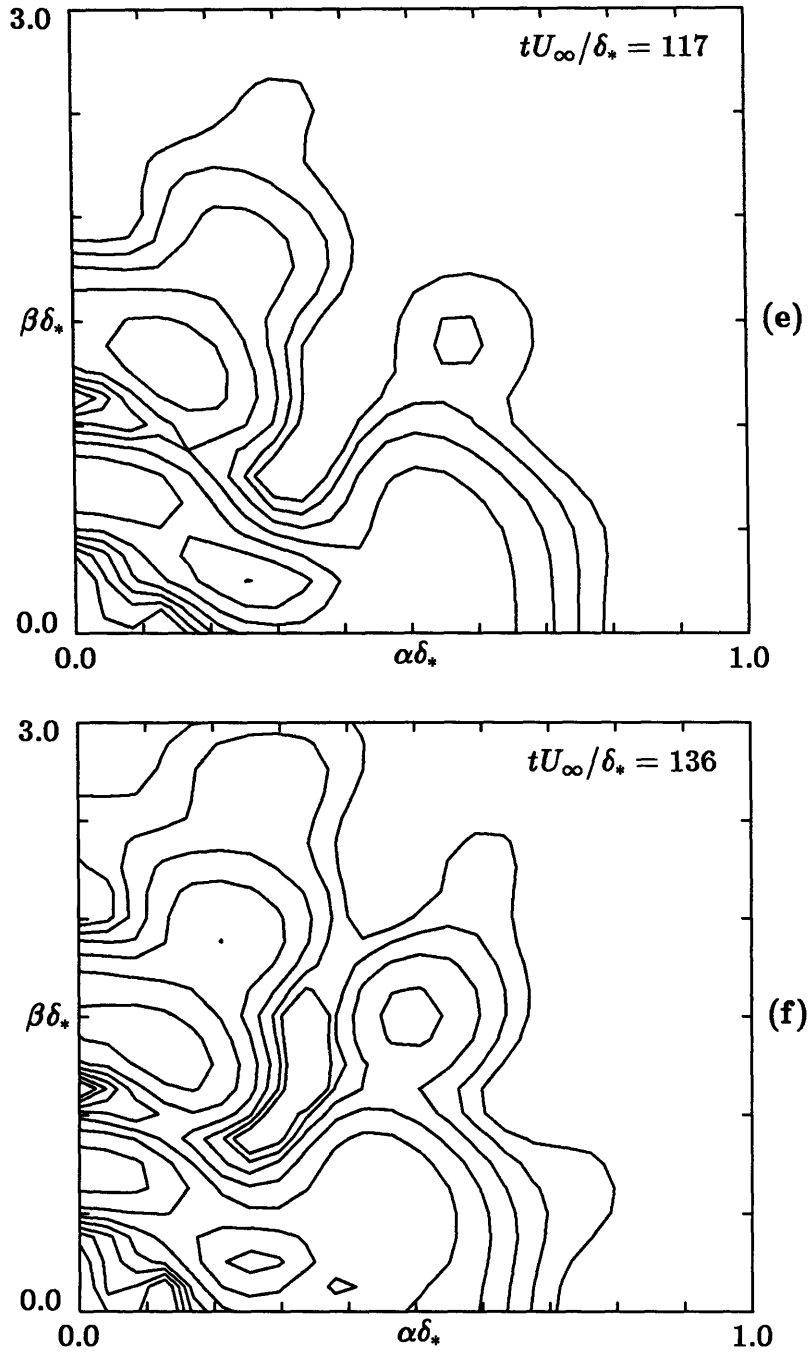

Figure 4.9: (Continued). Full simulation. Power spectra of v component of velocity at $y/\delta_* = 1.05$. Contour levels are plotted on a logarithmic scale.

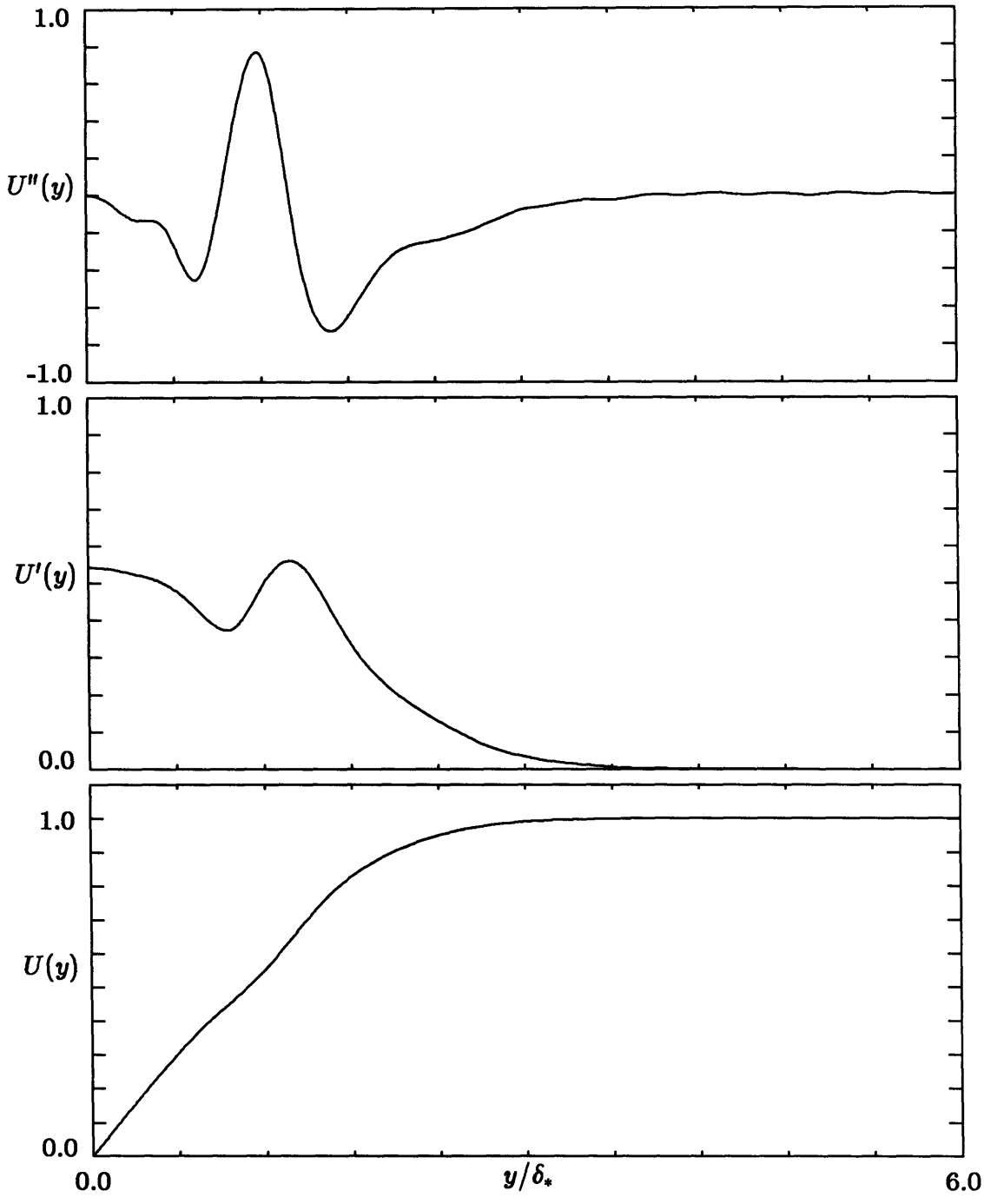

Figure 4.10: Distorted velocity profile, it first and second derivatives used in linear stability calculations. Extracted from the numerical simulation field at $t = 62, x = 33, z = 0.0$

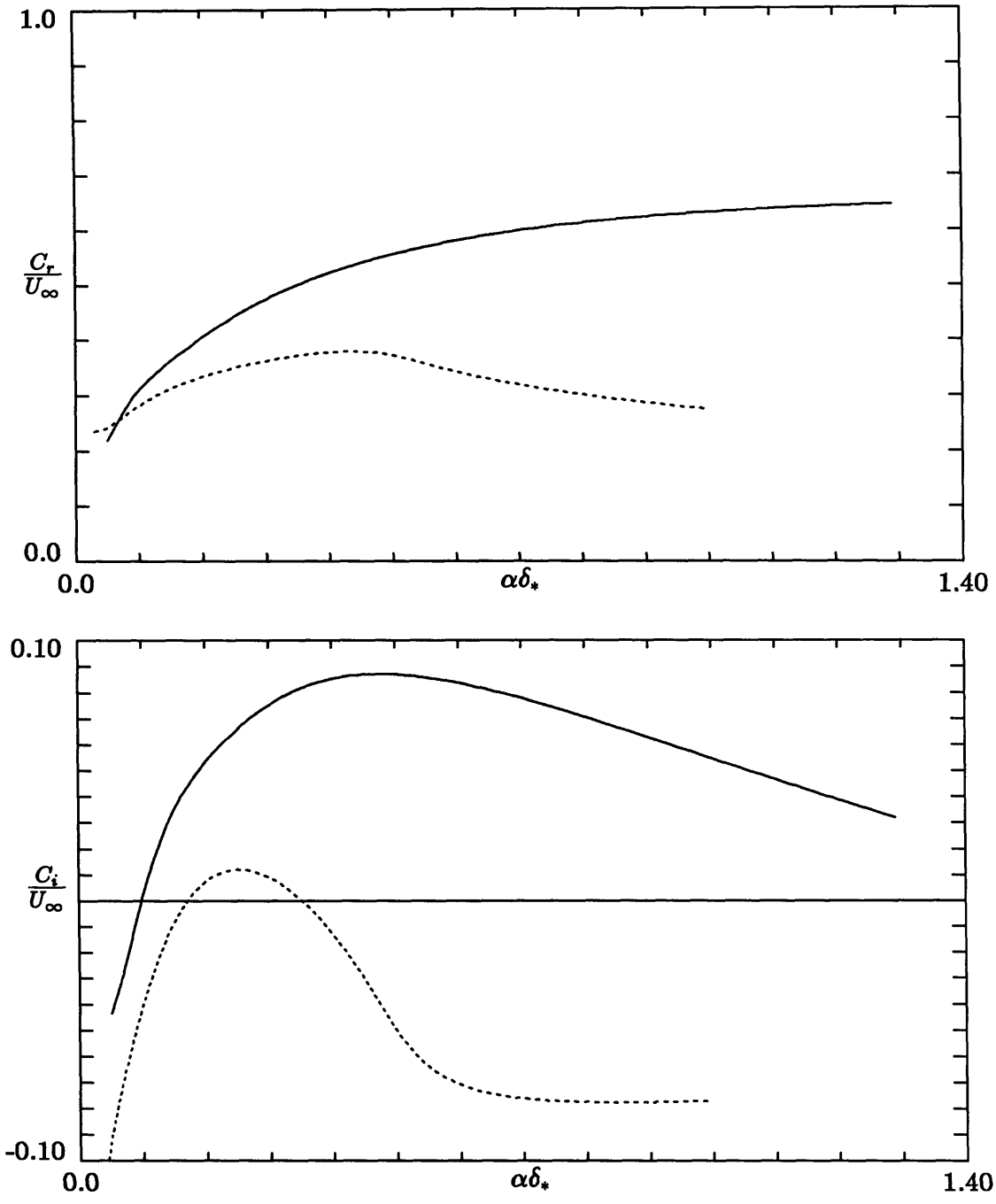

Figure 4.11: Linear dispersion relation, $C_r(\alpha)$ and $C_i(\alpha)$, for the perturbed velocity profile (Solid lines) and the Blasius profile (Dotted lines)

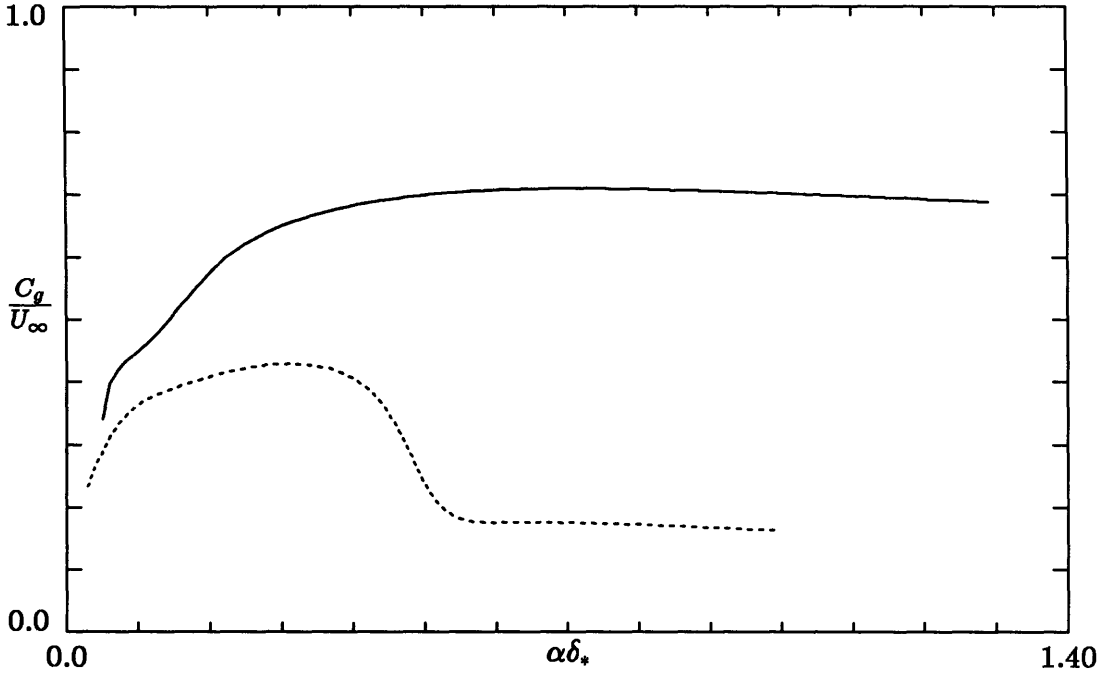

Figure 4.12: Group velocity $C_g(\alpha)$ for the perturbed velocity profile (Solid line) and Blasius profile (Dotted line).

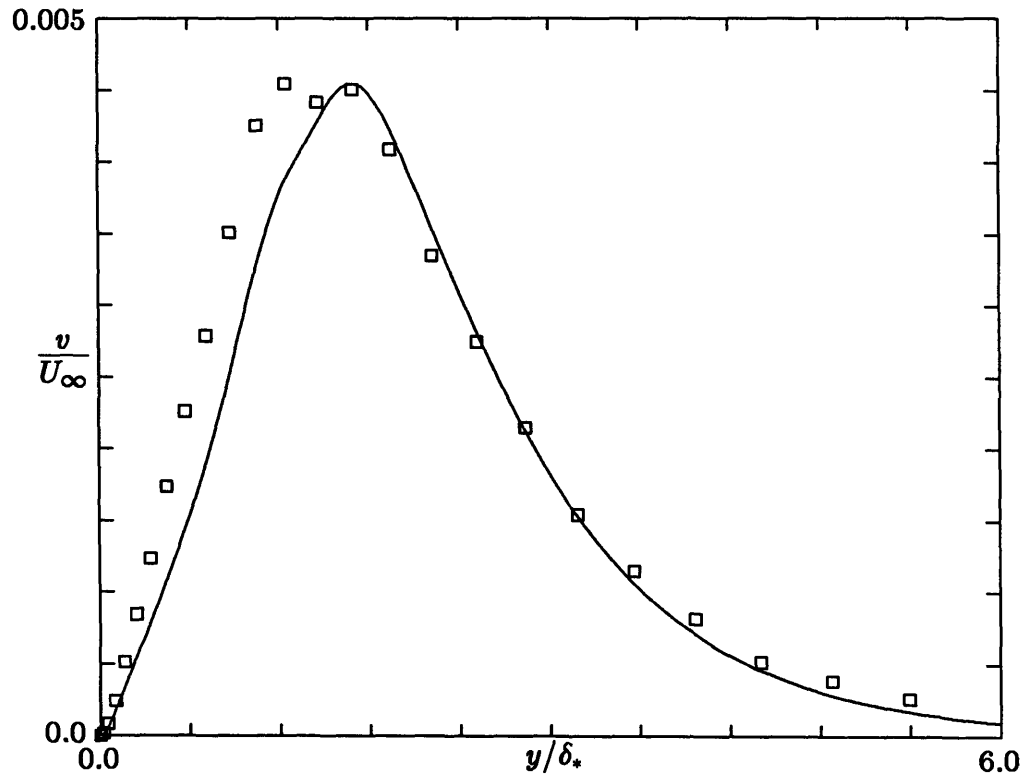

Figure 4.13: Vertical distribution of wave amplitude. Data points represent the amplitude distribution of v through the boundary layer from the full simulation data at $t = 62$. Solid line represents the eigenfunction based on linear stability calculations of distorted profile at $t = 62$.

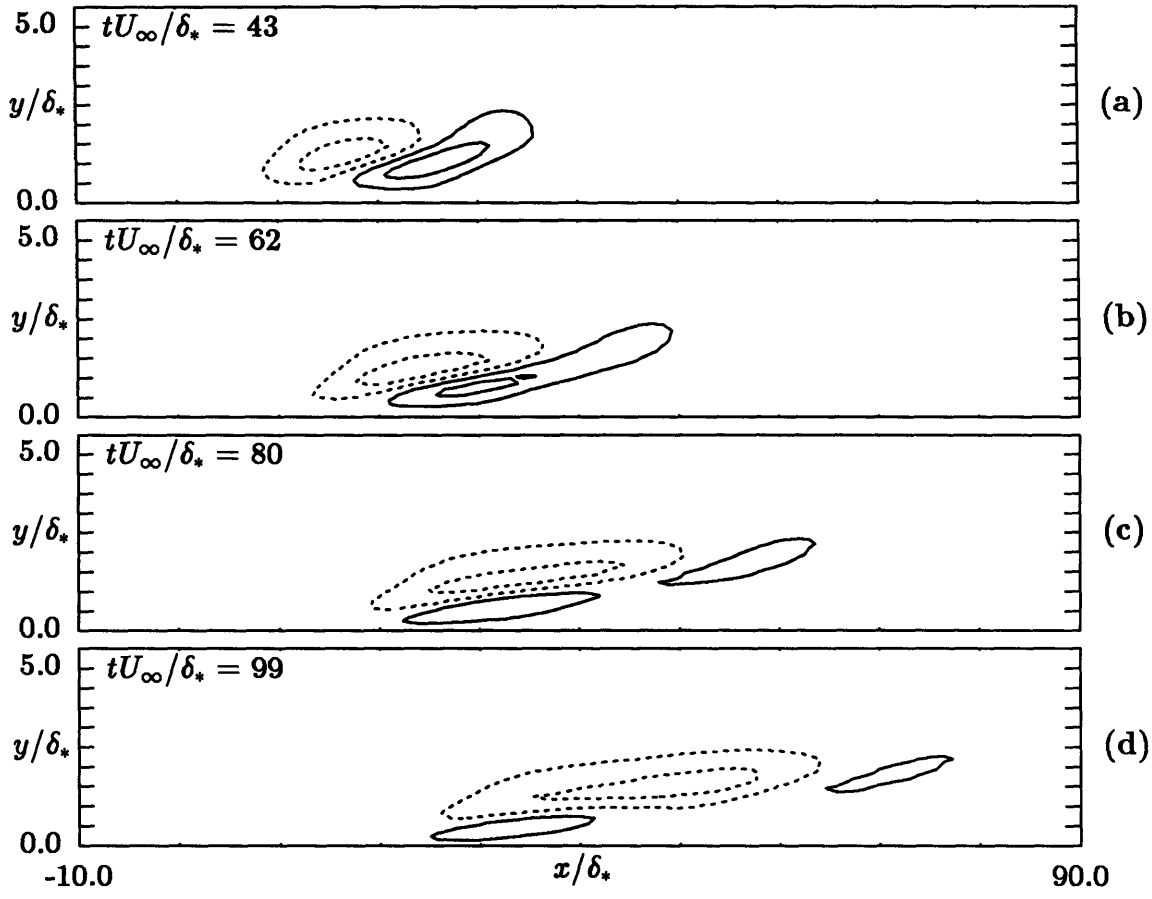

Figure 4.14: Full simulation. Contours of streamwise perturbation velocity at $z = 0.0$. *Negative* disturbance. Contour levels: $0.02U_\infty$. Solid lines represent positive contours, dotted lines represent negative contours.

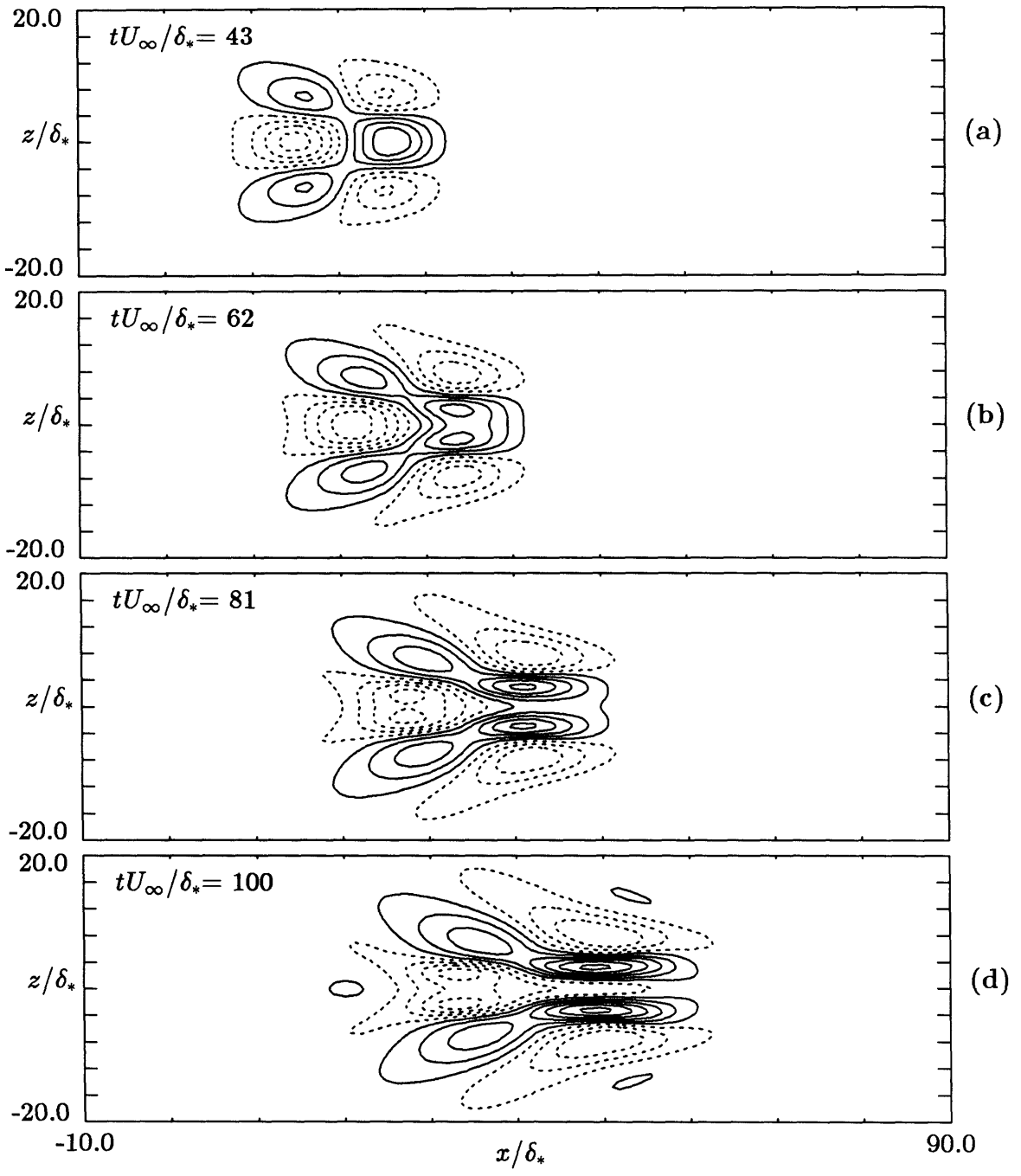

Figure 4.15: Full simulation. Contours of streamwise perturbation velocity at $y/\delta_* = 0.5$. *Negative* disturbance. Contour levels: $0.02U_\infty$. Solid lines represent positive contours, dotted lines represent negative contours.

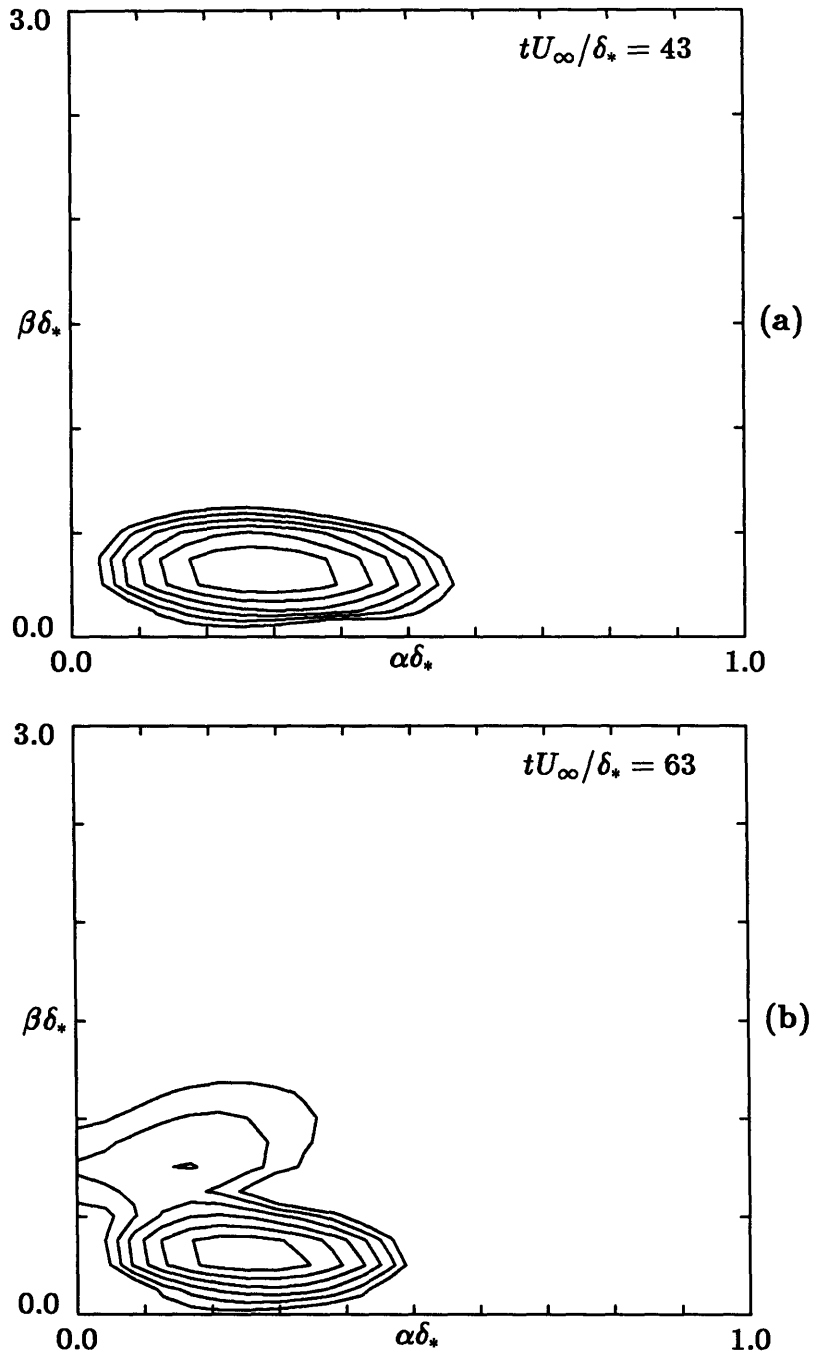

Figure 4.16: Full simulation. Power spectra of v component at $y/\delta_* = 1.05$. *Negative* disturbance. Logarithmic contour levels.

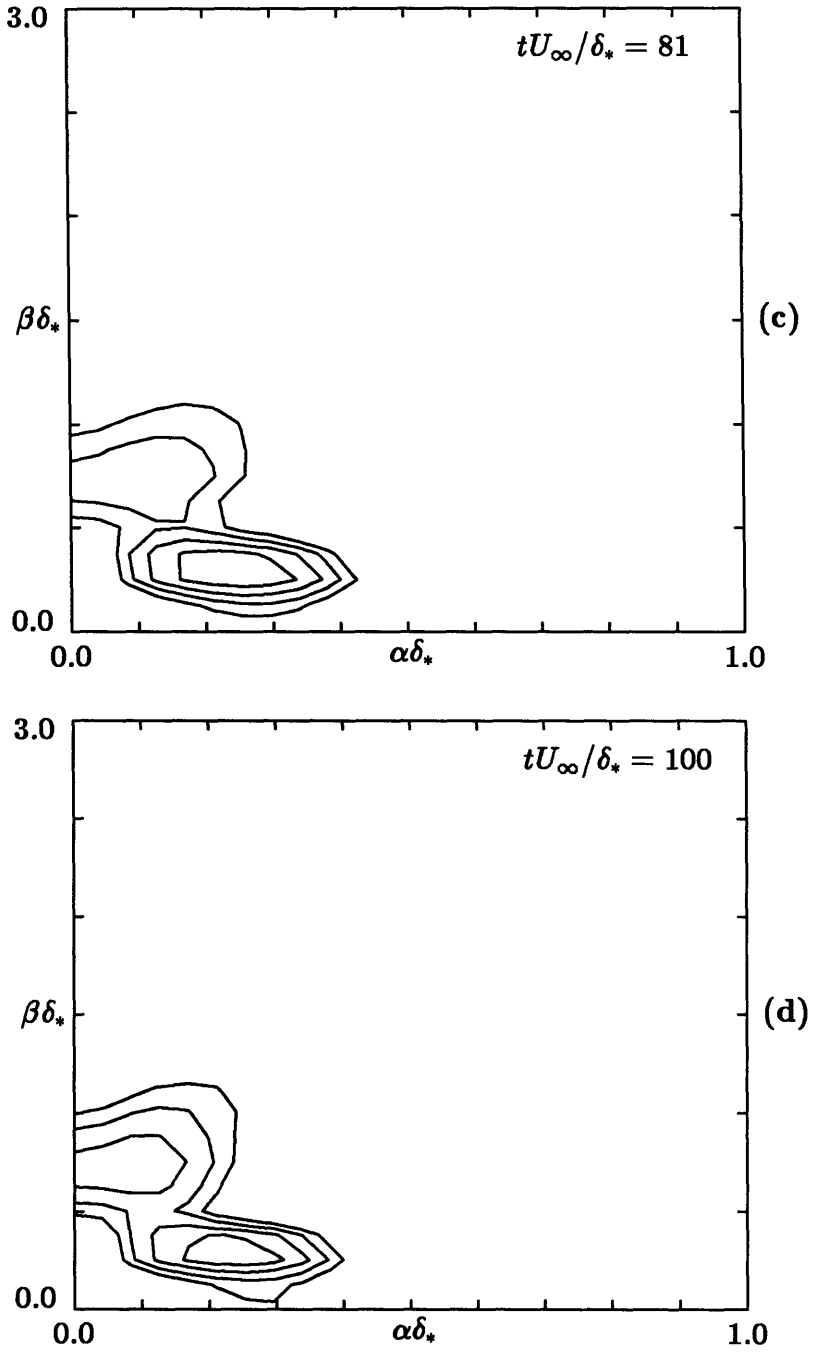

Figure 4.16: (Continued). Full simulation. Power spectra of v component at $y/\delta_* = 1.05$. *Negative* disturbance. Logarithmic contour levels.

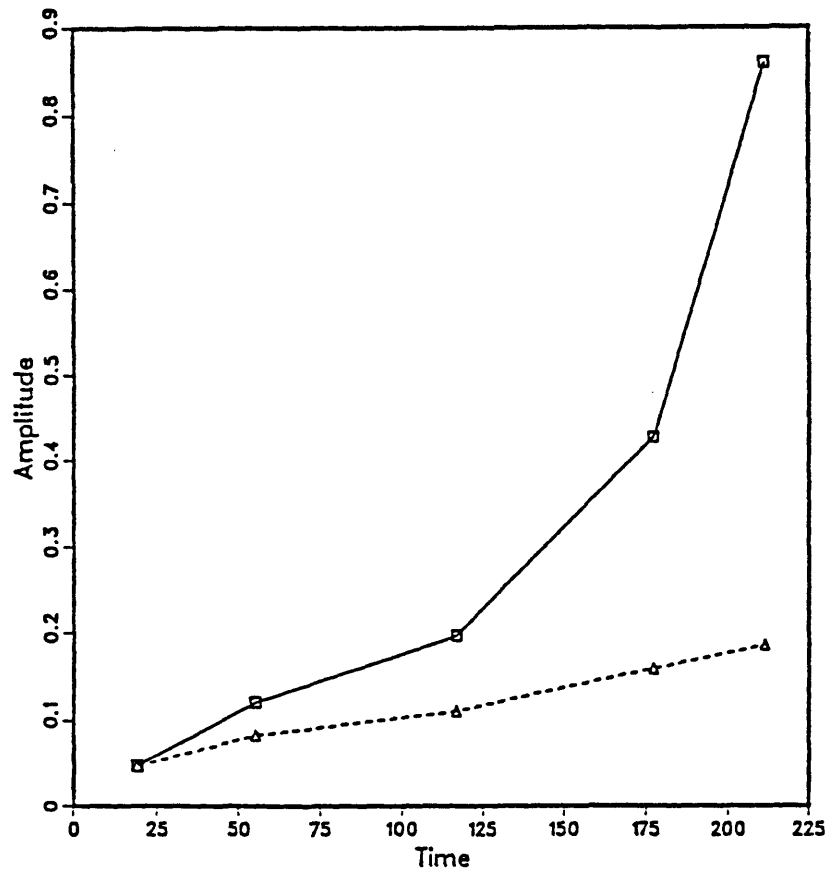

Figure 4.17: Full simulation. Amplitude of peak-to-peak u for both positive disturbance (solid line) and negative disturbance (dotted line).

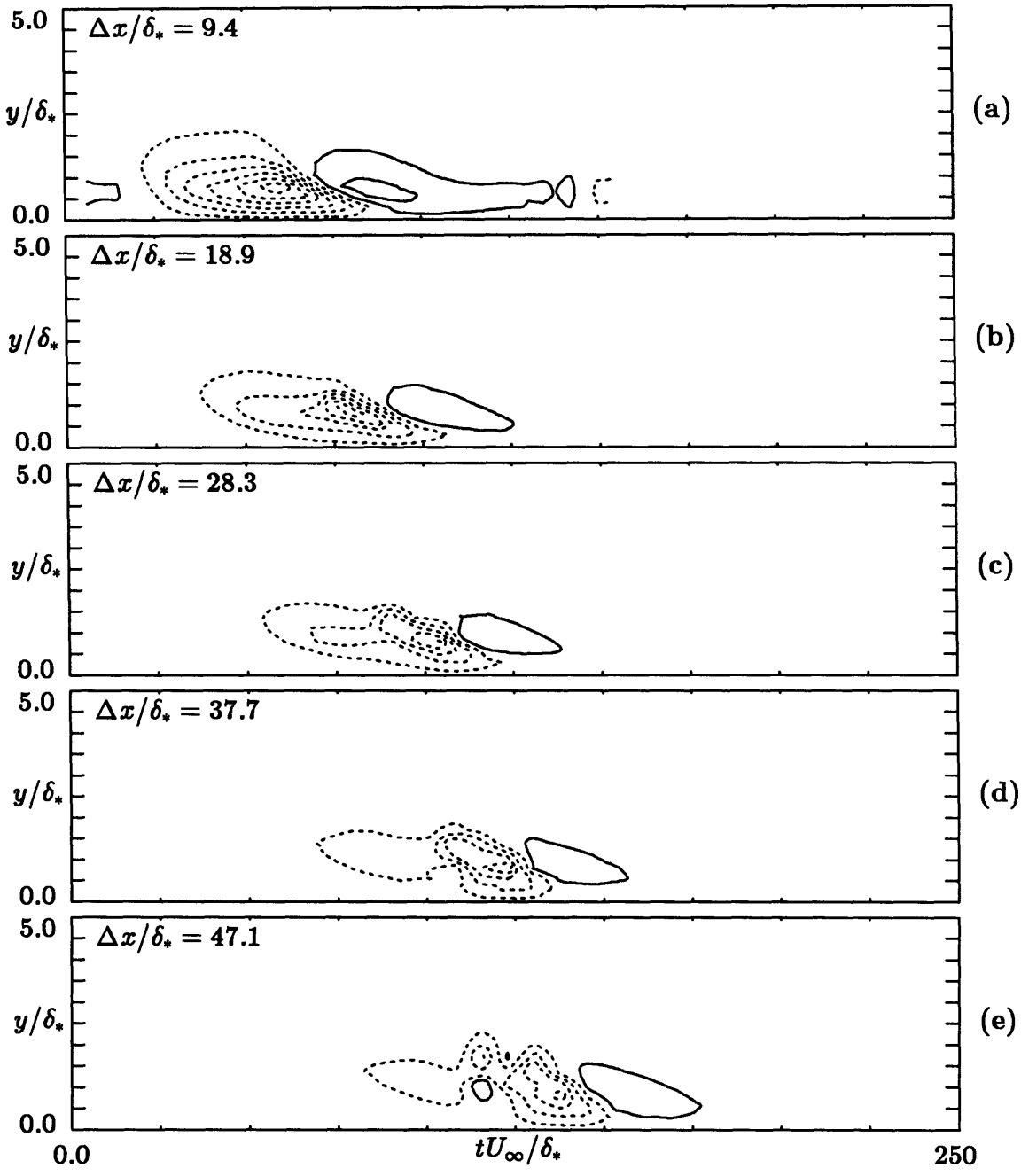

Figure 4.18: Experimental results. Contours of streamwise perturbation velocity for strong disturbance at $z = 0.0$. Contour levels: $0.03U_\infty$. Solid lines represent positive contours, dotted lines represent negative contours.

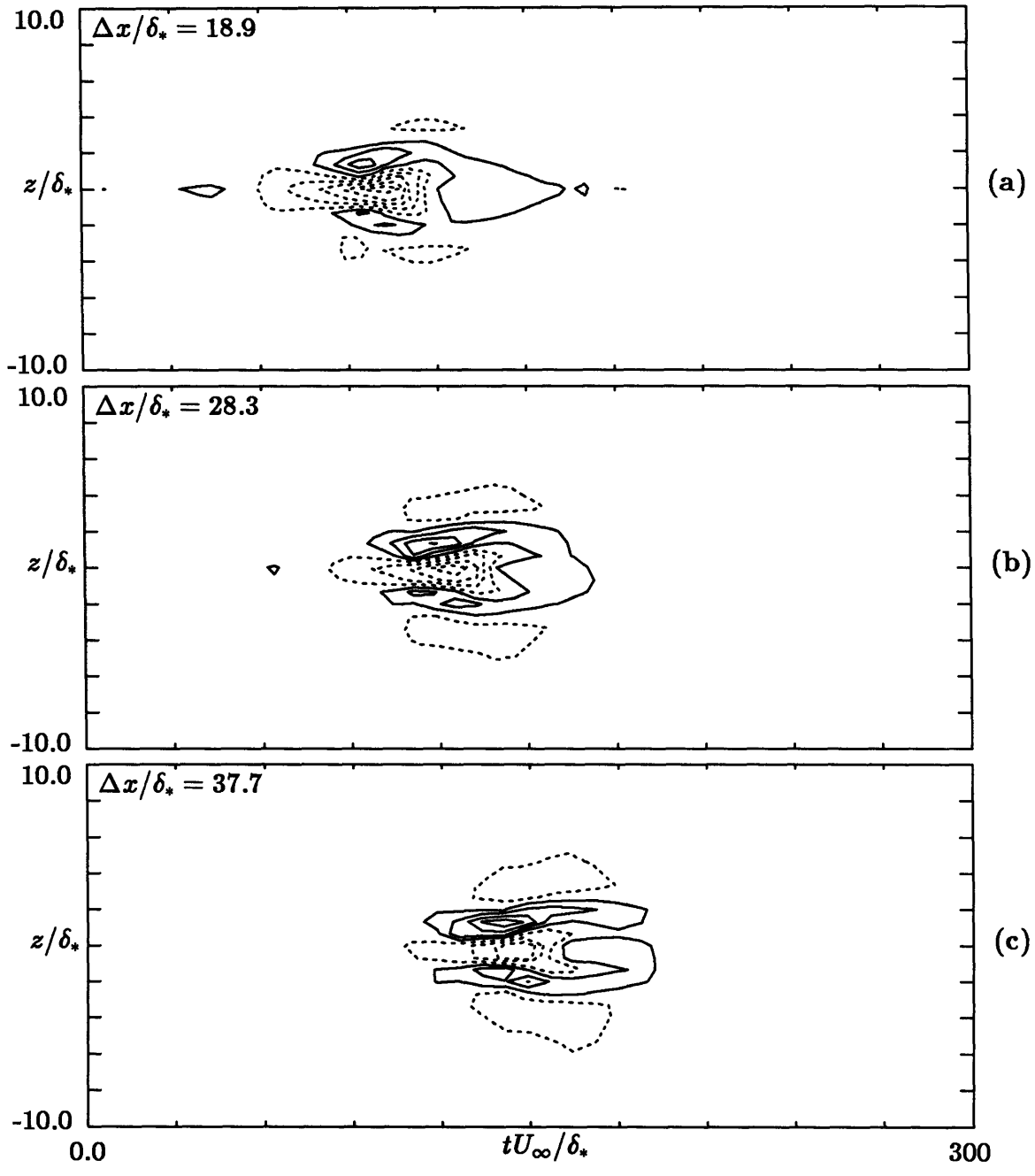

Figure 4.19: Experimental results. Contours of streamwise perturbation velocity for strong disturbance at $y/\delta_* = 0.5$. Contour levels: $0.03U_\infty$. Solid lines represent positive contours, dotted lines represent negative contours.

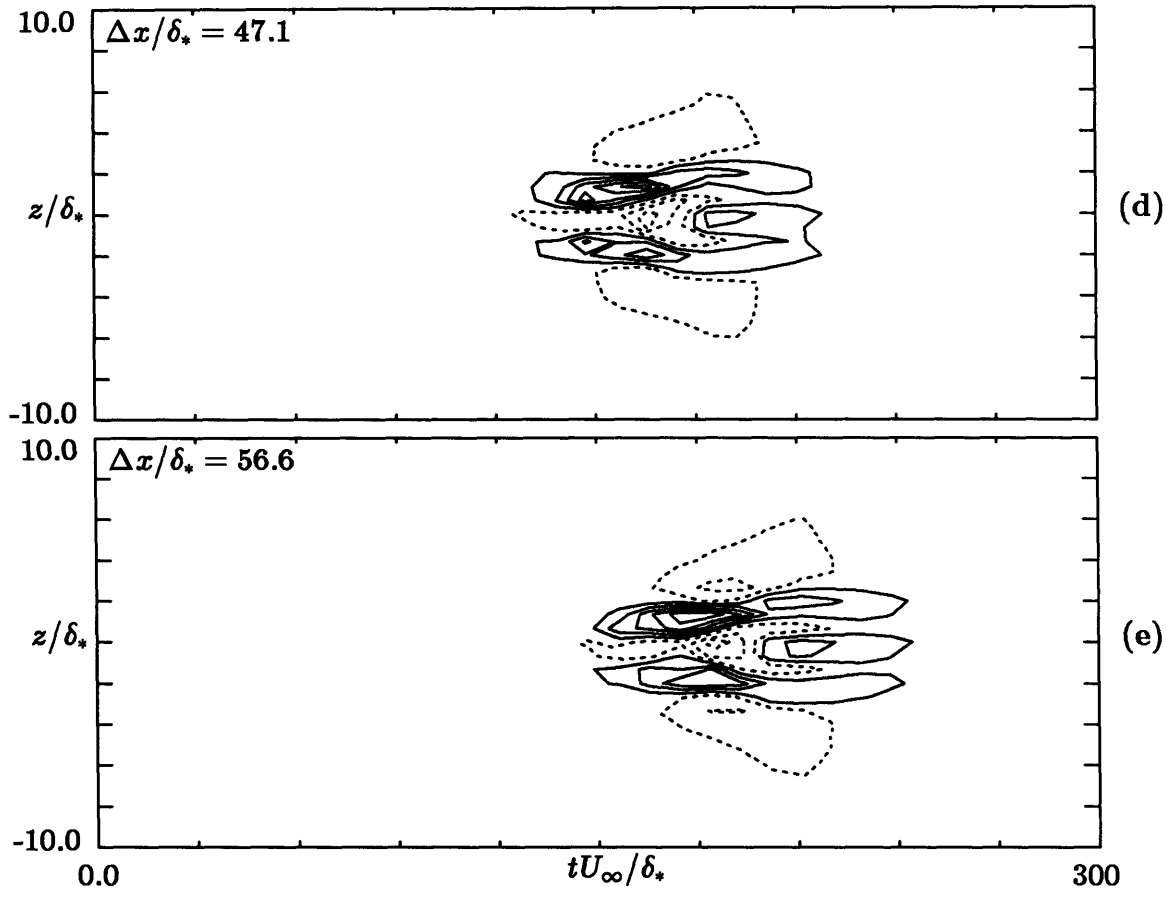

Figure 4.19: (Continued). Experimental results. Contours of streamwise perturbation velocity for strong disturbance at $y/\delta_* = 0.5$. Contour levels: $0.03U_\infty$. Solid lines represent positive contours, dotted lines represent negative contours.

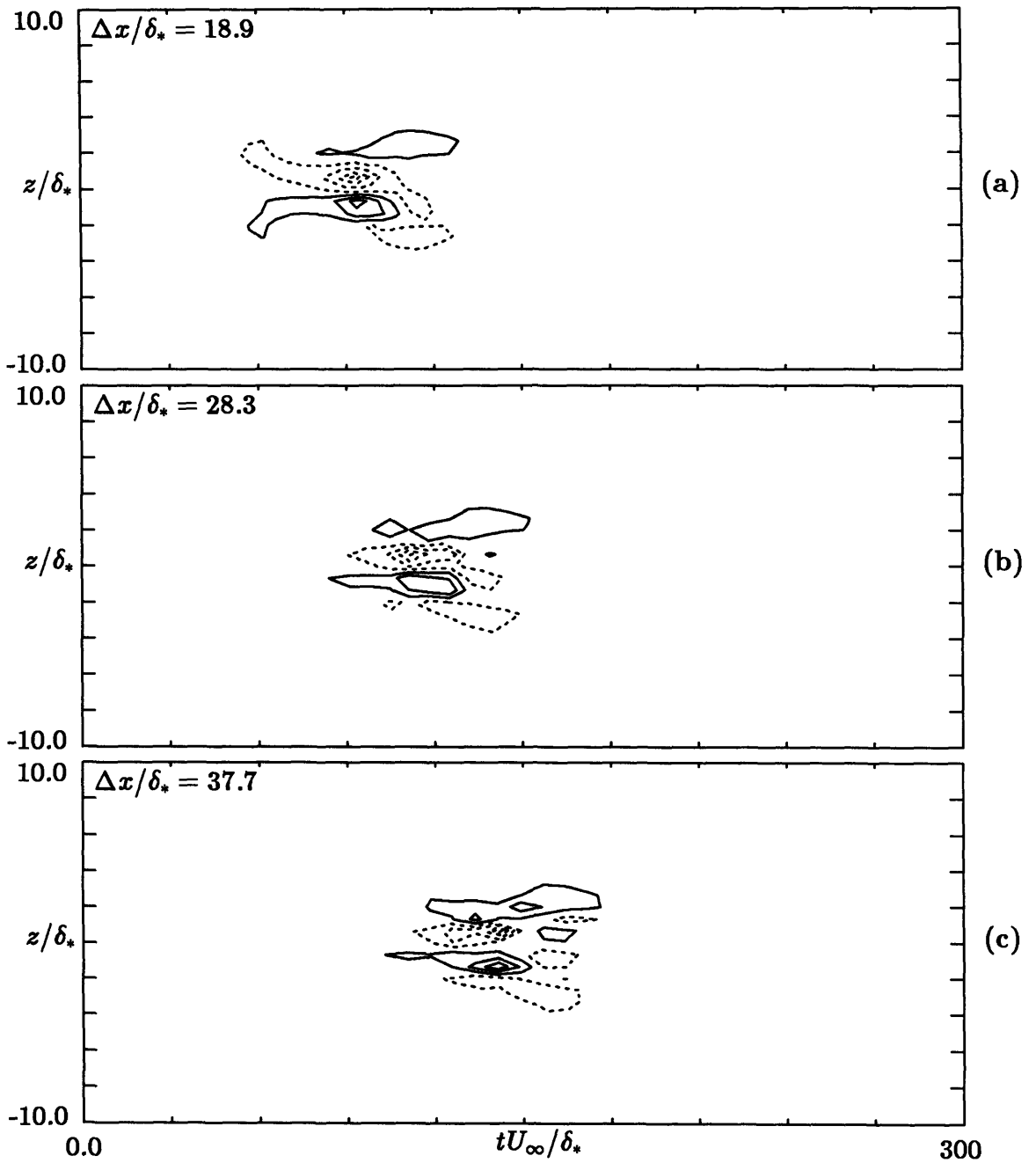

Figure 4.20: Experimental results. Contours of spanwise perturbations velocity for strong disturbance at $y/\delta_* = 0.5$. Contour levels: $0.02U_\infty$. Solid lines represent positive contours, dotted lines represent negative contours.

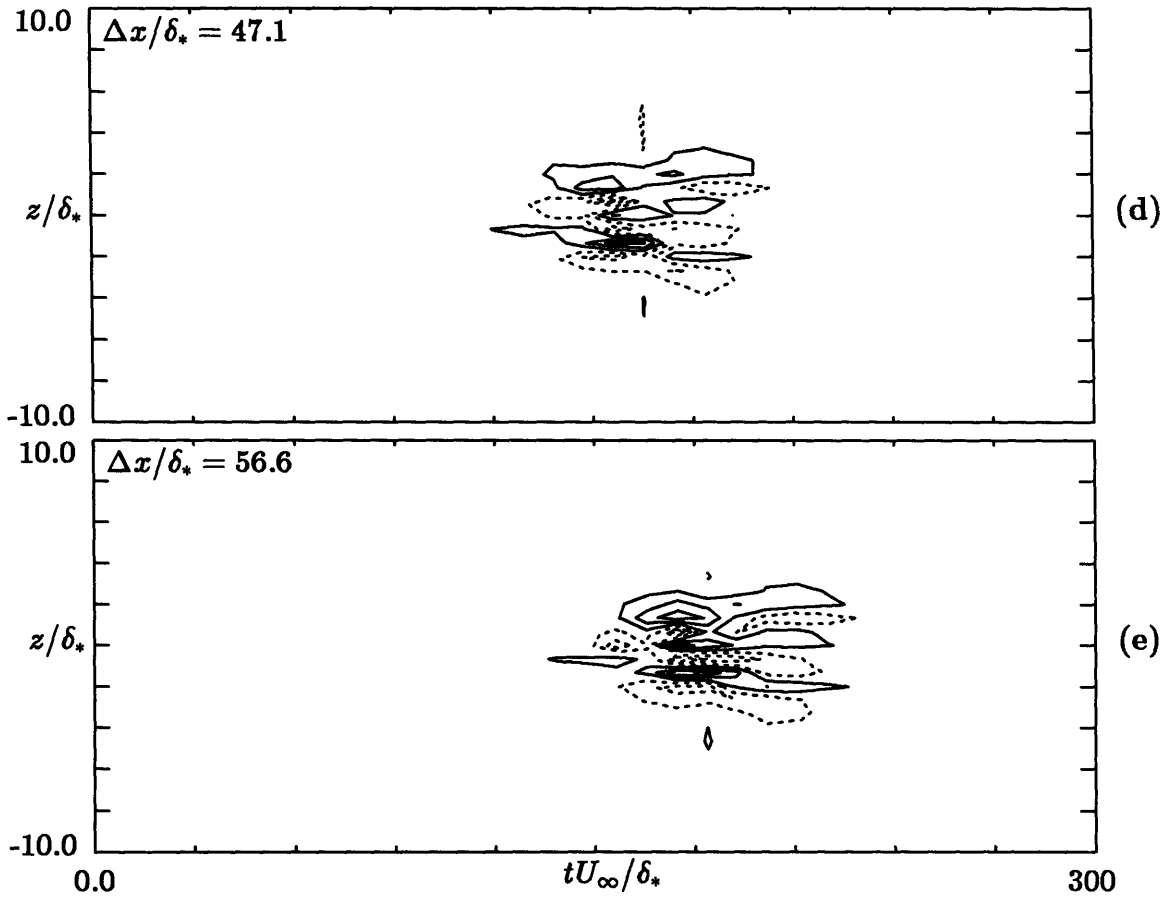

Figure 4.20: (Continued). Experimental results. Contours of spanwise perturbations velocity for strong disturbance at $y/\delta_* = 0.5$. Contour levels: $0.02U_\infty$. Solid lines represent positive contours, dotted lines represent negative contours.

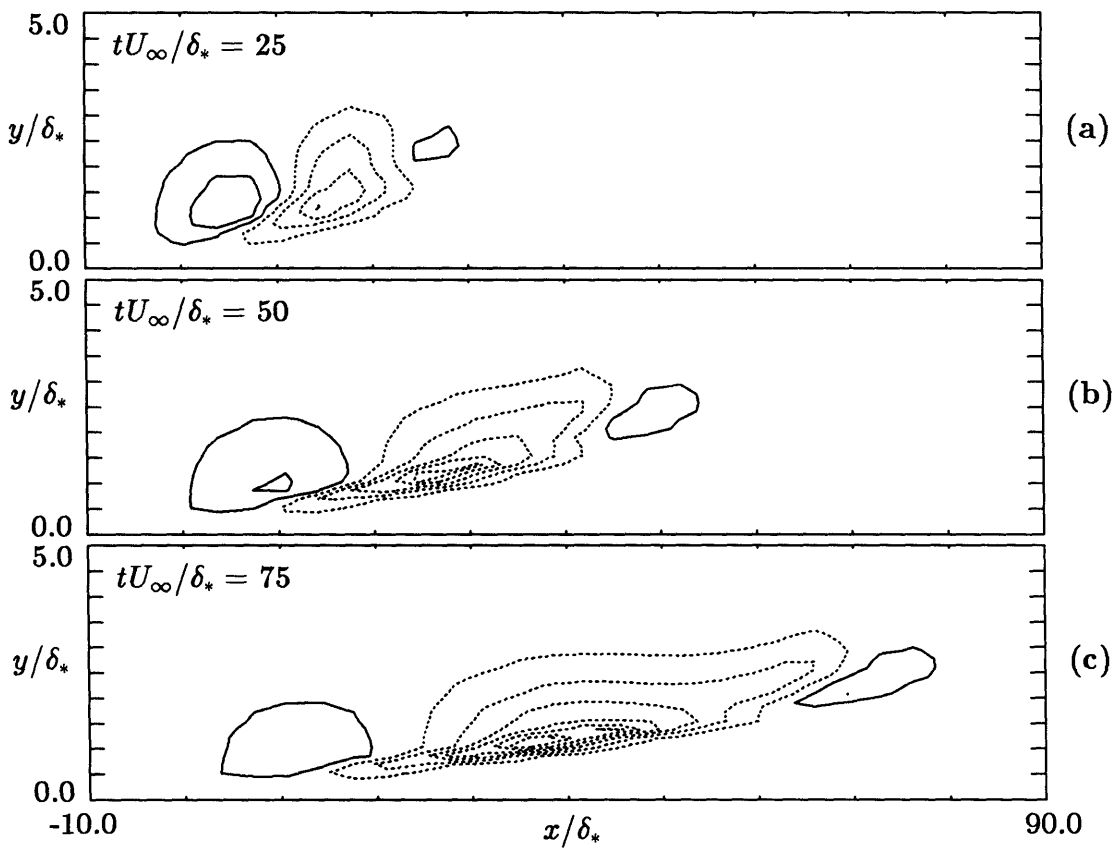

Figure 4.21: Flat-Eddy equations. Contours of streamwise perturbation velocity for strong disturbance at $z = 0.0$. Contour levels: $0.01U_\infty$. Solid lines represent positive contours, dotted lines represent negative contours.

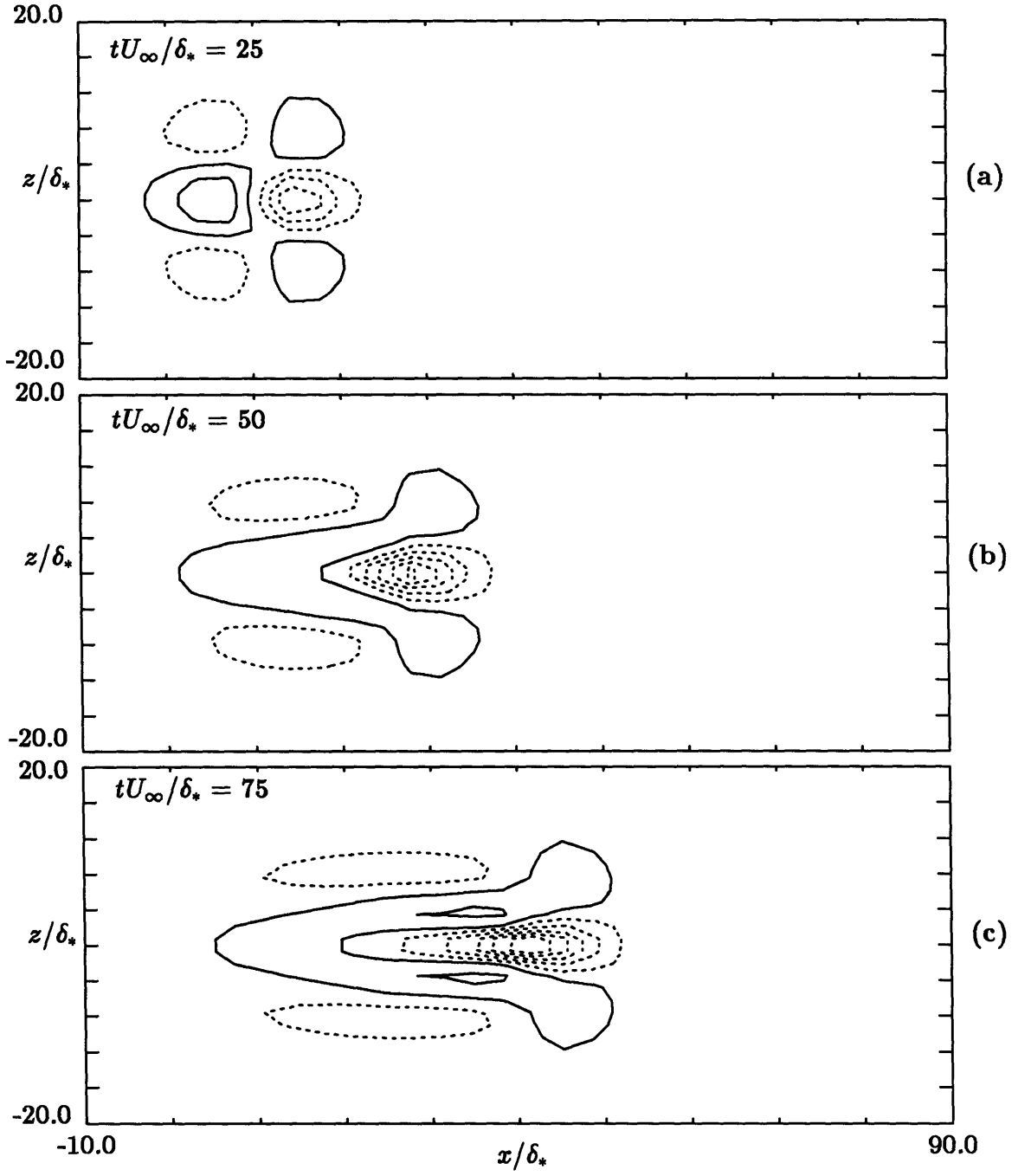

Figure 4.22: Flat-Eddy equations. Contours of streamwise perturbation velocity for strong disturbance at $y/\delta_* = 1.0$. Contour levels: $0.01U_\infty$. Solid lines represent positive contours, dotted lines represent negative contours.

Chapter 5

Comparisons with Turbulent Flows

At several stages throughout the discussion of the evolution of localized disturbances thus far, we have commented that some features of the results for this transitional flow are reminiscent what are found in fully turbulent flows. The object of this chapter is to briefly discuss some of these similarities and to argue that the structures seen in the transitional boundary layer flows are essentially the same structures that are obtained from conditional sampling of fully turbulent wall-bounded flow. Some of the similarities between transitional and turbulent flows have been pointed out by Blackwelder[9] who examined the comparable roles of streamwise vortices in turbulent flows and in transitional flows, including flows over concave surfaces. In such a flow, streamwise Görtler vortices develop creating inflectional shear layers which lead to transition and turbulence. These mechanisms, Blackwelder argued, are very similar to those associated with the streamwise vortices seen in fully turbulent flows.

A second, somewhat different comparison between laminar and turbulent flows was discussed by Acarlar and Smith[1,2], who generated hairpin vortices in a laminar boundary layer and also injected low-speed fluid into the wall region of a laminar boundary layer which subsequently developed into hairpin vortices. These laminar simulations acted as as models of some of the pheonomena that have been observed in turbulent wall flows. The idea behind their work was that the hairpin vortices generated in a

laminar flow would still contain all of the the relevant physics that one would find in a turbulent flow, but the observation of the dynamics is made much simpler by the clean environment offered by a laminar boundary layer. This is also the idea behind the application of the present results to the turbulent flow case. As we shall show, many of the features that are observed in a conditionally-averaged turbulent flow are also reproduced in the laminar flow results.

The friction velocity (u_τ) for a Blasius boundary layer can be written as:

$$u_\tau = \frac{0.756 U_\infty}{\sqrt{Re_{\delta_*}}} \tag{5.1}$$

Similarly, the displacement thickness, δ_* can be converted into viscous wall units (denoted by a '+' superscript):

$$\delta_*^+ = 0.756\sqrt{Re_{\delta_*}} \tag{5.2}$$

With these definitions, we can rescale the laminar flow in viscous units and look at the laminar structure in the same terms as if it were a turbulent flow. Since the laminar disturbance examined was at $Re_{\delta_*} = 945$, the displacement thickness, in viscous units is about 23 and thus the entire boundary layer is only approximately 70 viscous units thick. This height corresponds approximately to the height of the wall and buffer regions in a turbulent flow.

It has been known for some time now that shear-layer structures in the wall region of a turbulent flow are very important in the production of turbulence. Blackwelder and Kaplan[8] developed the VITA technique (Variable Interval Time Averaging) for detecting characteristic events in a turbulent boundary layer. Their results indicated that the Reynolds stress associated with VITA events was an order of magnitude larger than the conventionally averaged Reynolds stress in the flow. The spatial structure of

a VITA event was measured by Johansson, Alfredsson and Eckelmann[33] who used two hot-wire probes in a low-Reynolds number turbulent oil channel to map out the shear layer structure in the $x-y$ plane (they used a Taylor hypothesis to transform the temporal record to a spatial one). This structure, reproduced in Figure 5.1 is plotted as contours of local coherent perturbation velocity, normalized by the local fluctuation velocity: $\tilde{u}'/\sqrt{\overline{u'^2}}(y)$. The shear layer is characterized by an accelerated region (with an accompanying downward v component, and thus called the 'sweep' side in the turbulence literature) and a stronger 'ejection' side (the downstream part of the structure, where u is negative and v' is positive). The inclination of the shear layer was measured to be 7° near the wall and 20° in the buffer region.

The numerical simulations of fully turbulent channel flow by Moin and Kim [54,55,39] have allowed researchers to look in some detail at the three-dimensional structure of these shear layers. Kim[38] used a VISA (Variable Interval Space Averaging) detection scheme to conditionally sample the near wall region of a numerically simulated flow field, and found that the structure associated with a sharp deceleration of u with x (corresponding to the positive $\partial u/\partial t$ for a VITA event) consisted of two pairs of counter-rotating streamwise vortices - one associated with the upward motion of fluid (the ejection side) and the other, positioned directly upstream of the first, was associated with the downward motion of fluid (the sweep side). This structure has many similarities with the kind of disturbance that has been studied in this thesis. Recently a more detailed investigation was carried out by Johansson, Alfredsson and Kim[34] at the NASA/Stanford Center for Turbulence Research, and much of the following discussion will consist of a comparison of their results, from the turbulent channel numerical data base, with the present results from the laminar boundary layer.

5.1 Velocity Signals

Figure 5.2 shows the streamwise velocity signal obtained from two different sources. The first is the laminar flow simulation at $tU_\infty/\delta_* = 62$ replotted in viscous units, while the second plot is the signal found from conditional averaging of the numerically simulated turbulent flow field. Both structures show the presence of the inclined shear layer with the stronger perturbations on the downstream side of the disturbance where the velocity is lower than the local mean. The comparison between the spanwise structures of the conditional averages and of the laminar simulation is shown in Figure 5.3 (for the u velocities) and Figure 5.4 (for the v velocities).

In accordance with the structure seen in the laminar simulation, the main structure educed from the turbulent flow consists of an accelerated region on the upstream side with the decelerated region on the downstream side. The v perturbation indicates that the ejection side, where v is positive, is stronger than the sweep side, which is further upstream. This is also reproduced in the laminar simulation. The side lobes on either side of the main perturbations are also seen in the turbulent conditional averages. The consequence of the stronger downstream perturbations is that the Reynolds stress $(-uv)$ is considerably stronger on the ejection side than on the sweep side. This is true for both the turbulent conditional averages and the laminar disturbance simulations (Figure 5.5).

Both the results of Johansson, Alfredsson and Kim[34] and Johansson, Alfredsson and Eckelmann[33] agree that the structures remain confined to the near-wall region of the flow. ($y^+ < 60$). This is also consistent with the laminar flow result, although the confinement of the laminar disturbance is due to the fact that the structure is restricted to the boundary layer which itself is only 70 viscous units in height. In a turbulent

flow, the mean shear extends several hundred or even thousand viscous units. However, there is a sharp drop in the strength of the mean shear from the linear region to the logarithmic region, and this change in the shear may be the factor which sets the vertical scale for the shear layer structure in the turbulent flow.

5.2 Secondary Instabilities

One aspect of the laminar calculations that was important in the breakdown of the localized disturbance was the development of a secondary instability on the inflectional shear layer created by the lift-up effect. The experimental data of Johansson, Alfredsson and Eckelmann[33] (reproduced in Figure 5.6) does indicate some waves in the v signal, and they reported that similar waves have also been observed in the v signal in their earlier water channel data. The waves have a frequency of about 5.3 viscous time units, which translates to a wavelength of about 65 viscous length units. (assuming a propagation speed comparable to the shear layer's speed of 12 u_τ). Schewe[64] measured wall-pressure fluctuations simultaneously at three streamwise locations. He found, by visual analysis of the pressure signals, that pressure structures with high amplitude had the shape of "short wavetrains or pulses" and he measured the frequency and wavelength of these wavetrains to be $\omega^+ = 0.52$ and $\lambda^+ = 145$. Her[28] measured the wall pressure and the associated u and v signals at $y^+ = 15$. He also found the presence of this "wavy structure" in both the wall-pressure and the v signals although not in the u signal. The characteristic frequency of the wave structure was found to be $\omega^+ = 0.5$, which yields a wavelength of $\lambda^+ = 145$ assuming an advection speed of $12u_\tau$, in good agreement with Schewe. Recent work by Haritonidis, Gresko and Breuer[25] has investigated the 'wave' motion associated with VITA events, and their results indicate that while there is a

broad range of wave frequencies associated with the turbulence generating events, there is a clustering around $\omega^+ = 0.5$ In the present results, the wavelength of the secondary instability in the laminar simulation is about 140 l^+ which agrees extremely well with the results of Her and of Schewe, although it is roughly twice the wavelength seen in the oil channel data. The results of Johansson, Alfredsson and Kim from the numerically simulated turbulent flow do not address the issue of waves on the shear layer and the reason for this may be because the streamwise grid-spacing of the numerical simulation is only $17.67x^+$ which would make the resolution of the waves, if they are present, somewhat marginal.

Despite the discrepancies between the laminar simulations and the conditional averages from the turbulent flows it seems probable that the same phenomenon is being observed in both cases. We should not expect to match the structures too closely since the flow conditions, velocity profiles, etc. are very different, However, the qualitative similarities between the the two flows are nevertheless significant. One interesting observation concerning the turbulent results is that for the 'wave' observed in Johansson, Alfredsson and Eckelmann's results to survive the conditional averaging process, the wave crests must remain at a fixed position relative to the rest of the structure. If the phase speed of the waves was different from the propagation speed of the shear layer, the relative crest location would be random, and the waves would be averaged out by the sampling procedure. The laminar calculations do indicate, however, that the phase speed is the same as the structure's propagation speed, and this may be further confirmation that the two observations relate to the same physical process.

5.3 Pressure and Velocity Signals

It was mentioned in Chapter 4 that the peaks in the pressure signal in the laminar disturbance correspond well with the streamwise gradients of v. This is in agreement with the results of Johansson, Her and Haritonidis[35] in which they established a strong link between high peaks in the wall-pressure signal and shear-layer structures in the corresponding flow above the wall. The wall-pressure signal can be calculated by evaluating a Poisson integral over the entire flow field with the 'source' term (q) given by:

$$q = 2\frac{\partial U_i}{\partial x_j}\frac{\partial u_j}{\partial x_i} + \frac{\partial^2(u_i u_j - \overline{u_i u_j})}{\partial x_i \partial x_j} \tag{5.3}$$

The results of Johansson, Her and Haritonidis[35] showed that the pressure peaks scaled linearly with the velocity signals, indicating that the linear term which is the mean-shear interaction term, is the dominant term in q. This has since been confirmed by Johansson[31] who has analysed the numerically simulated turbulent channel flow at NASA Ames. This relationship between the pressure and the mean-shear interaction term is also confirmed in the laminar disturbance calculations presented here. Figure 5.7 plots the wall-pressure signal at the centerline of the disturbance, $z^+ = 0.0$. In addition, the corresponding streamwise and vertical velocities at $y^+ = 15$ are plotted. The correspondence between the shear in v and the peaks in p is very good, and the association between the pressure peak and the shear layer is in good agreement with the results of Johansson, Her and Haritonidis[35]. The recent measurements by Haritonidis, et al.[25] also confirm that the wall pressure and the vertical velocity at $y^+ = 15$ are related to each other in a linear fashion for both high pressure-peak events ($p > 2.5p_{rms}$) and accelerating VITA-on-u events ($k > 1$) (See Figure 5.8)

5.4 Positive and Negative events

In their investigation of turbulent channel flow, Alfredsson and Johansson[32] noted that the frequency of positive VITA events (shear layer structures) was considerably higher than the frequency of negative VITA events. In light of the present results we can suggest a possible explanation for this. In Chapter 4, we compared the growth rates of the positive disturbances with the negative disturbances, and it was found that the positive disturbances grew at a much faster rate than their negative counterparts. It may be that the higher growth rates of the positive events means that they dominate in the flow field more quickly, are less susceptible to the background turbulent fluctuations and thus are observed more frequently in the turbulent flow.

5.5 Summary

One cannot claim that every aspect of the shear layer structure in the turbulent flow has been accurately modeled in the laminar flow. For example, the propagation speed of the disturbances in the turbulent flow has been estimated[34] at 12 u_τ, whereas the average propagation speed of the laminar disturbance was found to be about $0.4U_\infty$ corresponding to about $16u_\tau$ in viscous units. Similarly, the time evolution of the turbulent VISA events described by Johansson, Alfredsson and Kim[34] did not follow the clean evolution exhibited in the laminar case, ending with the breakdown of the structure. Rather, the VISA event in the numerically simulated turbulent flow seemed to 'fade' away. However, as was mentioned above, a direct *quantitative* correspondence between a turbulent and a laminar flow is not a reasonable expectation. The correspondence between the shear-layer events obtained from fully turbulent data fields and the laminar

simulation of a localized disturbance does indicate that while the two flow fields are very different, the parallels between the two are quite convincing. The shear layer events in the turbulent flow do seem to have an organized structure which can be modeled with some qualitative accuracy in a laminar flow. It seems arguable, therefore, that the shear layer structures in the near wall region of the turbulent boundary layer are well-ordered disturbances, generated by the random fluctuations present in the turbulent flow, but once generated, they evolve, essentially, according to 'laminar' dynamics and are only influenced in a secondary manner by the turbulent background flow. The initial generation of these structures has been addressed by Landahl[45] who argued that a localized burst in Reynolds stress $-uv$ (from a previous breakdown) would produce a large scale disturbance with a sense of rotation opposite to that of the mean shear. This kind of disturbance is exactly the kind of initial conditions that have been used in these calculations. Once generated in this manner, the shear layer structure would evolve and break down, generating a new disturbance, and so on. While this is an idealized account of the mechanisms in the near wall region, these results do indicate that the mechanisms involved are quite fundamental ones. It is hoped that the availability of the numerical data bases for turbulent flows will allow more detailed investigations of these issues in the future. Johansson, Alfredsson and Kim[34] reported that the most common VISA structure was not symmetric about its detection point but in fact are strongly antisymmetric. A natural extension of this work would be to examine the evolution of structures that do not enforce the reflectional symmetry about the x-axis and determine whether or not their growth is enhanced by the lack of symmetry.

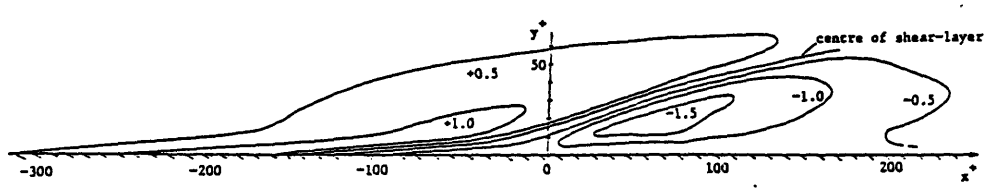

Figure 5.1: Contours of conditionally averaged streamwise perturbation velocity. Experimental Data from turbulent oil channel flow data; normalized by local u_{rms} Reproduced from Johansson, Alfredsson and Eckelmann (1987). Contour levels: 0.5. Solid lines represent positive contours, dotted lines represent negative contours.

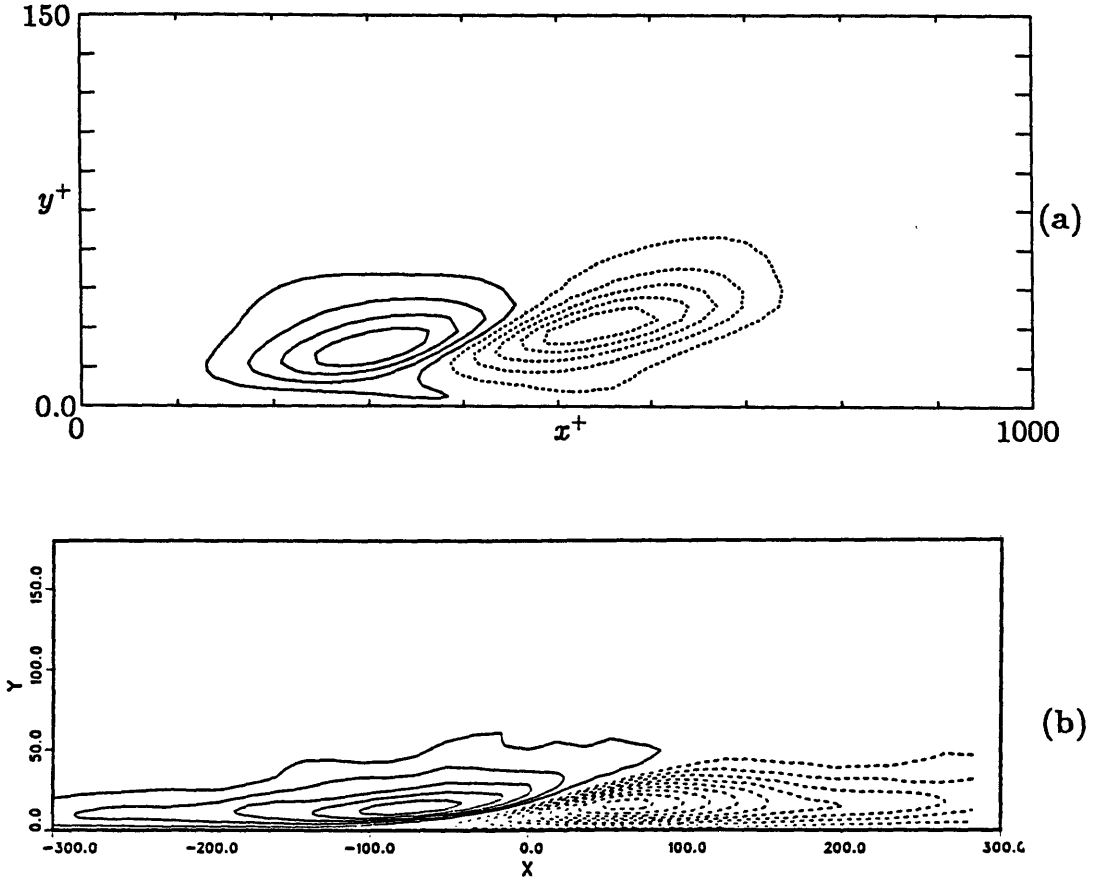

Figure 5.2: Contours of streamwise perturbation velocity at $z^+ = 0.0$. (a) Data from laminar simulation, plotted in viscous units. (b) Conditionally avereraged data from numerical simulation of turbulent channel flow. Reproduced from Johansson, Alfredsson and Kim (1987). Both plots are normalized by u_τ. Contour levels: 0.5. Solid lines represent positive contours, dotted lines represent negative contours.

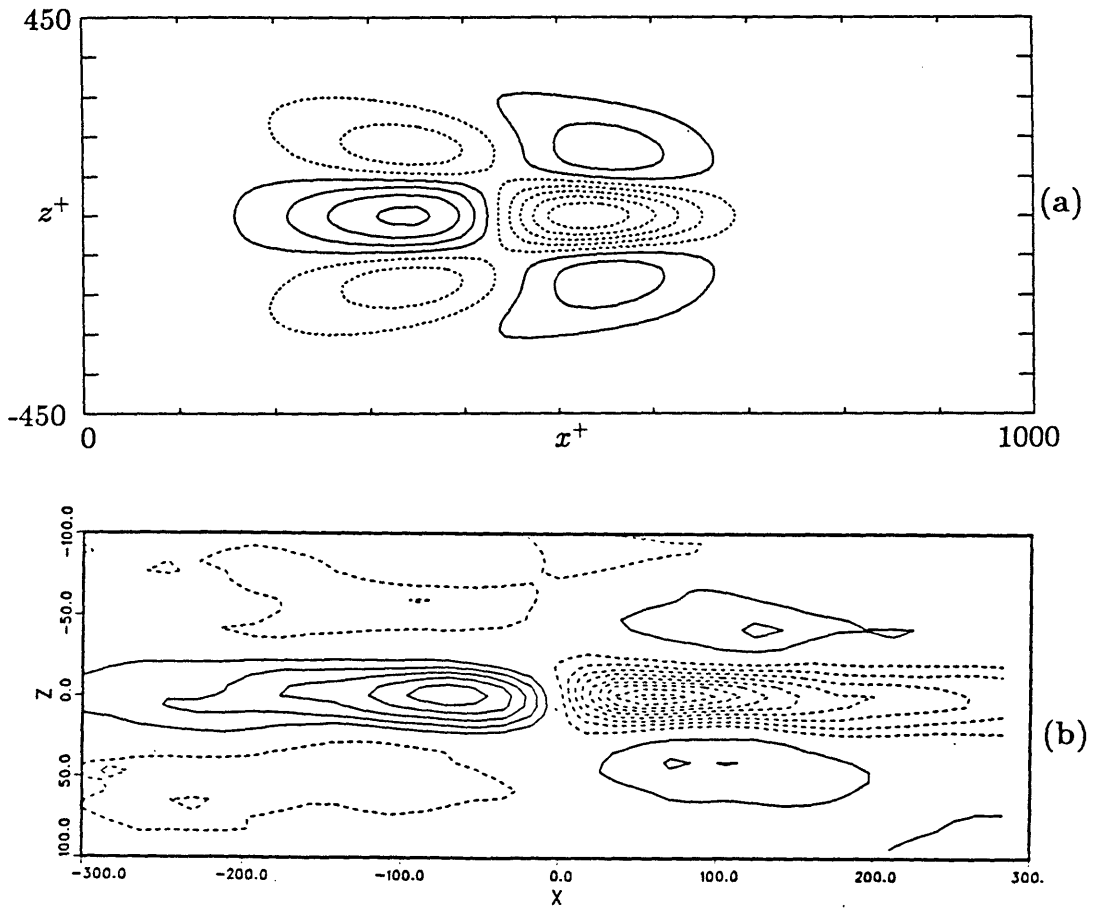

Figure 5.3: Contours of streamwise perturbation velocity at $y+ = 15$. (a) Data from laminar simulation, plotted in viscous units. (b) Conditionally avereraged data from numerical simulation of turbulent channel flow. Reproduced from Johansson, Alfredsson and Kim (1987). Both plots are normalized by u_τ. Contour levels: 0.5. Solid lines represent positive contours, dotted lines represent negative contours.

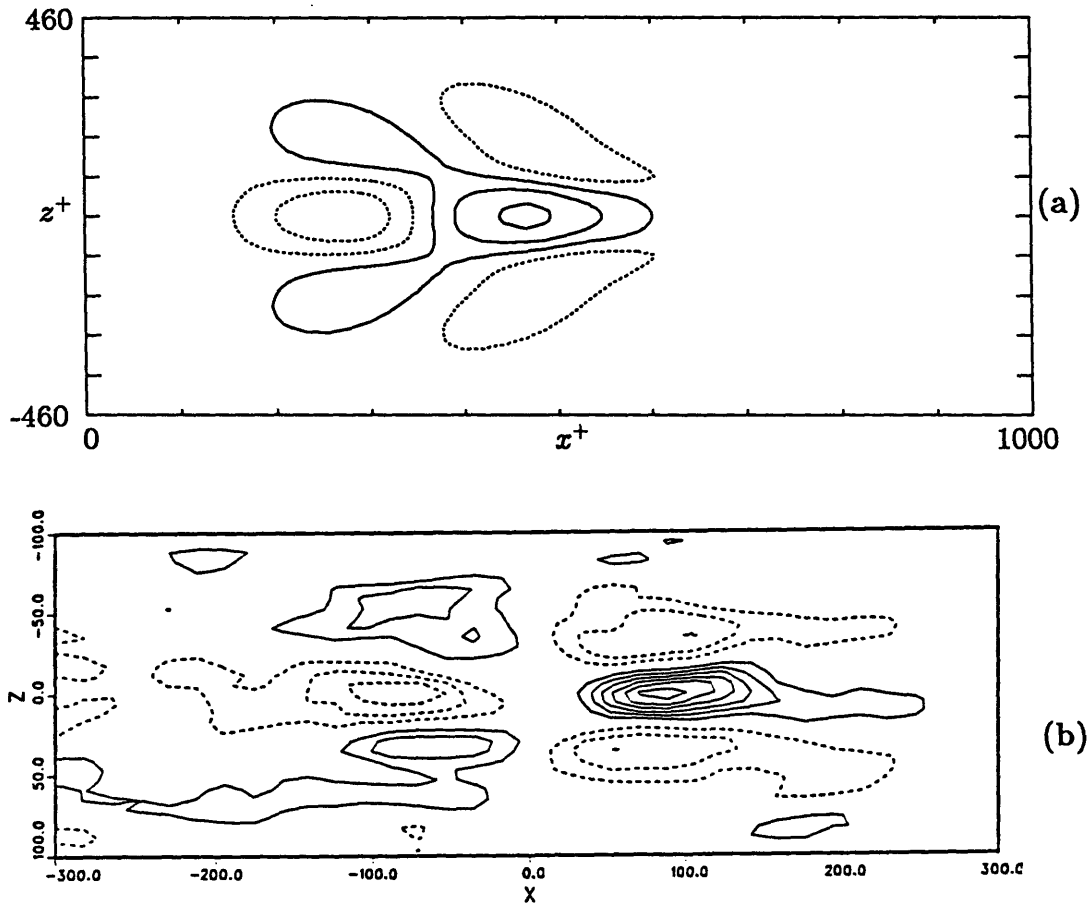

Figure 5.4: Contours of vertical perturbation velocity at $y^+ = 15$. (a) Data from laminar simulation, plotted in viscous units. (b) Conditionally avereraged data from numerical simulation of turbulent channel flow. Reproduced from Johansson, Alfredsson and Kim (1987). Both plots are normalized by u_τ. Contour levels: 0.1. Solid lines represent positive contours, dotted lines represent negative contours.

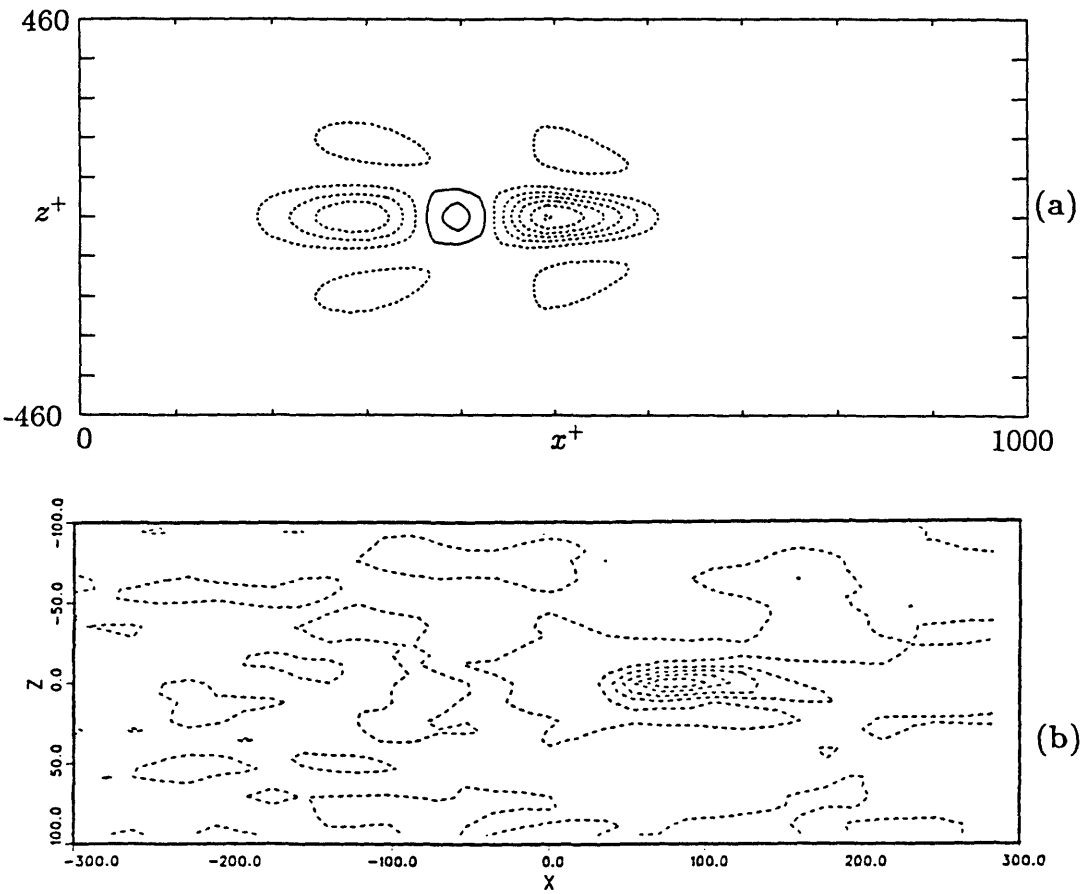

Figure 5.5: Contours of Reynolds stress at $y^+ = 15$. (a) Data from laminar simulation, plotted in viscous units. (b) Conditionally avereraged data from numerical simulation of turbulent channel flow. Reproduced from Johansson, Alfredsson and Kim (1987). Both plots are normalized by u_τ. Contour levels: 0.5. Solid lines represent positive contours, dotted lines represent negative contours.

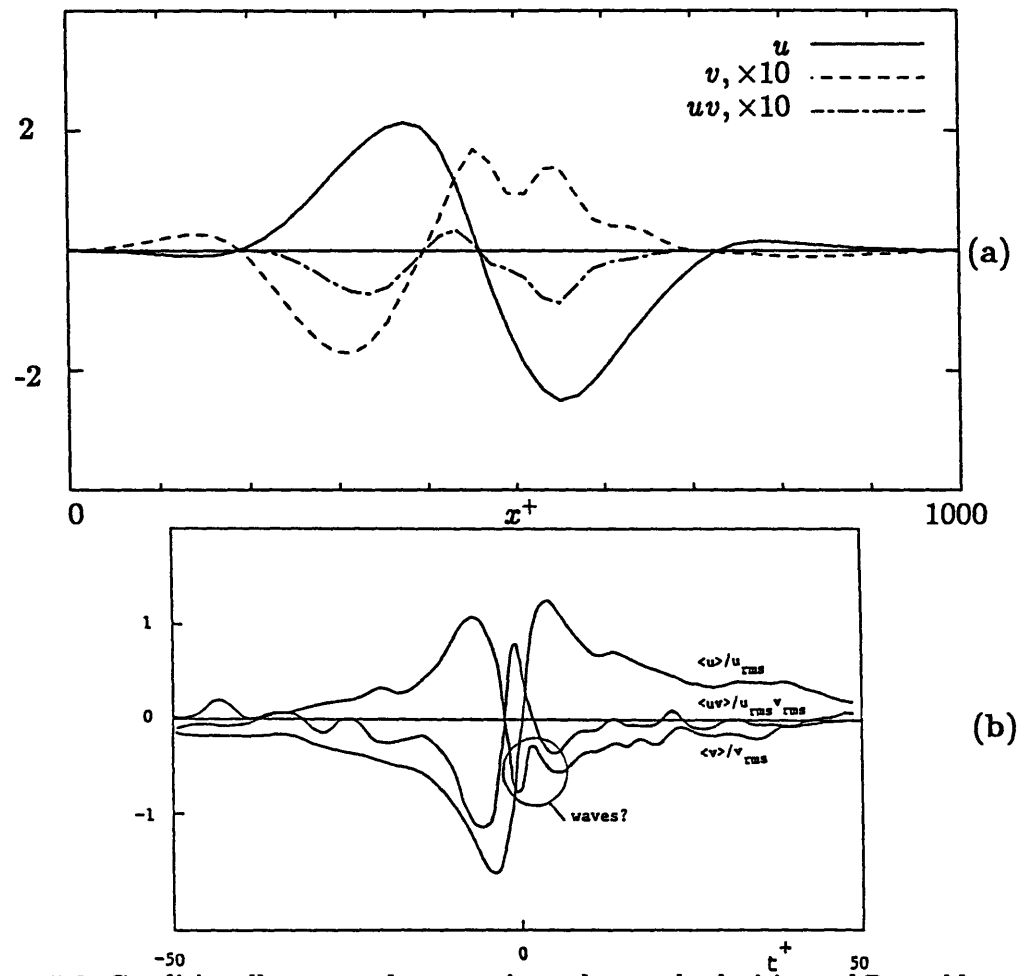

Figure 5.6: Conditionally averaged streamwise and normal velocities and Reynolds stress at $y^+ = 15$. (a) Data from laminar simulation, plotted in viscous units. (b) Conditionally avereraged data from turbulent oil channel. Reproduced from Johansson, Alfredsson and Eckelmann (1987). Both plots are normalized by u_τ.

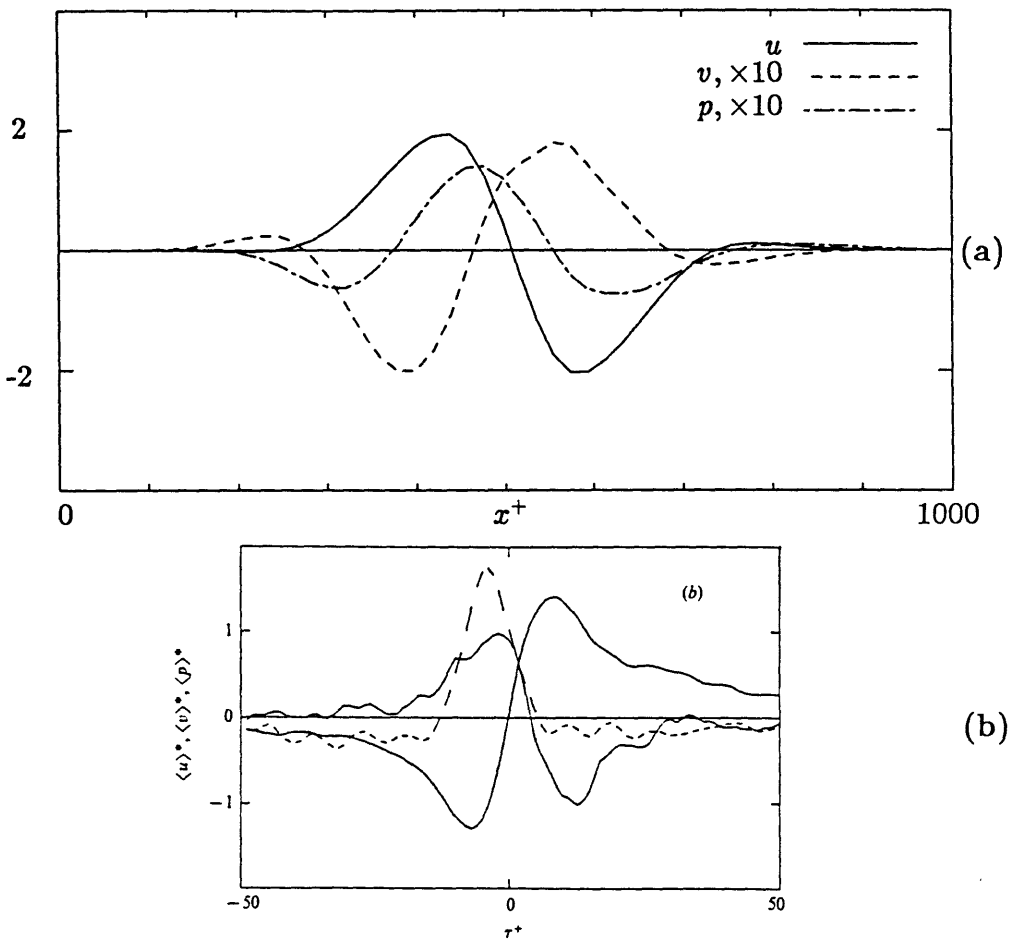

Figure 5.7: Conditionally averaged streamwise and normal velocities at $y^+ = 15$ and wall pressure signal. (a) Data from laminar simulation, plotted in viscous units. (b) Conditionally avereraged data from turbulent boundary layer flow. Reproduced from Johansson, Her and Haritondis (1987). Both plots are normalized by u_τ.

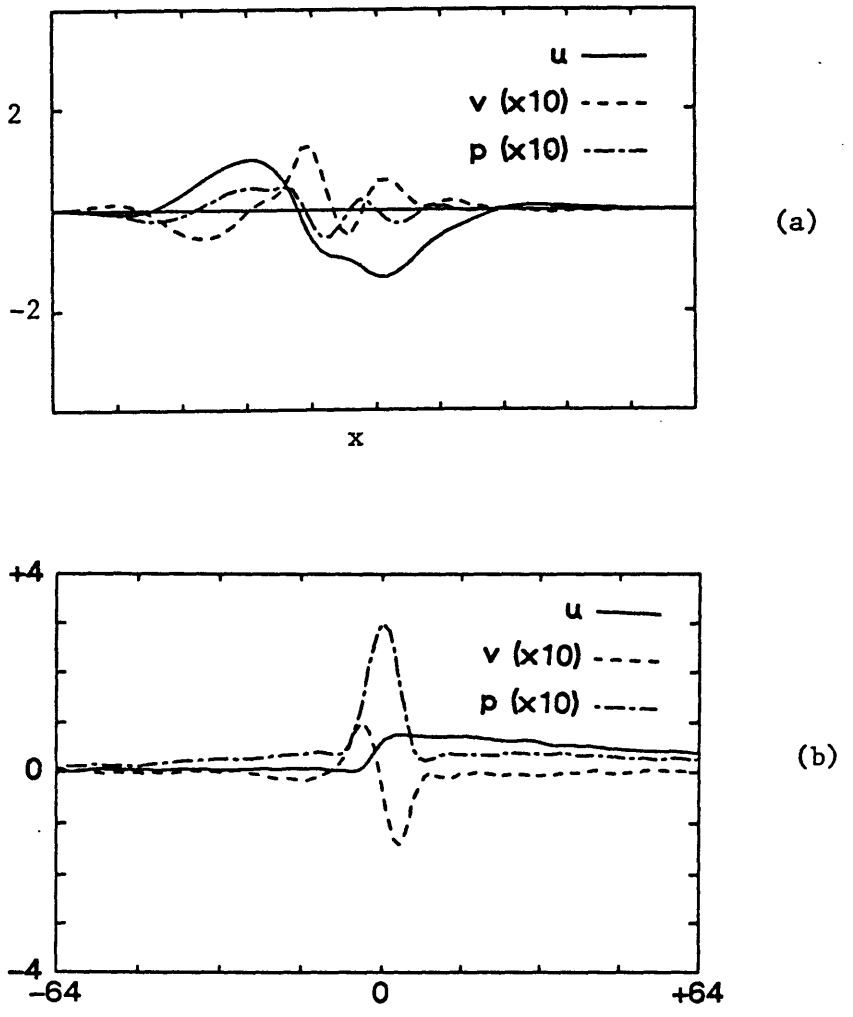

Figure 5.8: Conditionally averaged streamwise and normal velocities at $y^+ = 15$ and wall pressure signal. (a) Data from laminar simulation, plotted in viscous units. (b) Conditionally avereraged data from turbulent boundary layer flow. Reproduced from Haritonidis, Gresko and Breuer (1988). Both plots are normalized by u_τ.

Chapter 6

Concluding Remarks

The evolution of a localized disturbance in a boundary layer has been considered. Several approaches have been used in an attempt to isolate the various aspects of the disturbance which become important in different flow regimes. The disturbance can be conceived of in two parts. The first is the dispersive part which, in the case of a localized disturbance, is a swept back wave packet, similar to the wave packet measured by Gaster and Grant[18,20]. The second part of the disturbance is the transient, or advective part. The transient portion of the disturbance, which is advected at the local mean velocity, is a consequence of the three-dimensional nature of the initial disturbance which, by lifting up fluid elements in the presence of the mean shear, produces large horizontal velocity perturbations. These perturbations quickly dominate the flow field, and remain even after the initial vertical velocities have died away. This was described by Landahl[44] as a "permenant scar" in the horizontal velocities and was also derived by Gustavsson[24] and Henningson[27] for piecewise linear velocity profiles.

In the real (viscous) flow, the transient part created by the lift-up effect does decay and it was found that for low amplitudes, the decay is exponential, leaving behind the growing wave modes of the dispersive portion of the disturbance. The advective part of the disturbance is also subject to an algebraic instability. The three-dimensionality of the disturbance means that even if the streamwise velocity amplitude remains finite,

the disturbance energy will grow because the disturbance elongates as it is stretched by the mean shear. This mechanism was observed in the experimental results, in agreement with Landahl's theory[46] although the presence of viscosity did mean that the disturbance eventually decayed. As the amplitude of the initial disturbance grew, the time for the advective portion to decay became longer, and the stretching effect of the algebraic instability became more noticeable. Even at the low amplitudes, some weak nonlinear effects were observed to affect the evolution of the disturbance. The nonlinearity consisted of the development of two peaks off the centerline of the disturbance and was very similar to the nonlinear effects observed by Gaster and Grant[20] and Cohen[12].

At higher amplitudes, the transient modes were found to be strong enough so that they grew and led directly to transition. This nonlinear bypass of the Tollmien-Schlichting wave-route to transition is in good agreement with the discussion by Morkovin[56] although a more detailed senario is now available from these results. In this case the dispersive modes of the original disturbance became insignificant since the growth and breakdown of the disturbance occurred on a time scale much shorter than the typical time for the growth of Tollmien-Schlichting waves. The growth of the transient was seen to be driven by two phenomena. The first was the nonlinear growth of a marked spanwise structure in which two elongated strips of high-speed fluid develop around the central core of low-speed fluid. This pattern develops regardless of the sign of the initial conditions, and as time progresses, the strips become longer and more intense. In turn they too develop sub-structures, and the power spectra indicate that the nonlinear mechanism is repeated at the higher harmonics. The selection of the spanwise scale in the nonlinear evolution of the disturbance seems to be related to the spanwise scale of the initial disturbance although this must still be investigated. A second numerical

simulation with different initial spanwise scale is planned to resolve this issue.

The second phenomenon contributing to the break down of the transient was a secondary instability growing on the distorted mean profile. The lift-up mechanism creates an inflectional shear layer, and when the initial disturbance has sufficient amplitude, the shear layer is strong enough to support the growth of an instability wave. This wave was seen to start as a two-dimensional wave packet. The amplitude distribution of the wave instability agreed well with the theoretical distribution according to parallel-flow stability theory based on the distorted mean profile. At later times, the instability wave grew and became nonlinear. The threshold level at which the secondary instability must still be determined, and in general it will depend on the strength of the internal shear layer created by the lift-up. Since the lift-up is related to the spanwise scale of the initial disturbance, even a weak disturbance, with strong enough three-dimensionality could create a sufficiently strong shear layer to cause breakdown.

The presence of three-dimensional effects in transition has been reported widely both experimentally and theoretically (for example, Klebanoff, Tidstrom & Sargent[42], Orszag & Patera[60]) and the results of the localized disturbance contains the effects that are found in the secondary instabilities of two-dimensional Tollmien-Schlichting waves. The lift-up effect that creates the shear layers is closely related to the three-dimensional mechanism that creates the lambda vortices and shear layers in the results of Klebanoff et al.[42] and Kovasznay et al[43]. The mechanisms of vortex tilting and stretching described by Orszag & Patera[60] are also present in the localized model. The lift-up of fluid particles lifts up lines of spanwise vorticity (the mean vorticity) which are then tilted and stretched out by the mean shear. The legs of the vortex lines that are lifted, tilted and stretched by the localized disturbance will be turned so that they

form a pair of streamwise vortices. The presence of concentrated streamwise vorticity is, however, only a *consequence* of the lift-up mechanism and the stretching of vorticity by the mean shear. The interaction of the vertical vorticity with the two-dimensional T-S waves that Herbert[29] found is also contained in the mechanism of the localized disturbance since the lift-up effect is precisely the forcing of the vertical vorticity by the vertical velocity.

The association between these shear layer structures in transitional flow and in fully developed turbulent flows stems from the work of Russell and Landahl[63] who first applied the flat-eddy model to a disturbance in a turbulent boundary layer. The similarities between the disturbances seen in the laminar boundary layer and the VISA events in the turbulent flow strongly indicate that the turbulent flow is driven by the initiation, growth and breakdown of such local disturbances which occur randomly in space and time. The main mechanisms in both flows seem to be the same, namely the the three dimensional nature of the disturbance and its interaction with the mean shear, and secondary instabilities leading to breakdown. This view of the structure of turbulent flow is supported by recent experimental and numerical evidence (e.g. Johansson, Alfredsson and Kim[34], Johansson, Alfredsson and Eckelmann[33] and Her[28]). Blackwelder's discussion[9] concerning the presence of streamwise vortices in both transitional and turbulent boundary layers can be expanded upon in the light of the present results. The evolution of localized disturbances will, due to the tilting and stretching of the mean shear, produce elongated structures in the high-shear region such as those seen in the results presented here. Associated with these structures is a strong component of streamwise vorticity which will derive primarily from the strong spanwise shear: $\partial v/\partial z$. This evolution might explain the presence of the streamwise vortices and the low-speed streak that accompanies them in turbulent flows.

Many questions still remain concerning several aspects of the localized disturbance. One intriguing issue is the relationship between the inviscid and the viscous representations of the linear problem. In the inviscid formulation the advective terms are represented by the inviscid continuous spectrum. However, in the viscous problem, Orr-Sommerfeld modes represent the entire flow (at least for a channel flow where the discrete mode form a complete set of normal modes). One interesting problem is to establish how the viscous modes approach the inviscid spectrum as the Reynolds number increases. Another issue to investigate is the nature of the nonlinear interactions that were observed in both the weak disturbances and the strong disturbance. Several approaches to the nonlinear theory for secondary instabilities on T-S waves have reported (cf. Benney & Lin[6], Herbert[29], Craik[14]) but they do not address the issue of the localized disturbance for which the three-dimensionality is inherent in the initial conditions. This problem must still be addressed.

Appendix A

Measurements of Vertical Velocity

This appendix discusses the problems encountered with the measurement of the vertical velocity component and some suggestions as to what caused the problems and what might be tried in order to avoid these problems in future measurements.

A.1 Spurious Results

The measurements of the vertical velocity were made with a standard x-wire probe, illustrated in Figure 2.2. The box size was measured to be 0.4 millimeters on each side and the wire length used was 1.27 microns in diameter. The measurement technique used was identical to that described in Chapter 2 and the operating conditions were also as described in Table 2.1.

Figure A.1 shows the measured vertical velocity at $\Delta x/\delta_* = 37.7$ for a strong disturbance, i.e. a disturbance for which the transient breaks down to a turbulent spot. One should keep in mind Figures 4.19c and 4.20c as references for the streamwise and spanwise velocities at that location. The strong antisymmetric nature of the plot immediately suggests that something is not correct with the measurement. From a theoretical standpoint, one would expect that the vertical velocity must be symmetric about the centerline (if the membrane is symmetric about the centerline). The measured v is

clearly not symmetric about the center line. Close to $z = 0$, the signal is strongly antisymmetric, and further from the centerline, towards the edge of the disturbance, the contours disappear completely on one side of the plot.

This pattern – antisymmetry near the centerline and one-sidedness towards the edge – was found to be repeated at all x-locations, and it was not affected by changes in the amplitude of the disturbance, or by rotating the membrane by 180°. From this it was concluded that the asymmetry in the measurements was not associated with the membrane itself, and therefore had to be either inherent in the flow, or associated with the actual measurement of the vertical velocity. A close examination of the flat plate did not reveal anything that might yield an asymmetry and since the symmetry in both the u and w components of velocity has been observed to be quite good, it was concluded that the problem with the v was based in the measurements themselves.

A.2 Analysis of Experimental Error

The measurements of the streamwise and the spanwise velocities indicate that while the u component is symmetric about the centerline, the w component is antisymmetric. Both signals changes rapidly near the centerline and the spanwise shear in the central core of the disturbance is quite substantial. The stronly antisymmetric measured v suggests that the measurements of the vertical velocity are strongly contaminated, in some manner, by the spanwise velocity which would explain the antisymmetric measurements near the centerline. This theory is supported by the results from the linear initial value problem which indicate that the spanwise velocities are approximately an order of magitude larger than the vertical velocities, and thus may be overwhelming

the hot-wire measurements of v. Additionally, the spanwise shear $\partial u/\partial z$ and $\partial w/\partial z$ is significant, especially near the centerline. This may mean that the two wires of the x-wire actually 'see' two different velocities, which is subsequently interpreted by the calibration table to be a fictitious vertical velocity.

Close to the centerline, where the effect of the spanwise velocity and the spanwise shear is most prominant, the spurious measurements completely dominate the signal and the apparent v takes the structure of the corresponding spanwise velocity. Towards the edge of the disturbance, however, these effects are less strong, and the effect of the w contamination is more subtle. Since the v is symmetric about the centerline while the w is antisymmetric, the effect of the $v - w$ interference is to cancel each other out on the positive side of the disturbance and to reinforce each other on the negative side of the disturbance. This would explain the existance of the wave pattern on one side but not on the other side of the centerline.

A simple test was constructed to test out the possibility that a cross flow might cause an erroneous v measurement. The hot wire was calibrated in the normal fashion and then positioned in a uniform free stream flow. The probe was then rotated through several angles in such a manner that the apparent v to the probe remained zero, but the probe was exposed to a mean spanwise velocity. In an 'ideal' x-wire – one with zero wire separation and no supporting prongs – both wires would be exposed to the same mean spanwise velocity and therefore, the apparent v should remain zero. The wire was rotated through several angles from $-10°$ to $+10°$, and the free stream velocity varied from 1.4 m/s to 6 m/s. The apparent v, as a percentage of the actual cross-stream velocity, w, (calculated from $U \sin\theta$) is tabulated in Table A.1 over the range of angles and velocities. The errors in the measured v are quite substantial at low velocities,

Angle	$U = 1.4$m/s	$U = 2.7$m/s	$U = 6.0$m/s
-10	15.6	11.0	2.7
-5	15.6	11.5	3.6
5	14.8	10.3	4.0
10	13.6	9.0	2.7

Table A.1: Measured vertical velocity (as a percentage of spanwise velocity) caused by cross flow over x-wire probe

and clearly in the boundary layer, where the local velocity is low, a strong cross-stream flow will yield an apparent vertical velocity of as much as 15%. According to the linear calculations of Chapter 3, this spurious v is of the same order as the real v, and clearly the measured results will not reflect the true state of the flow. The actual cause of the erroneous v measurements is unclear, but the blockage of the upstream wire and its supports seems to be the likely explanation. One should note that these errors do not include the possible effects of spanwise shear on the measurement of v, but it seems plausible that in the center of the disturbance, where the spanwise shear is significant, the errors will only be compounded. For a smaller wire separation the effect of spanwise shear will be reduced because of the increase spatial resolution of the probe. One would also expect that the effect of the cross-flow might also be alleviated by reducing the box size of the x-wire and therefore reducing the influence of the wake contamination from the upstream wire.

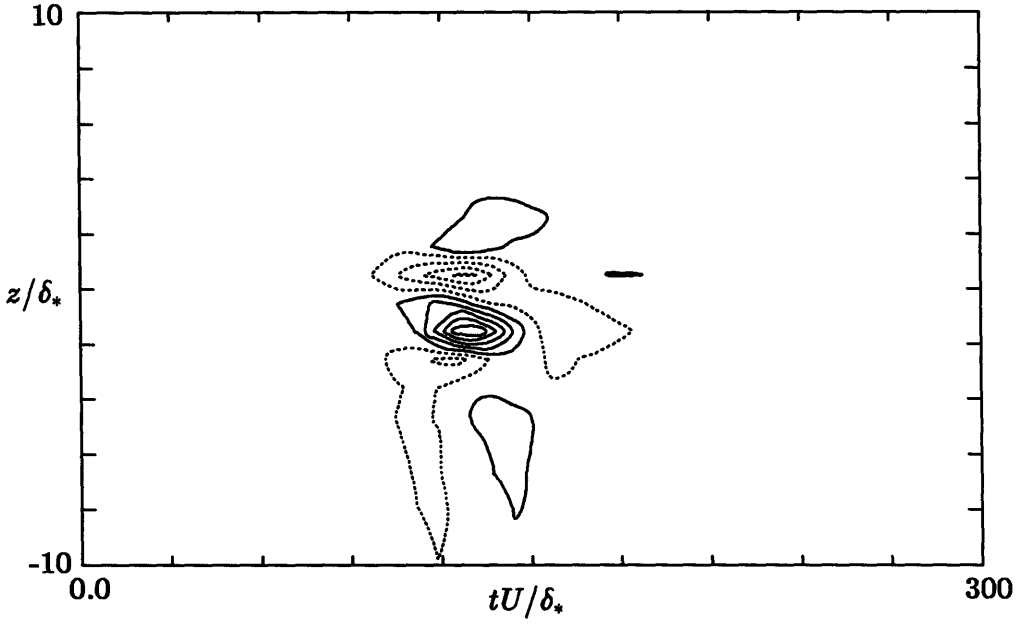

Figure A.1: Experimental Results. Contours of vertical velocity at $\Delta x/\delta_* = 37.7$ illustrating the spurious v measurements. Contour levels: $0.002U_\infty$. Solid lines depict positive contours, dotted lines depict negative contours.

References

[1] ACARLAR, M. S. & SMITH, C. R. 1987. A study of hairpin vortices in a laminar boundary layer. Part 1. Hairpin vorticies generated by a hemispherical protuberance. *J. Fluid Mech.* **175**, 1–42.

[2] ACARLAR, M. S. & SMITH, C. R. 1987. A study of hairpin vortices in a laminar boundary layer. Part 2. Hairpin vorticies generated by fluid injection. *J. Fluid Mech.* **175**, 43–48.

[3] AMINI, J. 1978. ***Transition contrôlée en couche limite: Etude expériementale du développement d'une pertubation tridimensionnelle instantanée.*** PhD thesis. L'institute national polytechnique de Grenoble.

[4] AMINI, J. & LESPINARD, G. 1982. Experimental study of an "incipient spot" in a transitional boundary layer. *Phys. Fluids* **25**,(10) 1743–1750.

[5] BENNEY, D. J. & GUSTAVSSON, L. H. 1981. A new mechanism for linear and nonlinear hydrodynamic instability. *SIAM J. Appl. Math.* **64**, 185–209.

[6] BENNEY, D. J. & LIN, C. C. 1960. On the secondary motion induced by oscillations in a shear flow. *Phys. Fluids* **3**, 656–657.

[7] BETCHOV, R. & CRIMINALE, W. O. 1967. ***Stability of parallel flows.*** Academic Press.

[8] BLACKWELDER, R. F. & KAPLAN, R. E. 1976. On the wall structure of the turbulent boundary layer. *J. Fluid Mech.* **76**, 89–112.

[9] BLACKWELDER, R. F. 1983. Analogies between transitional and turbulent boundary layers. *Phys. Fluids* **26**,(10) 2807–2815.

[10] CASE, K. M. 1960. Stability of invisicid plane Couette flow. *Phys. Fluids* **3**,(2) 143 – 148.

[11] COHEN, J. & WYGNANSKI, I. 1987. The evolution of instabilities in the axisymmetric jet. part 2. the flow resulting from the interaction between two waves. *J. Fluid Mech.* **176**, 221–235.

[12] COHEN, J. 1988. Private communication.

[13] CONTE, S. D. 1966. The numerical solution of linear boundary value problems. *SIAM J. Appl. Math.* **8**,(3) 309 – 321.

[14] CRAIK, A. D. D. 1971. Nonlinear resonant instability in boundary layers. *J. Fluid Mech.* **50**, 393–413.

[15] CRAIK, A. D. D. 1980. Nonlinear evolution and breakdown in unstable boundary layers. *J. Fluid Mech.* **99**, 247–265.

[16] DRAZIN, P. G. & HOWARD, L. N. 1966. Hydrodynamic stability of parallel flows of inviscid fluid. *Adv. Appl. Math.* **9**, 1–89.

[17] DRAZIN, P. G. & REID, W. H. 1981. *Hydrodynamic Stability.* Cambridge University Press.

[18] GASTER, M. 1975. A theoretical model for the development of a wave packet in a laminar boundary layer. *Proc. R. Soc. of Lond. A.* **347**, 271–289.

[19] GASTER, M. 1980. Estimates of the errors incurred in various asymptoptic representations of wave packets. In EPPLER & FASEL, editors, *Laminar-Turbulent transition.* pp 14 – 16 Springer.

[20] GASTER, M. & GRANT, I. 1975. An experimental investigation of the formation and development of a wave packet in a laminar boundary layer. *Proc. R. Soc. of Lond. A.* **347**, 253–269.

[21] GILBERT, N. & KLEISER, L. 1986. Subcritical transition to turbulence in channel flow. In SCHUMANN, & FRIEDRICH, , editors, *Direct and large eddy simulations of turbulent flows.* Vieweg-Verlag. Notes on numerical fluid mechanics. Vol 15.

[22] GRESKO, L. 1988. Private communication.

[23] GUSTAVSSON, L. H. & HULTGREN, L. S. 1980. A resonance mechanism in plane Couette flow. *J. Fluid Mech.* **98**, 149–159.

[24] GUSTAVSSON, L. H. 1978. *On the evolution of disturbances in boundary layer flows.* PhD thesis. Royal Institute of Technology, Department of Mechanics Stockhom, Sweden.

[25] HARITONIDIS, J. H., GRESKO, L. S. & BREUER, K. S. 1988. Wall pressure peaks and waves. In *Proceedings of the Zoran Zaric Memorial International Seminar on Near-Wall Turbulence* Dubrovnic.

[26] HEISENBERG, W. 1924. Uber stabilitat und turbulenz von flussigkeitsstromen. *Ann. d. Phys.* **74**, 577 – 627. [English translation: NACA TM 1291. (1951)].

[27] HENNINGSON, D. S. 1987. The inviscid initial value problem for a piecewise linear mean flow. *SIAM J. Appl. Math.* , 1 – 26.

[28] HER, J. 1987. *The relation between wall pressure and the flow field in the wall region of a turbulent boundary layer.* PhD thesis. Massachusetts Institute of Technology, Department of Aeronautics and Astronautics.

[29] HERBERT, T. 1984. Analysis of the subharmonic route to transition in boundary layers. AIAA Paper 84-0009.

[30] HERBERT, T. 1985. Three dimesional phenomena in the transitional flat plate boundary layer. AIAA Paper 85-0489.

[31] JOHANSSON, A. V. 1987. Private communication.

[32] JOHANSSON, A. V. & ALFREDSSON, P. H. 1982. On the structure of turbulent channel flow. *J. Fluid Mech.* **122**, 295–314.

[33] JOHANSSON, A. V., ALFREDSSON, P. H. & ECKELMANN, H. 1987. On the evolution of shear layer structures in near wall turbulence. In COMPTE-BELLOT, G. & MATHIEU, J., editors, *Advances in Turbulence*. pp 383–390 Springer-Verlag.

[34] JOHANSSON, A. V., ALFREDSSON, P. H. & KIM, J. 1987. Shear layer structure in near wall turbulence. In *Proceedings of the 1987 summer program*. pp 237–251 NASA / Stanford Center for turbulence research.

[35] JOHANSSON, A. V., HER, J. & HARITONIDIS, J. H. 1987. On the generation of high amplitude wall-pressure peaks in turbulent boundary layers and spots. *J. Fluid Mech.* **175**, 119–142.

[36] JORDINSON, R. 1970. The flat plate boundary layer. part 1. numerical integration of the orr-sommerfeld equation. *J. Fluid Mech.* **43**, 801–811.

[37] KACHANOV, YU. S. & LEVCHENKO, V. YA. 1984. The resonant interaction of disturbances at laminar turbulent transition in a boundary layer. *J. Fluid Mech.* **138**, 209–247.

[38] KIM, J. 1985. Turbulent structures associated with the bursting event. *Phys. Fluids* **28**,(1) 52–58.

[39] KIM, J. & MOIN, P. 1985. The structure of the vorticity field in turbulent channel flow. part 1. study of ensemble averaged fields. *J. Fluid Mech.* **162**, 339.

[40] KIM, J., MOIN, P. & MOSER, R. 1987. Turbulence statistics in fully developed channel flow. *J. Fluid Mech.* **177**, 133 – 166.

[41] KLEBANOFF, P. S. & TIDSTROM, K. D. 1959. Evolution of amplified waves leading to transition in a boundary layer with zero pressure. *NASA Tech. Rep.* No. TN D-195.

[42] KLEBANOFF, P. S., TIDSTROM, K. D. & SARGENT, L. M. 1961. Transition in a boundary layer. *J. Fluid Mech.* **12**, 1–34.

[43] KOVASZNAY, L. S. G., KOMODA, H. & VASUDEVA, B. R. 1985. Detailed flow field in transition. In *Proceedings of the 1962 heat transfer and fluid mechanics inisitute, University of Washington*. pp 1 – 26.

[44] LANDAHL, M. T. 1975. Wave breakdown and turbulence. *SIAM J. Appl. Math.* **28**, 735 – 756.

[45] LANDAHL, M. T. 1977. Dynamics of boundary layer transition and the mechanism of drag reduction. *Phys. Fluids* **20**,(10, Part II) S55 – S63.

[46] LANDAHL, M. T. 1980. A note on an algebraic instablitiy of inviscid paraller shear flows. *J. Fluid Mech.* **98**, 243–251.

[47] LANDAHL, M. T. 1984. Coherent structures in turbulence and Prandtl's mixing length theory. *Z. Flugwiss. Weltraumforsch* **8**, 233–242. Heft 4.

[48] LANDAHL, M. T. & MOLLO-CHRISTENSEN, E. 1987. *Turbulence and Random Processes in Fluid Mechanics*. Cambridge University Press.

[49] LEUPTOW, R., BREUER, K. S. & HARITONIDIS, J. H. 1988. Computer-aided x-wire calibration using a look-up table. *Experiments in Fluids* **6**, 115 – 118.

[50] LIN, C. C. 1955. *Theory of hydrodynamic stability.* Cambridge University Press.

[51] MACK, L. M. 1976. A numerical study of the temporal eigenvalue spectrum of the Blasius boundary layer. *J. Fluid Mech.* **73**, 497 – 520.

[52] MANGUS, J. F. 1984. *Preliminary measurements of drag and bursting frequency in a manipulated turbulent boundary layer* Master's thesis. Department of Aeronautics and Astronautics, Massachusetts Institute of Technology.

[53] MASLOWE, S. A. 1981. Shear flow instability and transition. In SWINNEY, H. L. & GOLLUB, J. P., editors, *Hydrodynamic instabilities and the transition to turbulence.* pp 181 – 228 Springer-Verlag.

[54] MOIN, P. & KIM, J. 1982. Numerical investigation of turbulent channel flow. *J. Fluid Mech.* **118**, 341.

[55] MOIN, P. & KIM, J. 1985. The structure of the vorticity field in turbulent channel flow. part 1. analysis of instantaneous fields and statistical correlations. *J. Fluid Mech.* **155**, 441.

[56] MORKOVIN, M. V. 1969. On the many faces of transition. In WELLS, C., editor, *Viscous Drag Reduction.* Plenum Press.

[57] OBREMSKI, H. J., MORKOVIN, M. & LANDAHL, M. T. A portfolio of stability characteristics of incompressible boundary layers. 1969. AGARDOgraph 134, NATO, Paris.

[58] ORR, W. M. F. 1881. The stability of the steady motions of a perfect liquid and of a viscous liquid. Part I: A perfect liquid. Part II: A viscous liquid. *Proc. R. Irish Acad. A* **27**, 9 – 138.

[59] ORSZAG, S. O. & KELLS, L. C. 1980. Transition to turbulence in plane Poiseuille and plane Couette flow. *J. Fluid Mech.* **96**, 159–205.

[60] ORSZAG, S. O. & PATERA, A. T. 1983. Secondary instability of wall-bounded shear flows. *J. Fluid Mech.* **128**, 347 – 385.

[61] RAYLEIGH, L. 1887. On the stability of certain fluid motions. *Proc. Math. Soc. Lond.* **11**, 57 – 70.

[62] REYNOLDS, O. 1883. On the experimental investigation of the circumstances which determine whether the motion of water shall be direct or sinuous, and the law or resistance in parallel channels. *Phil. Trans. Roy. Soc. Lond.* **174**, 935 – 982.

[63] RUSSELL, J. M. & LANDAHL, M. T. 1984. The evolution of a flat eddy near a wall in an inviscid shear flow. *Phys. Fluids* **27**,(3) 557–570.

[64] SCHEWE, G. 1983. On the structure and resolution of wall-pressure fluctuations associated with turbulent boundary layer flow. *J. Fluid Mech.* **134**, 311 – 328.

[65] SCHLICHTING, H. 1933. Berechning def anfachung kleiner storungen bei der plattenstromung. *ZAMM* **13**, 171 –174.

[66] SCHUBAUER, G. B. & SKRAMSTAD, H. F. 1947. Laminar boundary layer oscillations and the stability of laminar flow. *J. Aero. Sci.* **14**, 69–78.

[67] SOMMERFELD, A. 1908. Ein bietrag zur hydrodynamischen erklarung der turbulenten flussigkeitbewegungen. In *Atti. del 4. Congr. Internat. dei Mat. III.* pp 116–124 Roma.

[68] SPALART, P. R. 1986. Numerical simulation of boundary layers: Part 1. Weak formulation and numerical method. *NASA Technical Memorandum* No. 88222.

[69] SPALART, P. R. 1986. Direct simulation of a turbulent boundary layer up to $Re_\theta = 1410$. *NASA Technical Memorandum* No. 89407.

[70] SPALART, P. R. & YANG, K. 1987. Numerical study of ribbon induced transition in blasius flow. *J. Fluid Mech.* **178**, 345–365.

[71] SWEARINGEN, J. D. & BLACKWELDER, R. F. 1987. The growth and breakdown of streamwise vortices in the presence of a wall. *J. Fluid Mech.* **182**, 255–290.

[72] TANI, I. 1969. Boundary layer transition. *Ann. Rev. Fluid Mech.* **1**, 169–196.

[73] TOLLMIEN, W. 1929. Über die entstehung der turbulenz. 1. Mitt. Nachr. Ges. Wiss. Göttingen, Math. Phys. Klasse 21–44 [English translation NACA TM 609 (1931)].

[74] WRAY, A. & HUSSAINI, M. Y. 1980. Numerical experiments in boundary layer stability. *Proc. R. Soc. of Lond. A.* **392**, 373–389.